

ABSTRACT

Title of Thesis: THE EFFECT OF ARCHITECTURE AND SHEAR STRESS ON ENDOTHELIALIZATION OF 3D PRINTED VASCULAR NETWORKS

Tara Talaie, Master of Science, 2016

Thesis Directed By: Chair, Dr. John P. Fisher, Fischell Department of Bioengineering

Despite significant progress in the field of tissue engineering within the last decade, a number of unsolved problems still remain. One of the most relevant issues is the lack of proper vascularization that limits the size of engineered tissues to smaller than clinically relevant dimensions. In particular, the growth of engineered tissue *in vitro* within bioreactors is plagued with this challenge. Specifically, the tubular perfusion system bioreactor has been used for large scale bone constructs; however these engineered constructs lack inherent vasculature and quickly develop a hypoxic core, where no nutrient exchange can occur, thus leading to cell death. Through the use of 3D printed vascular templates in conjunction with a tubular perfusion system bioreactor, we attempt to create an endothelial cell monolayer on 3D scaffolds that could potentially serve as the foundation of inherent vasculature within these engineered bone grafts.

THE EFFECT OF ARCHITECTURE AND SHEAR STRESS ON
ENDOTHELIALIZATION OF 3D PRINTED VASCULAR NETWORKS

by

Tara Talaie

Thesis submitted to the Faculty of the Graduate School of the
University of Maryland, College Park, in partial fulfillment
of the requirements for the degree of
Master of Science
2016

Advisory Committee:

Dr. John P. Fisher, Chair

Dr. Kimberly Stroka

Dr. Ian White

© Copyright by

Tara Talaie

2016

Acknowledgements

I would like to thank my advisor, Dr. John P. Fisher, for allowing me to join the Tissue Engineering and Biomaterials Laboratory (TEBL). Having no engineering background, he always made sure that I had all the resources I needed to succeed and provided positive support to keep me on track.

Additionally, I would like to thank Dr. Jesse Placone, Max Lerman, and Bao Nguyen, who willingly spent many hours teaching me various laboratory skills and techniques, and took time from their busy schedules to help me and answer my questions.

I would also like to thank Dr. Stroka and Dr. White who graciously agreed to serve as committee members for my defense on relatively short notice.

Finally, I would like to thank the rest of the TEBL members: Laurie Bracaglia, Charlotte Piard, Javier Rueda, Ting Guo, Vincent Kuo, Navein Arumugasaamy, Maddelyn Golding, and Dr. Hannah Baker for all their help and support along the way.

Table of Contents

Acknowledgements	ii
List of Tables	vi
List of Figures.....	viii
List of Abbreviations	xv
Chapter 1: Introduction.....	1
Chapter 2: Related Literature	6
<i>Introduction</i>	6
<i>TPS Bioreactors</i>	8
Bioreactor Design	8
Advantages of a TPS Bioreactor	10
<i>Tissue Engineering Strategies for Vascularized Constructs</i>	11
3D Printing of Bone and Vascular Tissue Constructs	13
<i>Oxygen in the HUVEC Niche</i>	17
<i>Effect of Architecture and Topographic Patterns on Endothelial Cell Behavior</i>	17
<i>Effects of Shear Stress on Endothelial Cell Behavior</i>	21
Chapter 3: The Effect of Architecture and Shear Stress on Endothelialization of 3D Printed Vascular Networks.....	22
<i>Introduction</i>	22
<i>Materials and Methods</i>	24
SolidWorks Geometry Generation	24
SolidWorks Flow Simulations.....	24
Experimental Group Determination	26

3D Printing	28
EShell Sterilization	31
Cell Culture.....	31
Fibronectin Coating and Cell Seeding.....	32
Static 2D Setup	32
Dynamic Growth Chamber Setup.....	32
Bioreactor Setup	34
Viability, Morphology & Proliferation Analysis.....	37
DNA Analysis.....	39
Statistical Analysis	39
<i>Results</i>	40
SolidWorks CFD Analysis	40
Static Conditions Endothelial Cell Analysis	48
Dynamic Growth Chamber Endothelial Cell Analysis.....	50
<i>In Vitro</i> Bioreactor Endothelial Cell Analysis.....	53
<i>Discussion</i>	60
SolidWorks CFD Analysis	60
Static Conditions Endothelial Cell Analysis	61
Dynamic Growth Chamber Analysis.....	61
TPS Bioreactor Analysis	62
<i>Conclusion</i>	64
Chapter 4: Appendix A: Raw Data & Calculations.....	68

<i>Static Condition Studies</i>	68
Day 1 (24h).....	68
Day 3: Morphology and Proliferation	70
Day 7: Proliferation	71
<i>Dynamic Growth Chamber Studies</i>	72
<i>Bioreactor Study</i>	73
Pre-TPS bioreactor study setup calculations	73
DNA Analysis: Data and Calculations	75
Chapter 5: Appendix B: SolidWorks CFD Results	79
<i>Shear Stress Surface Plot Contours</i>	79
<i>Flow Trajectories</i>	97
Bibliography	118

List of Tables

Table 1: Surface shear stress results for group 1 diameter experimental groups in bioreactor study.	43
Table 2: Surface shear stress results from group 2 diameter experimental groups in bioreactor study.	44
Table 3: Surface shear stress results from group 3 diameter experimental groups in bioreactor study.	45
Table 4: No pattern/flat surface cell counts and calculations at day 1 time point.	71
Table 5: No pattern/flat surface attachment efficiency data at Day 1 time point.	71
Table 6: Aspect ratio data and calculations at day 1 time point.	72
Table 7: No pattern flat surface cell count data at day 3 time point.	72
Table 8: Aspect ratio data at day 3 time point.	73
Table 9: No pattern/flat surface cell counts and calculations at day 7 time point.	73
Table 10: No pattern/flat surface total cells on 2D prints at day 1 time point.	74
Table 11: No pattern flat surface, attachment efficiency at day 1 time point.	74
Table 12: No pattern/flat surface, aspect ratio at day 1 time point.	74
Table 13: Tubing sizes available for TPS bioreactor study.	75
Table 14: Diameters of 3D scaffolds based on tubing sizes.	75
Table 15: Tubing length quantities needed for setup of TPS bioreactor.	75
Table 16: Total inner surface area of scaffolds in bioreactor setup.	76
Table 17: Total volume of tubing in TPS bioreactor.	76
Table 18: Total HUVEC requirement needed based on total inner surface area of	

scaffolds in bioreactor setup.	76
Table 19: PICO green assay standard curves.	77
Table 20: PICO green plate setup. H= high standard curve, L = low standard curve. D = dynamic conditions sample (TPS bioreactor). S = static conditions sample. Sample 1 = group 1, no pattern. Sample 2 = group 1, channels. Sample 3 = group 1, channels and pits. Sample 4 = group 2, no pattern. Sample 5 = group 2, channels. Sample 6 = group 2, channels and pits. Sample 7 = group 3, no pattern. Sample 8 = group 3, channels. Sample 9 = group 3, channels and pits.	77
Table 21: PICO green plate results raw data corresponding to plate setup above.	78
Table 22: PICO green plate results in micrograms/mL and corresponding to plate setup above.....	78
Table 23: PICO green results. Significant differences between samples.	80

List of Figures

Figure 1. Nonunion versus malunion fracture	1
Figure 2: Group 1 diameter dimensions. a. Inner and outer diameters (mm). b. Length of cylinder (mm).	27
Figure 3: Group 2 diameter dimensions. a. Inner and outer diameters (mm). b. Length of cylinder (mm).	27
Figure 4: Group 3 diameter dimensions. a. Inner and outer diameters (mm). b. Length of cylinder (mm).	28
Figure 5: a. Channel surface topography. b. Channel and pits combination surface topography.	28
Figure 6: Example of EShell 300 Clear Print a. Side view with supports. b. Top view with supports.	31
Figure 7: Growth Chamber Setup	35
Figure 8: Model of bioreactor setup showing one complete tubing line circuit. Green represents tubing containing scaffolds. Pink represents connectors between tubing segments. Blue cylinder on the right represents media reservoir.	36
Figure 9: Bioreactor setup with lines in parallel	37
Figure 10: Aspect ratio calculated by dividing width by height.	39
Figure 11: Aspect ratio calculated by dividing longest side by shorter side, as done in this study.	39
Figure 12: Surface plot contour of shear stress, group 2 diameter with channels and pits, flow rate of 10 mL/minute.	42

Figure 13: Flow trajectory of group 2 diameter with channels and pits, flow rate of 10 mL/minute.	42
Figure 14: Selected images of HUVEC on day 1 at 20x.	49
Figure 15: Selected images of HUVEC on day 3 at 20x.	49
Figure 16: Aspect ratio of HUVEC on day 1 versus day 3.	50
Figure 17: Proliferation of HUVECs from day 1 to day 3.	51
Figure 18: Static versus dynamic, no pattern group HUVEC cell density on day 1. ...	52
Figure 19: Random orientation under flow, no pattern flat surface group. 10x.	53
Figure 20: Group 1 diameter, channels pattern at day 7 time point. 2.5x	55
Figure 21: Group 1 diameter, channels and pits pattern at day 7 time point. 2.5x.	56
Figure 22: DNA PICO green assay results.	57
Figure 23: Group 1 no pattern at 0.5 mL/minute flow rate.	81
Figure 24: Group 1 no pattern at 1 mL/minute flow rate.	81
Figure 25: Group 1 no pattern at 2 mL/minute flow rate.	81
Figure 26: Group 1 no pattern at 5 mL/minute flow rate.	82
Figure 27: Group 1 no pattern at 10 mL/minute flow rate.	82
Figure 28: Group 1 no pattern at 20 mL/minute flow rate.	82
Figure 29: Group 1 with channels at 0.5 mL/minute flow rate.	83
Figure 30: Group 1 with channels at 1 mL/minute flow rate.	83
Figure 31: Group 1 with channels at 2 mL/minute flow rate.	83
Figure 32: Group 1 with channels at 5 mL/minute flow rate.	84
Figure 33: Group 1 with channels at 10 mL/minute flow rate.	84

Figure 34: Group 1 with channels at 20 mL/minute flow rate.	84
Figure 35: Group 1 with channels and pits at 0.5 mL/minute flow rate.	85
Figure 36: Group 1 with channels and pits at 1 mL/minute flow rate.	85
Figure 37: Group 1 with channels and pits at 2 mL/minute flow rate.	85
Figure 38: Group 1 with channels and pits at 5 mL/minute flow rate.	86
Figure 39: Group 1 with channels and pits at 10 mL/minute flow rate.	86
Figure 40: Group 1 with channels and pits at 20 mL/minute flow rate.	86
Figure 41: Group 2 no pattern at 0.5 mL/minute flow rate.	87
Figure 42: Group 2 no pattern at 1 mL/minute flow rate.	87
Figure 43: Group 2 no pattern at 2 mL/minute flow rate.	87
Figure 44: Group 2 no pattern at 5 mL/minute flow rate.	88
Figure 45: Group 2 no pattern at 10 mL/minute flow rate.	88
Figure 46: Group 2 no pattern at 20 mL/minute flow rate.	88
Figure 47: Group 2 with channels at 0.5 mL/minute flow rate.	88
Figure 48: Group 2 with channels at 1 mL/minute flow rate.	89
Figure 49: Group 2 with channels at 2 mL/minute flow rate.	89
Figure 50: Group 2 with channels at 5 mL/minute flow rate.	89
Figure 51: Group 2 with channels at 10 mL/minute flow rate.	90
Figure 52: Group 2 with channels at 20 mL/minute flow rate.	90
Figure 53: Group 2 with channels and pits at 0.5 mL/minute flow rate.	90
Figure 54: Group 2 with channels and pits at 1 mL/minute flow rate.	91
Figure 55: Group 2 with channels and pits at 2 mL/minute flow rate.	91

Figure 56: Group 2 with channels and pits at 5 mL/minute flow rate.	91
Figure 57: Group 2 with channels and pits at 10 mL/minute flow rate.	92
Figure 58: Group 2 with channels and pits at 20 mL/minute flow rate.	92
Figure 59: Group 3 no pattern at 0.5 mL/minute flow rate.	92
Figure 60: Group 3 no pattern at 1 mL/minute flow rate.	93
Figure 61: Group 3 no pattern at 2 mL/minute flow rate.	93
Figure 62: Group 3 no pattern at 5 mL/minute flow rate.	94
Figure 63: Group 3 no pattern at 10 mL/minute flow rate.	94
Figure 64: Group 3 no pattern at 20 mL/minute flow rate.	94
Figure 65: Group 3 with channels at 0.5 mL/minute flow rate.	95
Figure 66: Group 3 with channels at 1 mL/minute flow rate.	95
Figure 67: Group 3 with channels at 2 mL/minute flow rate.	96
Figure 68: Group 3 with channels at 5 mL/minute flow rate.	96
Figure 69: Group 3 with channels at 10 mL/minute flow rate.	96
Figure 70: Group 3 with channels at 20 mL/minute flow rate.	97
Figure 71: Group 3 with channels and pits at 0.5 mL/minute flow rate.	97
Figure 72: Group 3 with channels and pits at 1 mL/minute flow rate.	97
Figure 73: Group 3 with channels and pits at 2 mL/minute flow rate.	98
Figure 74: Group 3 with channels and pits at 5 mL/minute flow rate.	98
Figure 75: Group 3 with channels and pits at 10 mL/minute flow rate.	98
Figure 76: Group 3 with channels and pits at 20 mL/minute flow rate.	99
Figure 77: Group 1 no pattern at 0.5 mL/minute flow rate.	99

Figure 78: Group 1 no pattern at 1 mL/minute flow rate.	100
Figure 79: Group 1 no pattern at 2 mL/minute flow rate.	100
Figure 80: Group 1 no pattern at 5 mL/minute flow rate.	100
Figure 81: Group 1 no pattern at 10 mL/minute flow rate.	101
Figure 82: Group 1 no pattern at 20 mL/minute flow rate.	101
Figure 83: Group 1 with channels at 0.5 mL/minute flow rate.	101
Figure 84: Group 1 with channels at 1 mL/minute flow rate.	102
Figure 85: Group 1 with channels at 2 mL/minute flow rate.	102
Figure 86: Group 1 with channels at 5 mL/minute flow rate.	103
Figure 87: Group 1 with channels at 10 mL/minute flow rate.	103
Figure 88: Group 1 with channels at 20 mL/minute flow rate.	103
Figure 89: Group 1 with channels and pits at 0.5 mL/minute flow rate.	103
Figure 90: Group 1 with channels and pits at 1 mL/minute flow rate.	104
Figure 91: Group 1 with channels and pits at 2 mL/minute flow rate.	104
Figure 92: Group 1 with channels and pits at 5 mL/minute flow rate.	104
Figure 93: Group 1 with channels and pits at 10 mL/minute flow rate.	105
Figure 94: Group 1 with channels and pits at 20 mL/minute flow rate.	105
Figure 95: Group 2 no pattern at 0.5 mL/minute flow rate.	105
Figure 96: Group 2 no pattern at 1 mL/minute flow rate.	106
Figure 97: Group 2 no pattern at 2 mL/minute flow rate.	106
Figure 98: Group 2 no pattern at 5 mL/minute flow rate.	106
Figure 99: Group 2 no pattern at 10 mL/minute flow rate.	107

Figure 100: Group 2 no pattern at 20 mL/minute flow rate.	107
Figure 101: Group 2 with channels at 0.5 mL/minute flow rate.	107
Figure 102: Group 2 with channels at 1 mL/minute flow rate.	108
Figure 103: Group 2 with channels at 2 mL/minute flow rate.	108
Figure 104: Group 2 with channels at 5 mL/minute flow rate.	109
Figure 105: Group 2 with channels at 10 mL/minute flow rate.	109
Figure 106: Group 2 with channels at 20 mL/minute flow rate.	110
Figure 107: Group 2 with channels and pits at 0.5 mL/minute flow rate.	110
Figure 108: Group 2 with channels and pits at 1 mL/minute flow rate.	111
Figure 109: Group 2 with channels and pits at 2 mL/minute flow rate.	111
Figure 110: Group 2 with channels and pits at 5 mL/minute flow rate.	112
Figure 111: Group 2 with channels and pits at 10 mL/minute flow rate.	112
Figure 112: Group 2 with channels and pits at 20 mL/minute flow rate.	113
Figure 113: Group 3 no pattern at 0.5 mL/minute flow rate.	113
Figure 114: Group 3 no pattern at 1 mL/minute flow rate.	114
Figure 115: Group 3 no pattern at 2 mL/minute flow rate.	114
Figure 116: Group 3 no pattern at 5 mL/minute flow rate.	115
Figure 117: Group 3 no pattern at 10 mL/minute flow rate.	115
Figure 118: Group 3 no pattern at 20 mL/minute flow rate.	116
Figure 119: Group 3 with channels at 0.5 mL/minute flow rate.	116
Figure 120: Group 3 with channels at 1 mL/minute flow rate.	117
Figure 121: Group 3 with channels at 2 mL/minute flow rate.	117

Figure 122: Group 3 with channels at 5 mL/minute flow rate.	118
Figure 123: Group 3 with channels at 10 mL/minute flow rate.	118
Figure 124: Group 3 with channels at 20 mL/minute flow rate.	119
Figure 125: Group 3 with channels and pits at 0.5 mL/minute flow rate.	119
Figure 126: Group 3 with channels and pits at 1 mL/minute flow rate.	120
Figure 127: Group 3 with channels and pits at 2 mL/minute flow rate.	120
Figure 128: Group 3 with channels and pits at 5 mL/minute flow rate.	121
Figure 129: Group 3 with channels and pits at 10 mL/minute flow rate.	121
Figure 130: Group 3 with channels and pits at 20 mL/minute flow rate.	122

List of Abbreviations

TPS: Tubular Perfusion System

CAD: Computer Aided Design

BTE: Bone Tissue Engineering

EPC: Endothelial Progenitor Cell

MMP: Matrix Metalloproteinase

ECM: Extracellular Matrix

VEGF: Vascular Endothelial Growth Factor bFGF: basic
Fibroblast Growth Factor

PDGF: Platelet Derived Growth Factor

TGF- β : Transforming Growth Factor –Beta

UV: Ultra Violet

FD: Fused Deposition Modeling

FFF: Fused Filament Fabrication

PVA: Poly(Vinyl Alcohol)

PDMS: Polydimethylsiloxane

HUVEC: Human Umbilical Vein Endothelial Cell hMSC: Human
Mesenchymal Stem Cell

PECAM-1: Platelet Endothelial Cell Adhesion Molecule -1

VCAM-1: Vascular Cell Adhesion Protein -1

ICAM-1: Intercellular Cell Adhesion Molecule -1 eNOS:
endothelial Nitric Oxide Synthetase NO: Nitric Oxide

DLP: Digital Light Processing

PBS: Phosphate Buffered Saline

EBM-2: Endothelial Basal Media

Chapter 1: Introduction

Clinicians and researchers are investigating novel methods for repairing critically sized bone defects to meet the large demand for bone repair in the clinic. Currently, bone is second only to blood as the most transplanted tissue.¹ Bone tissue defects can be due to elevated levels of stress associated with physical activity, obesity, and aging. Approximately 15 million bone fractures occurred worldwide in 2011, with nearly 10% resulting in nonunions.¹ A nonunion fracture is classified as a fracture which fails to heal after nine months without intervention (Figure 1).²

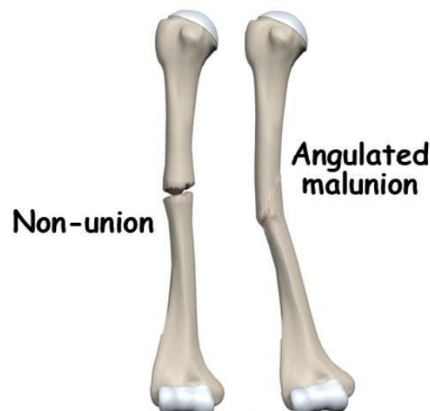


Figure 1. Nonunion versus malunion fracture.

Nonunion fractures take an extended or indefinite time to heal, while typical fractures heal within a few weeks.³ Commonly, these nonunions result in a significant displacement between the two fractured ends; if this displacement is large enough as to not allow for natural healing, the gap is then classified as being above the critical defect size. Normally, bone fractures with gaps below the critical defect size will fill the void via natural healing and proper non-surgical fixation (hard cast, splint, sling,

etc) of the fracture. These critically sized defects require larger scale bone grafts and thus there is a large clinical need to develop one grafts on this larger scale.

In 2010, the CDC reported 342,030 hospitalizations in the United States for extremity fractures with an average treatment cost of about \$34,016.⁴ Conservatively, about 10% of traumatic fractures result in a nonunion.⁵ In these cases, surgical intervention is commonly needed to fully heal the wound through the use of artificial supports and bone grafts. The goal of bone grafts and bone tissue engineering strategies is to create a living tissue that can self-maintain and grow within a patient. Nonunions that require surgery to aid the closure of the critically sized gap can be complicated by infection and rejection of the implant, thus potentially leading to multiple revision surgeries and further complications.³ Therefore, it is critical to optimize these surgical treatment strategies in order to reduce the potential physical and economic effects of complications.

Approximately 1 million grafting procedures are performed each year.⁶ Transplanted human tissue used for bone regeneration is derived from either autologous sources (elsewhere in the patient's body) or from donated allogeneic tissue (e.g. cadaveric tissue, living donors). Currently, the gold standard for harvesting bone tissue for implantation are autografts because autologous tissues have immune reaction side effects and complications.^{2,7} Unfortunately however, both options have significant disadvantages and the rate of complications arising from an allograft is nearly 30%.⁸ Furthermore, the introduction of a secondary defect site increases the risk for complications such as post-surgical pain, infection, and scarring at the

donation site.⁵ Additionally, there are limitations as to which patients may receive autografts and the maximum donation size is limited. Elderly, young, and sick may not be able to donate their own bone tissue for reimplantation, and up to 20% of patients experience complications from the harvesting procedure.⁷

Cadaveric donors overcome one limitation of autologous transplants- constrained supply- by providing allogeneic bone structures capable of bearing load without the restrictions of donor site morbidity. While allografts are the most widely available option for treating long bone defects, fresh allografts are rarely used due to the potential of serious infections such as HIV and Hepatitis C and the presence of immunogenic factors.⁷ Therefore, allogeneic bone requires processing prior to transplantation, which also decreases the desirable biological activity of the tissue.⁷ Still the greater quantity of bone tissue available to surgeons allows them to pack allografts at higher density and promote osteoconduction.²

Substitute materials can be engineered with highly reproducible and tunable properties, which makes it a desirable potential substitute for bone tissue engineering constructs. Researchers are currently investigating *in vitro* strategies in an attempt to develop an alternative that can overcome the complications that arise as a result of the current clinical practices. Generally, the tissue engineering approach involves seeding and growing a cell source on a scaffold and implanting it into the injury site.⁸ While strides have been made in the field of bone tissue engineering research, a major limitation of such 3D constructs is that they have been optimized for a single cell population to enhance and cultivate bone, but lack of inherent vasculature, which thus limits nutrient

transfer. In order to increase the feasibility of cell based tissue engineering strategies, this limitation must be overcome.

The most common component of engineered vascular constructs is the presence of endothelial cells. Many techniques are currently being investigated for the development of vascularized networks with the ultimate goal of developing inherent vasculature within engineered bone tissue grafts. Some of these methods include of *in vitro* or *in vivo* prevascularization of grafts; however due to several disadvantages of these methods, more recent research has focused on 3D printing of vascular scaffolds.

Bone constructs are typically grown in small modules in bioreactor systems to maintain nutrient transfer *in vitro*. A bioreactor is a cell culture system that is used to support or expand a population of cells through dynamic conditions within a controlled environment.⁸ An important benefit of bioreactor systems is their ability to create an *in vitro* environment that mimics the *in vivo* environment of the human body more closely. They do so by providing mechanical stresses and increased nutrient transport via flow. The tubular growth chamber design is more commonly used for the tissue engineering of vascular grafts, where vascular tissue growth is directed either around the outside of a 3D scaffold or around the inner walls of a growth chamber.⁹

The research presented here focuses on the development of an endothelial monolayer that would serve as the foundation for the development of inherent vasculature within these engineered bone tissue grafts. Through the combination of a tubular perfusion system (TPS), computer aided design (CAD), and subsequent 3D printing, we

examine the effects of architecture and shear stress on the formation of endothelial cell monolayer formation.

Chapter 2: Related Literature

Introduction

Vascular networks are an essential element of any biological system, providing cells with oxygen and glucose, while also removing waste products.^{10,11,12} Because of their role in nutrient and waste exchange, they are also the limiting factor within the human body – cells are restricted to a maximum distance of 100-200 μm from the nearest capillary.^{10,11} Despite the overwhelming presence of vascular networks within the body, vascularization of implantable bone grafts remains a major limitation, especially in engineering large scale bone grafts.

While inherent vasculature in engineered bone tissue grafts has yet to be successful on a larger clinically relevant scale, the human body has demonstrated the ability for vascular tissues to spontaneously invade implanted tissue.^{10,13} However, host vasculature invades from the outside of the implanted scaffold inwards; therefore, the time required to achieve sufficient vascularization depends on the thickness of the implant. This spontaneous vascular ingrowth has been measured to occur on the order of a few hundred nanometers per day, thus requiring several weeks to fully vascularize even smaller scale constructs.¹³ During this time, implantable constructs rapidly develop a necrotic core^{10,12,14,15}; the cells that do not die experience a nutrient gradient in which the cells on the outermost aspect of the construct consume greater amounts of nutrients than those cells deeper within the core. The nutrient and

oxygen concentrations decrease toward the center of the scaffold, and eventually drop below the minimum necessary to sustain cell growth.¹³

The need to develop inherent vasculature within engineered bone tissue grafts is apparent, and many different vascularization techniques are currently being developed and tested. It is important to note however, that while there are many different cell culture and tissue engineering strategies used throughout research, many vascularization techniques are incompatible with certain tissue engineering strategies. Because of this disconnect, it is essential to determine which cell culture and construction strategy will work best for the intended application when designing vasculature for bone tissue engineering.

Classical tissue engineering methods generally involve fabrication of scaffolds made of either natural or synthetic materials, and cells of interest are then seeded onto them. Recently, focus has shifted towards the additive layer-by-layer robotic fabrication of 3D scaffolds used in tissue engineering. This technology provides advantages over classical tissue engineering such as higher precision and resolution of printed geometries.¹⁶ Majority of these techniques are based on the use of computer-aided design (CAD) information, which is then converted into a series of cross sectional layers.

Bioreactors have been shown to improve cell seeding efficiency and cell proliferation.⁸ Clinically, one of the most notable benefits of a bioreactor system in the field of tissue engineering is the potential for automation; significant benefits of automated cell culture in a continuously closed system include dramatically

decreasing the risk of contamination, labor, and costs normally associated with *in vitro* cell culture.⁸

The research presented here focuses primarily on the use of tubular perfusion system (TPS) bioreactors, and the vascularization techniques were therefore tuned for use within this bioreactor system.

TPS Bioreactors

Bioreactor Design

Tissue engineering research is increasingly relying on the use of advanced cell culture technologies that provide rigorously controlled cell microenvironments. There are a variety of bioreactors currently being utilized in the field of bone tissue engineering; generally, the three main classes of bioreactors include spinner flasks, rotating wall systems, and perfusion systems, each having their own specific advantages and disadvantages. While there are many different systems, the common goal of all of these bioreactors is to provide controlled mechanical stimuli as well as regulate cell culture media.¹⁷ Mechanical stimuli through flow of media over the scaffolds provides shear stress, while regulation of cell culture media provides sufficient levels of nutrient and waste exchange to all cells in a uniform manner.

Physiologically relevant shear stresses for endothelial cells can be as high as 70 dyne/cm².¹⁸ Therefore, many tissue engineering bioreactor systems seek to expose human umbilical vein endothelial cells to these levels of shear stress, in an attempt to mimic the *in vivo* vascular environment.

While all of the previously mentioned methods of dynamic culture have shown benefits over traditional static culture, success has been modest in spinner flask and rotating wall bioreactors, due to the less-ordered nature of the systems.¹⁷ In its most basic form, as spinner flask bioreactor simply consists of a bone tissue engineering (BTE) scaffold submerged in a flask containing cell culture media. Mechanical stimuli and flow of media is then provided via convection created by the spinning of a stir bar at the base of the beaker. Similarly, a rotating wall bioreactor contains a BTE scaffold in a flask consisting of two concentric cylinders. Here, the flow of media is driven through the viscous effects of media in contact with the both the stationary inner wall, and the rotating outer wall. In both of these systems, convection of media is relegated to the periphery of the constructs, and, while advantageous as compared to static culture, they still require small-scale constructs to allow for full diffusion of the necessary nutrients to the core of these constructs.¹⁷ In fact, cell death is often observed in the core of scaffolds as close as 200 μm from the scaffold surface.¹⁹

Perfusion bioreactors overcome many of the limitations of spinner flask and rotating wall bioreactors, but require a significantly more complex setup. A typical perfusion bioreactor is composed of a media flask, which feeds into a custom-fit reaction chamber, via a tubing circuit. The media is then perfused through a scaffold construct through the use of a pump. These systems have demonstrated increased proliferation and viability of endothelial cells as compared to static culture and other dynamic culture options.⁹ However, in order to ensure that media perfusion actually occurs through the

scaffolds and not around it, the scaffold must be press fit into a custom sized reaction chamber to eliminate any void space between the scaffold and the chamber walls. To overcome these limitations, a system is needed that can provide for increased perfusion of nutrients and increased shear stresses, while eliminating of the need for custom fit reaction chambers.

Advantages of a TPS Bioreactor

Tubular perfusion system (TPS) bioreactors overcome all of these limitations through a unique design. The TPS bioreactor has several important advantages over other existing bioreactor systems. Many perfusion bioreactor systems are composed of customized components that require custom manufacture. The TPS bioreactor, however, is made entirely of off-the-shelf components, making the system easy and cheap to manufacture and modify.⁹ It can accommodate large and small scaffold sizes and multiple scaffolds simultaneously through the adjustment of the growth chamber and medium reservoir size. Furthermore, the TPS bioreactor is easily reproducible, allowing for experimental standardization and consistency, which is important for clinical use.⁹ The medium flow rate in this system may be accurately adjusted between 2 and 240 mL/min. This large flow rate range allows for thorough experimentation of the effect of flow rate and thus shear stress on cell proliferation and differentiation. The bioreactor system can easily and efficiently be sterilized via autoclaving, which will reduce bacterial contamination risk, a common problem in bioreactor systems.⁹

Tissue Engineering Strategies for Vascularized Constructs

All living cells require nutrients for sustained growth and viability. In the body, diffusion of oxygen is limited to only 100-200 μm from the nearest capillary.^{10,11,13} Without functional vascular networks being integrated into 3D engineered tissues, the cells very quickly become necrotic. Despite recent advancements in bone tissue engineering, this diffusion requirement has been a limiting factor, resulting in clinically used implants to be thin or avascular tissues, which can only be vascularized by spontaneous host-capillary invasion.¹³ To address the need for larger-scale tissue constructs, several vascularization techniques are currently under investigation, both *in vitro* and *in vivo*.

The most common component of engineered vascular constructs is the presence of endothelial cells.^{20,21,22,23} Endothelial cells are the foundation of native vasculature; they form a confluent monolayer which lines vascular networks, thus providing an effective barrier to prevent hemorrhage while also allowing for nutrient exchange. Mammalian cells require a constant oxygen supply and waste disposal mechanisms in order to survive. They are located within 100-200 μm of blood vessels, which is the diffusion limit for oxygen. Briefly, vascular networks are formed via a three-phase process. First, endothelial progenitor cells (EPCs) differentiate and proliferate to form the early stages of a capillary network. In this phase known as is vasculogenesis, the primary capillary network is formed. The next phase is angiogenesis, which refers to the formation of new capillary vessels from pre-existing microvessels.¹⁶ During this phase, endothelial cells release matrix metalloproteinases

(MMPs), which serve to degrade the extracellular matrices (ECMs) surrounding the primitive networks formed during vasculogenesis. As the ECM degrades, proliferating endothelial cells migrate into the void, remodeling and elongating the network to form blood vessels. Finally, these blood vessels are remodeled and enlarged into larger vessels and arteries in a process called arteriogenesis.¹³

For thin constructs, there is no significant need for a vascular network formation prior to implantation. Hypoxic conditions within constructs trigger the release of angiogenic growth factors. In combination with the host inflammatory response, these angiogenic growth factors trigger spontaneous host-capillary invasion that provides sufficient vascularization for thin grafts.¹³ Current vascularization strategies are being used in conjunction with this natural response in an attempt to provide sufficiently perfused larger scale vascularized constructs.

One such technique, termed *in vivo* prevascularization, provides implants with a vascular network that spans the major axis of a construct. The advantages of this technique are that it allows for direct microsurgical anastomosis of the construct to the host vasculature, thus resulting in immediate perfusion of the construct. However, this technique requires a host to undergo two separate surgeries. The BTE construct is initially implanted into a healthy region of the body with a major artery. Over a span of several weeks, the graft and the axial vasculature of the artery merge, and once the vascular axis within the graft is sufficient, it is removed from the implant growth site and inserted into the defect site.¹³ While this technique overcomes many of the major limitations of vascularization within BTE constructs, the requirement of two

surgeries, as well as the removal of a major vascular axis from the initial implant site are significant drawbacks. In particular, the requirement for an axial vascular network to be removed from the initial implant site once again places limitations on the size of the implant –as construct size increases, the removal of the initial implant becomes more dangerous.

Another approach utilizes *in vitro* prevascularization. Under the right conditions, EPCs can be directed to differentiate into endothelial cells and form vascular networks. Several design strategies include the addition of growth factors such as vascular endothelial growth factor (VEGF), basic fibroblast growth factor (bFGF), platelet-derived growth factor (PDGF), and transforming growth factor β (TGF- β), among others, to stimulate the formation and remodeling of vascular networks. However, adding too much of a growth factor can result in negative consequences, which includes hemorrhagic vessels, and undesirable differentiation of seeded cells.¹³ While these strategies result in spontaneous, random microvascularization of constructs, they are not sufficient as standalone techniques for the complete vascularization of large scale constructs. Therefore, *in vitro* and *in vivo* prevascularization techniques are often combined with other scaffold-based techniques.

3D Printing of Bone and Vascular Tissue Constructs

To combat many of the issues of the methods mentioned above, 3D printing is often utilized. Here, there are two primary ways in which 3D printing techniques are used to create vasculature in BTE constructs. First, vascular channels can be created simply by

utilizing printing techniques that create user-defined vascular channels and surface topography. The second method, which is also the method most commonly used, is sacrificial molding. Several methods of 3D printing are used to create scaffolds with user-defined geometries and topographical structures. These techniques largely serve the same purpose, with the major differences being the types of materials that can be used with each technique, and the resolution that each method offers. 3D printing can simply be broken down into two primary techniques: stereolithography and extrusion based printing.

Stereolithography involves the use of a liquid polymer resin and a light source. Here, the light source can either be visible light, or ultraviolet (UV) light, depending on the polymer. This technique requires that the polymer have side chains, such as methacrylate groups, which crosslink when exposed to a beam of light. Here, highly focused light causes crosslinking of the photopolymer in a layer-by-layer fashion. Some of the main limiting factors of the stereolithographic approach include cell death caused by UV light, the requirement that polymers be photo-crosslinkable, and scaffold thickness limitations based on the max depth of light penetration.¹⁵ Despite these limitations, important advantages of stereolithography include relatively quick and hands-off production, good resolution, and a high degree of reproducibility.²⁴

Extrusion based printing, which includes techniques such as fused deposition modeling (FDM) and fused filament fabrication (FFF), involves the layer-by-layer addition of material. Extrusion occurs either by drawing the material through a nozzle (FFF), or by applying pressure to force the material through a nozzle (FDM). Under an FDM system, the user can control the temperature of both the print head and build platform, which allows for

multiple material types. Here, the polymer is placed at a temperature that allows for extrusion, while keeping it viscous enough to maintain strand integrity. By tuning the applied pressure and print head movement speed, strand diameter can be carefully controlled, and polymer fibers are deposited layer by layer onto a build plate. Under this system, UV crosslinkable photopolymers can also be used by simply curing each layer with UV light before the next layer is applied. While it is a highly reproducible printing method, this technique is limited by a relatively large resolution, which is driven by the minimum strand diameter, a function of the print nozzle diameter. Further, this technique is limited by the strength of attachment of each layer to the next, as well as the imperfect alignment of each rounded strand to the rounded strand in the previous layer.

For these reasons, sacrificial molding is the more commonly utilized technique for designing and creating vasculature in BTE constructs. Sacrificial molding involves the creation of a user-defined vascular mold. These molds can either be formed by printing a mold within a hydrogel to be filled with a sacrificial material, or by forming the scaffold around the sacrificial template. Major limitations of sacrificial molding include cytotoxicity of sacrificial materials¹⁴, and the challenges associated with creating relevantly sized, interconnected vascular channels.

Another common method of creating sacrificial networks is solvent cast molding. Here, a soluble material such as poly(vinyl alcohol) (PVA), is poured into a mold of the desired shape.¹⁴ The cast is then allowed to solidify, and the tissue construct is built up around it. Once the construct is complete, the cast is sacrificed by simply exposing the construct to a solvent that selectively dissolves the cast.

Alternatively, certain cast materials can be sacrificed at elevated temperatures. These methods are limited by the properties of the sacrificial material, as they must be durable enough to withstand the process of generating the construct, while at the same be easily sacrificed under conditions that are not harmful to the construct or the cells encapsulated within them.

Another way to create sacrificial channels within BTE constructs is through the incorporation of electrospun fibers. Electrospinning is the process of nanofiber formation driven by an electric current applied to a fluid jet composed of a polymer dissolved in a solvent.²⁵ Electrospinning, commonly combined with a polydimethylsiloxane (PDMS) scaffold, allows for the formation of a complex nanochannel network.²⁵ Electrospun fiber materials can then be sacrificed in a variety of

ways, such as the dissolution polyethylene oxide and pullulan fibers in water.^{25, 26}

Despite the vast array of different vascularization strategies currently under investigation, relevantly sized BTE constructs remain largely avascular. Furthermore, the majority of the vascularization techniques produce vasculature on the micro-scale.

However, the diameter of the human femoral artery ranges from about 6 mm to about 10 mm, highlighting the clinical need to develop inherent vasculature on a much larger scale.²⁷

Therefore, a significant need exists to identify strategies that will allow for the vascularization of large-scale BTE constructs.

Oxygen in the HUVEC Niche

In vivo oxygen concentrations are known to influence cellular respiration, proliferation, and viability. Recent studies have examined the influence of oxygen concentration on HUVEC viability and proliferation.

Atmospheric air consists of 20.95% O₂, or roughly 160 mm Hg.²⁸ By the time inhaled oxygen reaches arterial blood, these levels decrease to about 7-12%, and drop further to less than 5% in venous and capillary blood.^{29,30} Further, interstitial oxygen levels within human tissues and organs range from around 2-9%^{28,29}, while average oxygen tensions within healthy bone marrow range from 6-7%^{29,30,31}. Cells within BTE constructs under dynamic culture have been shown to live for up to seven days at oxygen levels just below 4%, whereas identical constructs under static culture yielded 0% central oxygen concentrations in only five days, and marked cell death.³² Additionally, long term exposure to oxygen tensions below 1% result in massive levels of cell death.³³

Effect of Architecture and Topographic Patterns on Endothelial Cell Behavior

Recent developments in micro- and nanofabrication techniques have enabled the fabrication of substrates that are able to mimic the structure and length scale of native topography in two-dimensional and three-dimensional substrates.³⁴ Cells respond to synthetic topographic substrates in a wide array of responses, which depend upon many factors including cell type, feature size and geometry. Three basic nanotopographic geometries that most studies focus on are nanogratings (also known as nanochannels),

nanopost arrays, and nanopit arrays. Nanotopography affects basic cell function in almost all types of mammalian cells.

It is well known that human tissues, including bone and vasculature, exist in the form of naturally well-organized nanoscale topographies for tissue specific function.³⁵ Furthermore, it has been accepted that topography can strongly influence the morphology and orientation of living cells through a phenomenon known as contact guidance and through integrin mediated intracellular tension, which may play an essential role in determining characteristic functions of complex tissues.³⁵ The interaction of mammalian cells with nanoscale topography has proven to be an important signaling modality in controlling cell function – naturally occurring nanotopographic structures within the extracellular matrix present surrounding cells with mechanotransductive cues that influence local migration, cell polarization, and other functions.³⁴ Furthermore, it has been accepted that topography can strongly influence the morphology and orientation of living cells, through contact guidance as well. Contact guidance is a leading example of a naturally occurring phenomenon that is characterized by the response of cells to structures on the micron and sub-micron scale.^{34,35} Synthetically nanofabricated topography can also influence cell morphology, alignment, adhesion, migration, proliferation, and cytoskeleton organization.³⁴

Perhaps the most palpable effect of nanotopography on cell function is the impact upon cell geometry. Many cell types, including endothelial cells, typically respond to nanogratings by simultaneously aligning and elongating in the direction of the grating axis.³⁶

Studies have demonstrated that some nanograting feature sizes induced alignment of cells both parallel and orthogonally to the nanograting axis.^{36,37} Recent studies have also shown that in static conditions that human umbilical vein endothelial cells (HUVECs) were highly aligned on anisotropically nanopatterned scaffolds with nanogrooves, which contrasts their observed random morphology and orientation on flat surfaces.³⁵ Furthermore, it has been shown that HUVECs elongate more strongly on sparser nanogrooved density scaffolds than on relatively denser ones.³⁵ These results indicate that nanopatterned matrices strongly influence the alignment and orientation of HUVECs, which also coincides with the natural orientation of these cells *in vivo*.³⁵ Nanopit features have been shown to elicit a more subtle effect on cellular morphology, and studies of both nanoposts and nanopits, illustrated a decrease spread of cells, although the overall effect of these structures on cell area is unclear.³⁵

Capillary formation of endothelial cells is another important behavior because it is the initial process for formation of new blood vessels. Pioneering research by Bettinger et al. demonstrated that nanotopography had an ability to promote natural capillary formation of endothelial progenitor cells.³⁷

Nanotopography has also been shown to influence attachment and adhesion of cells. Nanogratings generally appear to enhance the adhesion in various cell/biomaterial-geometry combinations. The effect of nanotopography on migration is typically observed in cells cultured on nanogratings. Many cell types, including endothelial cells,

have exhibited biased migration direction in the direction of the grating axis and increased overall migration velocities.³⁶

Additionally, surface topography has also been shown to alter gene expression in endothelial cells. In a co-culture system of HUVECs and human mesenchymal stem cells (hMSCs) seeded on a nanopattern surface, increased Connexin 43 expression compared to the flat surface was seen, indicating that the nanopattern surface may provide an environment more suitable for cell-cell communication, most likely due to the controlled cell shapes.³⁵

It is important that synthesized vascular grafts need to be capable of maintaining the appropriate phenotype of endothelial cells *in vitro*. Phenotypic maintenance of endothelial cells are typically evaluated by the expression of endothelial markers such as platelet endothelial cell adhesion molecular 1 (PECAM1), vascular endothelial cadherin (VE-cadherin), vascular cell adhesion molecule-1 (VCAM-1), and intercellular adhesion molecule-1 (ICAM-1). PECAM-1 plays a role in controlling adhesion between endothelial cells and leukocytes or to adjacent endothelial cells. VE-cadherin mediates intercellular junctions which assist in maintaining the integrity of the endothelial layer. VCAM-1 and ICAM-1 are up regulated during inflammation. Studies have demonstrated that nanotopography has the ability to maintain phenotypes of endothelial cells. Endothelial cells on aligned nanofiber meshes showed an aligned morphology in parallel with nanofibers and expression of three endothelial markers listed above, which represented phenotypic maintenance *in vitro*.³⁷

Although studies have provided important insights into topography as an enabling tool for advanced stem cell-based vascular tissue engineering, further progress is required for the recapitulation of the natural topography observed in the native vascular environment.³⁵ Even with the existing advanced micro- and nanofabrication techniques, it is difficult to prepare highly ordered nanoscale features over a large area.³⁷

Effects of Shear Stress on Endothelial Cell Behavior

Fluidic shear stress is a crucial factor for vascular cell function including proliferation, elongation, and protein secretion. The shear stress applied to the surface of the inner vessel wall ranges from 10 to 70 dyn/ cm² (arteries), or 1 to 6 dyn/ cm² (veins).³⁷ The use of perfusion of medium through an entire cell-seeded scaffolds, enables efficient and uniform mass transfer of oxygen and other soluble factors throughout the entire scaffold, in a similar manner to the role of vasculature in tissues.¹⁸ In addition to its role in mass transfer, the perfusing media produces a frictional force on the surface of the cells known as shear stress. Exposure to high shear stress on the order of 10-70 dyne cm² is normal for vascular endothelial cells, as they make up the inner layer of the arterial vascular network.¹⁸ Because fluid shear stress is an important regulator of cell behavior, many studies have attempted to study its effects on cultivated cells, specifically endothelial cells.

One such study seeded HUVECs in alginate scaffolds at three different levels of shear stress (1-13 dyn/ cm²) for 24h, and found that each shear stress resulted in

different levels of the membrane marker Intercellular Adhesion Molecule 1 (ICAM-1) as well as phosphorylated endothelial nitric oxide synthetase (eNOS).¹⁸ Additionally, Tsuboi et.al. showed that in 2D HUVEC culture, increasing shear stress in the range of 0 to 20 dyne cm² caused increasing levels of ICAM-1 expression in a shear dependent manner as well.¹⁸ Sun et.al. showed that nitric oxide (NO) levels increased when mesenteric arterioles were subjected to shear stresses ranging from 1 to 15 dyne cm².¹⁸ NO is synthesized by eNOS which is activated by its phosphorylation, and therefore there is strong correlation between NO levels and p-eNOS levels in cells. Together, these results indicate that mechanical shear stress via flow rate influences HUVEC gene expression.

Shear stress has been also shown to induce cell sprouting in HUVEC cultures, in a shear stress-dependent manner. Kang et. al subjected HUVECs to a laminar shear stress ranging from 0.12- 12 dyne cm² which illustrated that the invasion distance of HUVEC sprouts into a 3D collagen matrix increased in a shear stress dependent manner¹⁸.

Chapter 3: The Effect of Architecture and Shear Stress on Endothelialization of 3D Printed Vascular Networks

Introduction

With nearly 15 million bone fractures¹ and 1 million bone grafting procedures worldwide⁶ each year, there is a large clinical need for relevantly sized tissue engineered alternatives. Conventional techniques have so far been limited to tissue engineered constructs of less than 11 cubic centimeters³⁸, due to the need for inherent

vasculature for long term graft functionality. While inherent vasculature in larger scale, clinically relevant sized engineered bone tissue grafts has yet to be successful, the human body has demonstrated the ability for vascular tissues to spontaneously invade implanted tissue.^{10,13} However, host vasculature invades from the outside of the implanted scaffold inwards; therefore, these larger scaffolds rapidly develop a necrotic core.^{10,12,14,15}

Classical tissue engineering methods generally involve fabrication of scaffolds made of either natural or synthetic materials and cells of interest are seeded onto them. Recently, focus has shifted towards the additive layer-by-layer robotic fabrication of 3D scaffolds used in tissue engineering. This technology provides advantages over classical tissue engineering such as higher precision and resolution of printed geometries.¹⁶ Nanotopography, including nanochannels, nanopillars, and nanopits have been used to enhance cell proliferation and migration of endothelial cells.

Bioreactors have been shown to improve cell seeding efficiency and cell proliferation.⁸ Clinically, one of the most notable benefits of a bioreactor system in the field of tissue engineering is the potential for automation; significant benefits of automated cell culture in a continuously closed system include dramatically decreasing risk of contamination, labor, and costs normally associated with *in vitro* cell culture.⁸

The research presented here focuses on the use of a TPS bioreactor and 3D printed scaffolds with varying surface topography, including a novel channels and pits

combination, to study the effect of architecture and shear stress on endothelial cell monolayer formation. In our study we hypothesize that our micron scale channels and novel channels and pits combination surface topography will alter surface shear stress in a manner that will enhance proliferation and monolayer formation.

Materials and Methods

SolidWorks Geometry Generation

The use of stereolithography and other 3D printing techniques are advantageous not only because of the high degree of accuracy that they produce, but also because they allow any lab to reproduce the results of another, as long as they have access to the same computer-aided design (CAD) files. However, the CAD files must first be developed. Here, SolidWorks was utilized to create all structures to be printed. First, concept drawings were created that began and ended with a single inlet and outlet, respectively. The overall length of the scaffolds designed was limited by the length of the printer build platform, or approximately 70 mm. Once all of the design parameters were known, the actual CAD model could be developed, as seen in Figures 2-4.

SolidWorks Flow Simulations

Bioreactor studies using three-dimensional scaffolds, provide information about shear stress effects, but additional variables in the system can make it difficult to calculate exact shear stresses cells are exposed to. Complex modeling is required to accurately compute flow rate induced shears for fluid flowing through the

three-dimensional scaffolds with varying surface topography, and these shears are influenced by factors that are difficult to measure including cell growth and extracellular matrix deposition. Additional benefits of running these flow simulations are that you are able to perform a large amount of them in a short amount of time and obtain a large amount of information from each simulation. This allows quick optimization of study designs.

Computational fluid dynamics (CFD) analyses was run utilizing the SolidWorks “Flow Simulation” add-in. SolidWorks develops accurate flow profiles by solving the Navier-Stokes equations for conservation of energy, mass, and momentum, using a finite volume analysis. A unique feature of CFD in SolidWorks is that it automatically determines the fluid volume, making it easy to set up. Further, because CAD models were originally designed in SolidWorks, there was no need to convert files or create entirely new files. However, SolidWorks CFD does require that all fluid volumes be fully constrained, so that the software can determine flow paths.

Boundary conditions were then imposed, assuming fully developed flow. For each experimental group, flow simulations were performed at 0.5, 1, 2, 5, 10 and 20 mL/min, which was imposed at the inlet boundary, and an environmental pressure (1 atm) was imposed as the outlet boundary condition. Finally, flow of media was modeled as water and blood at 37 °C, gravity was imposed to account for the vertical orientation of the reaction chamber within the incubator, and mesh resolution was set to “4”. This resolution value was determined to give the best results within a reasonable time; the average calculation time was about 20 minutes. Overall, several

assumptions are made by this modeling technique – it assumes 37 °C, fully developed flow at the inlet, finite volume, and boundary conditions for both fluid volume rate and environmental pressure.

Experimental Group Determination

For the bioreactor study which utilized 3D printed scaffolds, the experimental groups were based on cylindrical diameter and surface topography. Cylinders were divided into Groups 1-3, each with a different inner diameters, 4.5mm, 10 mm, and 16 mm, respectively (Figures 2-4). Scaffold diameters were chosen so that the scaffolds would fit flush within the tubing sizes available for use in the bioreactor, ensuring that all media flow went through, not around the scaffolds. The length of the cylinder in each group was calculated so that the cylinders in each group would have the same total inner surface area. Static control samples, one corresponding to each dynamic experimental group were used as controls. This group altogether are referred to as “Static Control” in all relevant graphs and tables. All other groups were cultured in a TPS bioreactor.



Figure 2: Group 1 diameter dimensions. a. Inner and outer diameters (mm). b.

Length of cylinder (mm).

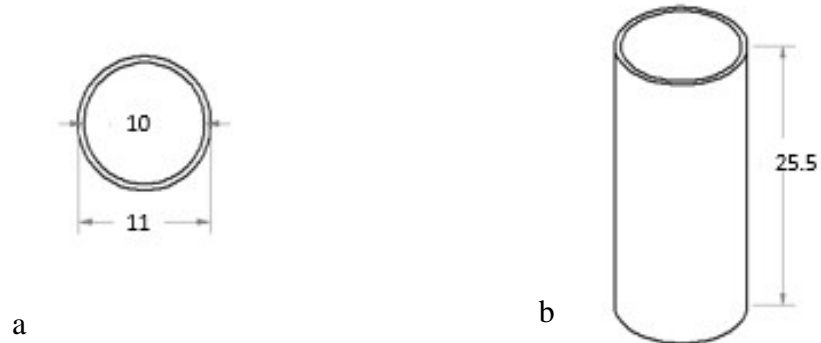


Figure 3: Group 2 diameter dimensions. a. Inner and outer diameters (mm). b.

Length of cylinder (mm).

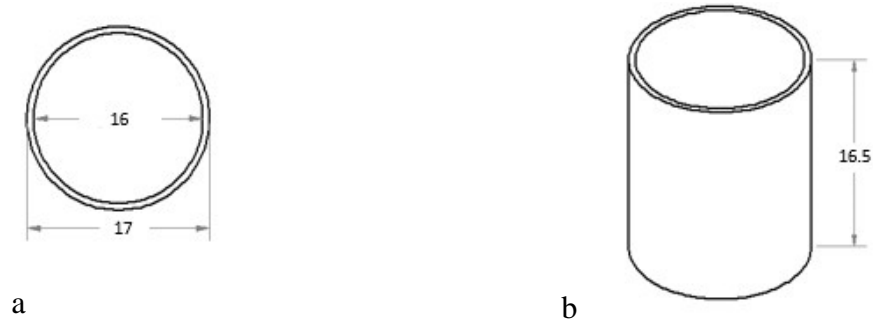


Figure 4: Group 3 diameter dimensions. a. Inner and outer diameters (mm). b.

Length of cylinder (mm).

Additionally, within each group, three different surface topographies were analyzed – no pattern flat surface, channels, and channels & pits (Figure 5). The channels seen in Figure 5 were 0.400 mm in height, and 0.400 mm in width. 0.400 mm spacing was also used between each channel. The pits in Figure 5b were 0.800 mm in depth and 0.400 mm wide. They were also spaced 0.400 mm from each other.

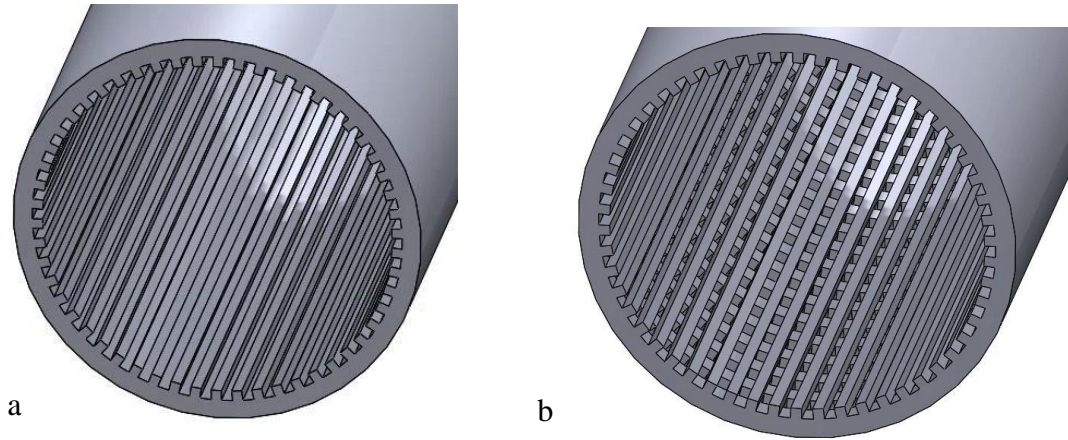


Figure 5: a. Channel surface topography. b. Channel and pits combination surface topography.

Initially, smaller topographical features were designed and created to more closely mimic the nanotopography of the *in vivo* vascular environment; however, these designs failed to successfully print due to the resolution of the 3D printer, so the channels and pits topography was scaled up to the dimensions shown in Figure 5.

For studies under static conditions as well as dynamic growth chamber studies under flow, 2D printed scaffolds were used. Experimental groups were divided based on surface topography: no pattern flat surface, channels, and channels & pits.

3D Printing

All 3D printing was completed using a Digital Light Processing (DLP) stereolithography printer (EnvisionTec). A clear polymer, EShell 300 (EnvisionTec) was chosen for both the perfusion network, and the connectors. EShell 300 is a clear, photo-crosslinkable polymer, due to the functionalization of both acrylate and methacrylate groups. Tuned by the manufacturer for use with EnvisionTec DLP

printers, it provides resolutions on the order of 100-150 μm , and is designed as a bioinert polymer for commercial hearing aid manufacturing. This material was chosen for several reasons: it is well characterized by the company (EnvisionTec), cheap, and easy to obtain.

First, CAD files of networks and connectors were imported as .stl files to Magics, an STL editor software. Parts were rotated and translated as necessary to align them to the build plate. They were then “fixed” using the built-in features of Magics to correct overlapping geometries, holes, etc. From here, support structures were generated within Magics. Support structures attach to the print files, and allow for rounded structures to adhere to the build platform, and ensure that the construct did not collapse during the build process. Part files and support structures were then imported to Perfactory RP (EnvisionTec), a software which allows the user to translate .stl files to the proper format to be used with Perfactory printers. Here, parts can be angled and rotated to allow for optimal use of build platform space.

Additionally, build style is selected here. The EnvisionTec default build style for EShell 300 was used, with a step size of 50 μm . The Perfactory 4 (EnvisionTec) was the DLP printer utilized for all prints. Ensuring that the projector light type was set to “UV,” the intensity was calibrated to 180 mW/dm², as is recommended by the manufacturer. A 48-field calibration was used to achieve the highest degree of accuracy. Once calibrated, the flat calibration plate was exchanged in favor of the material tray, which features silicone rubber walls to allow for the containment of the liquid EShell 300 resin. From here, files were transferred to the printer, and the printer

was left to run its course. Build times for job files ranged from 2-7 hours. Once the printer finished, the build platform was raised and prints were removed from the build platform using a putty knife. At this point, prints were soft-cured, meaning that they maintained their shape, but were still very soft and sticky to the touch due to the presence of partially cured polymer. Prints were cleaned by spraying them gently with 99% isopropanol, and then placed into an isopropanol bath on a shaker platform for approximately 15 minutes. This cleaning process served to remove excess polymer, and ensure that pits and channels were not occluded.

Following the cleaning process, parts were dried with compressed air, and support structures were trimmed using a razor blade and an X-ACTO knife. Parts were washed and dried again, and cured through the application of 1500 flashes in a light polymerization chamber (EnvisionTec). Remaining support structure debris was then sanded down to yield smooth surfaces. Constructs with and without support structures can be seen in Figure 6.

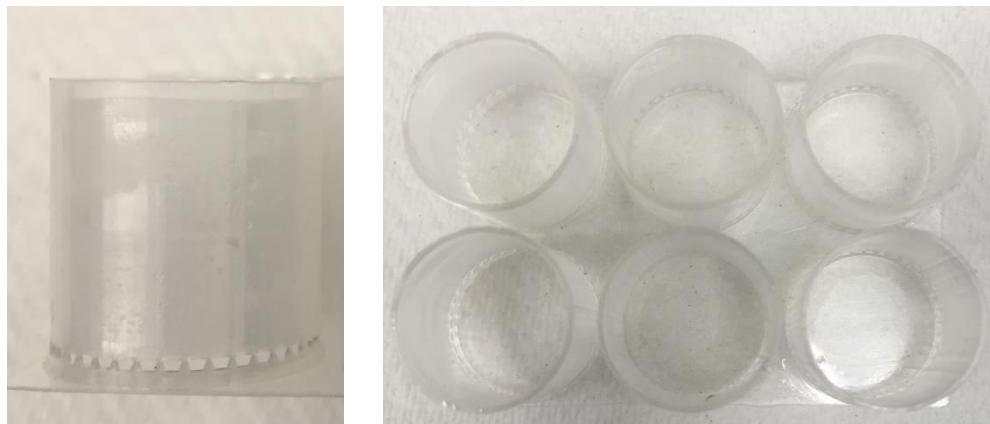


Figure 6: Example of EShell 300 Clear Print a. Side view with supports. b. Top view with supports.

EShell Sterilization

Because EShell parts cannot be autoclaved, the 3D printed scaffolds were sterilized by a sterilization-rehydration protocol. First, five sterile beakers were sprayed with 70% ethanol and transported to a sterile hood. Similarly, an unopened 1 gallon jug of 100% ethanol was sprayed into the hood, along with sterile phosphatebuffered saline (PBS, pH 7.4). The five beakers were filled with five different solutions (one each), of 100% PBS, 25%-75% ethanol-PBS, 50%-50% ethanol-PBS, 75%-25% ethanol-PBS, and 100% ethanol. All parts to be sterilized were submerged in 100% ethanol and exposed to UV light for 15 minutes. Then, parts were gradually rehydrated in PBS by soaking them in increasing percentages of PBS, for five minutes per beaker, all while exposed to UV. Once the parts reached the final, 100% PBS, solution, they were removed using sterile tweezers and stored submerged in PBS in sterile 50 mL Falcon tubes.

Cell Culture

Human umbilical vein endothelial cells (HUVEC) (Lonza Inc., Walkersville, USA) were purchased and cultured according to standard protocols.¹⁶ Plated cells were kept at 37 °C in a 5% CO₂ atmosphere. Endothelial basal media (EBM-2) (Lonza Inc.) combined with the EMB-2 bullet kit (Lonza Inc) was used to make media changes to cell culture plates every two days as well as one day prior to experimentation in order to ensure 100% confluency and high cell yield. All cells used in the study were passage 3 or 4. HUVECs were chosen as the cell line to use in these studies as they are well characterized, easy to obtain, and grow quickly.

Fibronectin Coating and Cell Seeding

Prior to cell seeding, samples were coated overnight with 3 ug/uL fibronectin concentration in 50 mL Falcon conical tubes on a rotator, which allowed for a more even distribution of the fibronectin on the scaffolds. Fibronectin coating was used to enhance cell adhesion rates on the EShell scaffolds. Experiments were done using a cell seeding concentration of 5000 cells/ cm². Following fibronectin coating, scaffolds were seeded overnight in 37°C incubator before studies were begun.

Static 2D Setup

Static studies were performed with 2D disc shaped constructs with no pattern flat surfaces. The prints were placed in a petri dish and submerged with media until assessed at various time points; the setup can be seen in Figure 7 with the media represented as the pink fluid and the print as the gray flat disc. Three time points were assessed using live dead stain on days 1, 3, and 7.

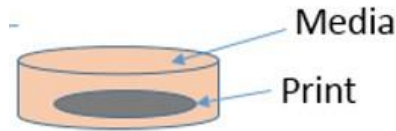


Figure 7. Static 2D setup in a petri dish.

Dynamic Growth Chamber Setup

Since microscopic imaging on 3D constructs is challenging, we used 2D EShell 300 clear circular prints under the same shear stress to perform viability and morphological analysis. Prints had varying surface topography – no pattern flat surface, channels only, or channels and pits combination. This setup was thus used as a

representation of the inner surface of the 3D scaffolds in the TPS bioreactor experiments. The setup as shown in Figure 8, uses a syringe pump (Harvard Apparatus) that held a 10mL syringe loaded with media. This allowed for controlled flow rate of media into the growth chamber apparatus at 0.005 mL/min. The shear stress on the print could be controlled by choosing one of the three gaskets available for this growth chamber model labeled A, B, and C. The gaskets vary in thickness and flow path widths. The gasket that was chosen for this study was gasket A, which has a thickness of 0.005 inches and a flow path width of 0.25 cm; our reason for this selection is that gasket A allowed us to reach the shear rate that we wanted, which was 5 dyn/ cm², while also reducing the number of times the syringe had to be reloaded with media by using a lower flow rate to obtain the shear stress we wanted. The growth chamber was attached to a vacuum line, which was important for keeping the seal tight around the cell culture area on the print.

These studies were performed for a 24 hour period, at which time the samples were analyzed for attachment efficiency, orientation, morphology and viability.

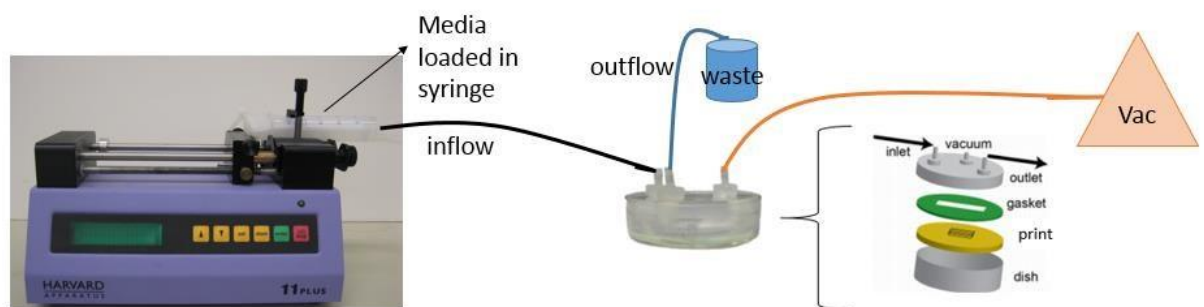


Figure 8. Growth Chamber Setup.

Bioreactor Setup

A Masterflex L/S peristaltic pump (Cole-Parmer) drives the flow of media throughout the bioreactor. Masterflex two stop L/S 14 tubing is fed into the pump.

Tubing is connected using silver ion-lined microbial resistant tubing connectors (Cole Parmer) of varying sizes. The platinum cured silicone tubing was chosen for its low chemical leachability, minimal protein binding, and high gas permeability to allow for easy exchange of carbon dioxide and oxygen.

All tubing and connectors were first autoclaved, with the exception of EShell parts, which were sterilized as described above. Using appropriate 1/8-1/8” connectors, 1/8” ID tubing extends from both ends of the pump tubing, and one end is fed into the media flask, which is stopped with a rubber stopper with two holes for tubing. Each line on the bioreactor featured tubing sizes ranging from 1/8” to 3/4”, which allowed the cylinders were varying diameters from all groups to be run on the same line simultaneously. In each tubing segment, shown as green in Figure 9, two scaffolds would be present. Connectors, shown in pink in Figure 9, were used to connect segments to one another and prevent any potential leaking. The final combination of connectors and the perfusion network resulted in a system that allowed for the direct perfusion of media throughout the interior of the designed constructs.

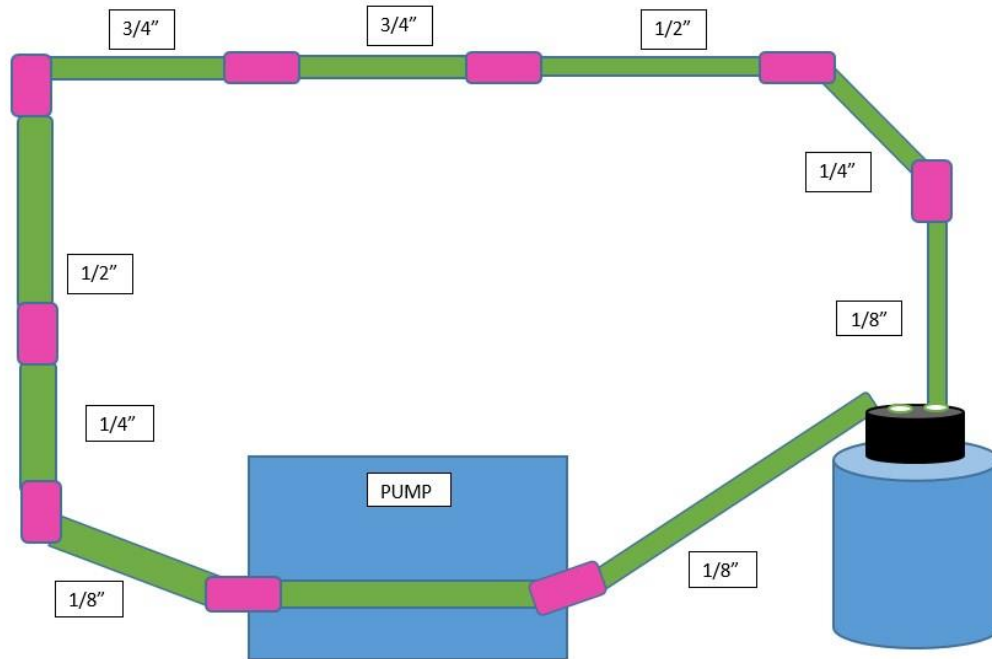


Figure 9: Model of bioreactor setup showing one complete tubing line circuit.
Green represents tubing containing scaffolds. Pink represents connectors
between tubing segments. Blue cylinder on the right represents media reservoir.

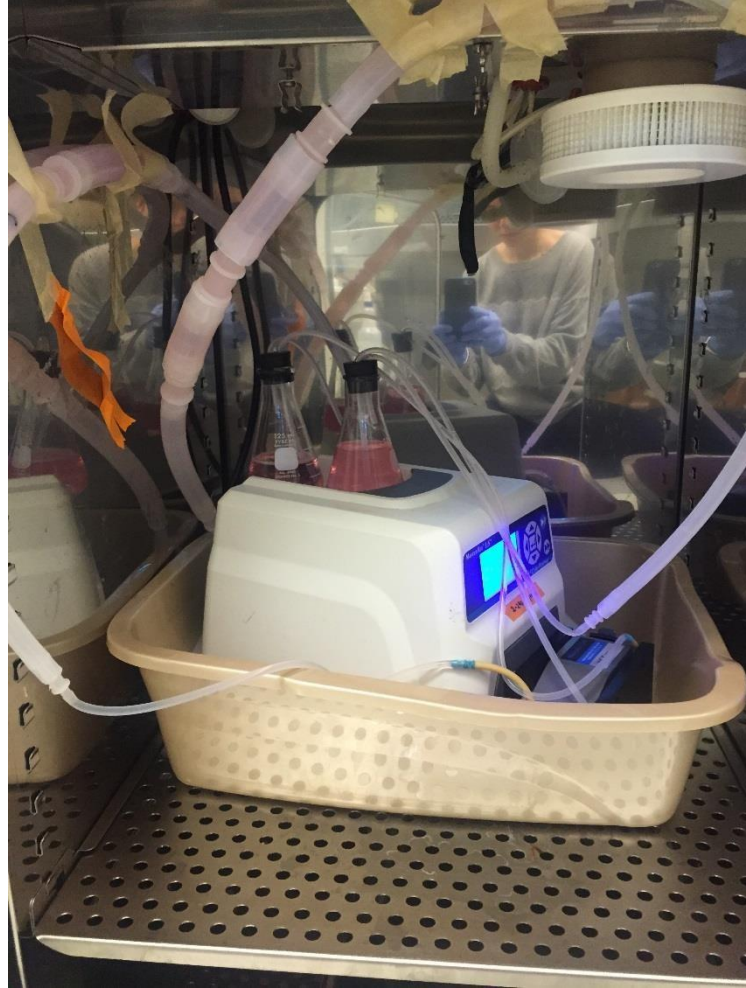


Figure 10: Bioreactor setup with lines in parallel.

The bioreactor setup was designed in a way that all experimental groups could be tested simultaneously, under the same flow conditions. All bioreactor groups were run in parallel on the same pump (Figure 10). Once set up in a sterile hood, the entire system is then transported to a cell culture incubator at 37 °C, with 5% CO₂. Each tubing line had its own separate media flask, filled with 250 mL of perfusion media as demonstrated by Figure 10, which features the complete setup installed into the incubator at 37 °C. The medium is withdrawn and replaced from the reservoir through two tubes that penetrate the stopper and changed every 3 days by moving the bioreactor into a sterile

culture hood, removing the medium in the reservoir and replacing it with a fresh medium. This provides for a change of 80% of medium. All groups were exposed to a flow rate of 20 mL/min.

Viability, Morphology & Proliferation Analysis

Cell viability was assessed using a live dead assay following standard protocols as described previously.⁹ Samples were incubated in 2 μ M ethidium homodimers and 4 μ M calcein AM (Molecular Probes) for 30 minutes. Fluorescent images were then taken using a fluorescent microscope (Axiovert 40 CFL with filter set 23; Zeiss, Thornwood, NY) equipped with a digital camera (Diagnostic Instruments 11.2 Color Mosaic, Sterling Heights, MI).

For the analysis of growth chamber and static samples, viability, attachment efficiency, morphology and proliferation of HUVECs were assessed. Attachment efficiency was assessed on Day 1 (24 hr) using five images, one from each quadrant as well as one image from the center of the construct. Images were taken on Days 1 (24h), Day 3 and Day 7 for morphology analysis, which included aspect ratio and orientation of cells. Proliferation was assessed on Day 7.

For the calculation of the aspect ratio, twenty or more fluorescent images were taken at 20x. Aspect ratio is normally calculated as width divided by height (Figure 11). However, in our study, orientation in static conditions was irrelevant, so we could simplify our calculation to dividing the longer side, side 1, by the shorter side, side 2 (Figure 12). Each side length was measured using the ImageJ measurement

tool.

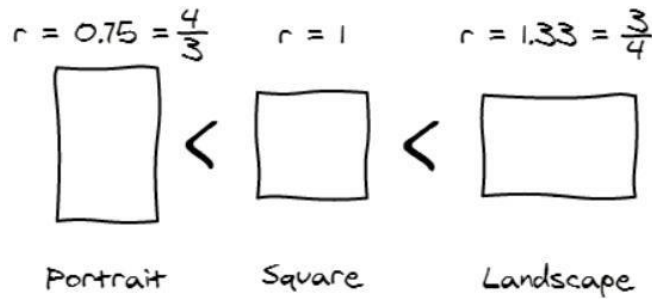


Figure 11: Aspect ratio calculated by dividing width by height.

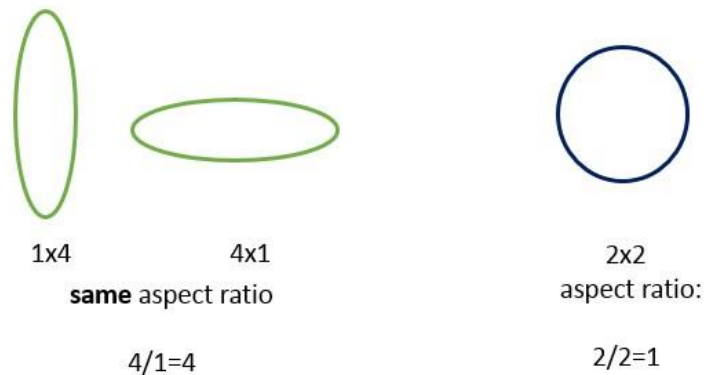


Figure 12: Aspect ratio calculated by dividing longest side by shorter side, as done in this study.

Attachment efficiency in the table below was calculated by dividing the total cells counted on Day 1 (24h) by the original number of cells seeded on the print, and then multiplying by 100 to get the attachment efficiency value in a percentage.

For bioreactor samples, proliferation, morphology and viability were assessed on Day 7. A static sample for each experimental group served as the negative controls.

All microscopic images analysis was performed using the ImageJ software.

Uniform image processing (i.e. brightness/contrast modifications) on ImageJ ensured that

all images were processed uniformly to prevent misrepresentation of data. Images were first processed, and then live dead images were merged.

Cell counts were obtained from individual live or dead images at 2.5x, 10x and 20x magnification. The images were counted using the cell counter feature on ImageJ.

DNA Analysis

DNA was extracted at the Day 7 time point for the bioreactor study samples using the following procedure previously described in the literature.⁹ Isolated cell pellets were resuspended in 200 uL of PBS isolated using a DNeasy Tissue Kit (Qiagen, Valencia, CA) following standard protocols to produce 400 uL of eluate. Double stranded DNA was then quantified by mixing 50 uL of DNA eluate with 50 uL of diluted Quanti-iT Pico Green dsDNA reagent (Molecular Probes, Carlsbad, CA), incubating for 5 min in the dark and measuring fluorescence using an M5 SpectraMax plate reader (Molecular Devices, Sunnyvale, CA) with excitation/emission of 480/520 nm. All samples were performed in triplicate (n=3).

Statistical Analysis

For statistical analysis in the static conditions and dynamic growth chamber studies, a two sample T Test was used with a 95% confidence level. For statistical analysis of the TPS bioreactor studies, a one way ANOVA was used.

Results

SolidWorks CFD Analysis

The purpose of the SolidWorks flow simulations is to determine what flow rate to use in bioreactor study to obtain physiologically relevant shear stress. CFD results from SolidWorks flow simulations demonstrate flow velocity profiles and shear stresses similar to average velocities in previous TPS bioreactor experiments.⁹ Furthermore, flow profiles for all experimental groups examined varied by diameter and topography. Surface plot contours of shear stress (Figure 13), flow trajectories of the flow velocities (Figure 14) and surface shear stress results (Tables 1-3) were obtained for each sample under each flow rate simulation. More images of these flow simulations can be found in Appendix B. Looking at Figure 14, it is important to note that the effect of surface topography on shear stress profiles can be seen – the pits pattern at the flow rate shown has a lower shear stress than the surrounding scaffold area. Thus, even prior to starting the bioreactor study, we were able to see the influence of surface architecture on the shear stress profile sensed by endothelial cells on the construct's surface.

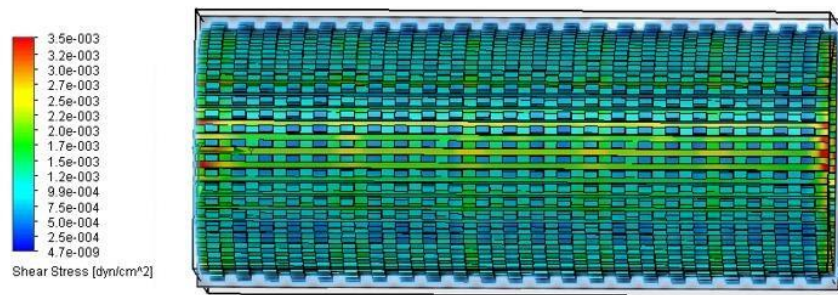


Figure 13: Surface plot contour of shear stress, group 2 diameter with channels and pits, flow rate of 10 mL/minute.

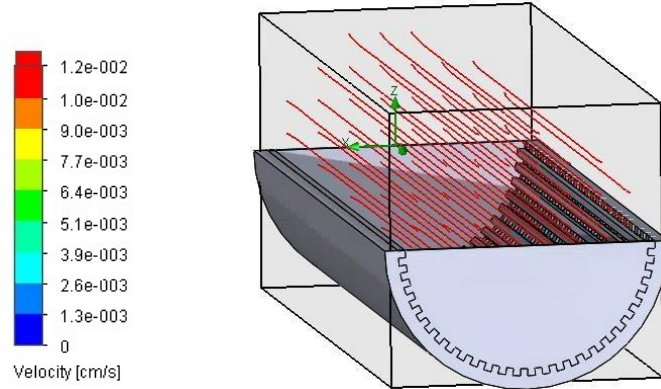


Figure 14: Flow trajectory of group 2 diameter with channels and pits, flow rate of 10 mL/minute.

Group	Flow Rate (mL/min)	Surface topography pattern	Minimum shear stress (dyn/ cm ²)	Maximum shear stress (dyn/ cm ²)	Average shear stress (dyn/ cm ²)
Group 1 diameter (4.5 mm)	0.5	No pattern /flat surface	0.00837	0.04849	0.01712
	1		0.10581	0.46391	0.19925
	2		0.19041	0.76888	0.34971
	5		0.40017	1.78646	0.73020
	10		0.70159	3.3068	1.27418
	20		1.25094	6.13288	2.23082
	0.5	Channels only	0.00050	0.19241	0.01329
	1		0.00100	0.35354	0.02658
	2		0.00220	0.61852	0.05283
	5		0.00220	0.61852	0.05283
	10		0.01243	2.28568	0.21712
	20		0.02259	4.04388	0.37994
	0.5	Channels + Pits	0	0.05294	0.00591
	1		5.385E-07	0.03077	0.00279
	2		0	0.02543	0.00263
	5		0	0.06239	0.00714
	10		0	0.12492	0.01426
	20		0	0.29339	0.02950

Table 1: Surface shear stress results for group 1 diameter experimental groups in bioreactor study.

Group	Flow Rate (mL/min)	Surface topography pattern	Minimum shear stress (dyn/ cm ²)	Maximum shear stress (dyn/ cm ²)	Average shear stress (dyn/ cm ²)
Group 2 Diameter (10 mm)	0.5	No pattern /flat surface	0.00035	0.00076	0.000549
	1		0.00076	0.00149	0.001103
	2		0.00155	0.00295	0.002209
	5		0.00400	0.00713	0.005533
	10		0.00839	0.01387	0.01108
	20		0.01722	0.02705	0.02222
	0.5	Channels only	5.56E-08	0.01117	9.85E-05
	1		9.30E-08	0.02058	0.00020
	2		9.27E-08	0.03804	0.00041
	5		1.40E-07	0.08591	0.00107
	10		1.14E-06	0.15947	0.00222
	20		5.06E-07	0.29634	0.00457
	0.5	Channels + Pits	4.70E-09	0.00347	7.36E-05
	1		0	0.00616	0.00015
	2		0	0.01126	0.00032
	5		0	0.02702	0.00088
	10		0	0.05184	0.00183
	20		0	0.09878	0.00378

Table 2: Surface shear stress results from group 2 diameter experimental groups in bioreactor study.

Group	Flow Rate (mL/min)	Surface topography pattern	Minimum shear stress (dyn/ cm ²)	Maximum shear stress (dyn/ cm ²)	Average shear stress (dyn/ cm ²)
Group 3 diameter (16 mm)	0.5	No pattern /flat surface	4.09E-05	0.00021	0.00012
	1		0.00011	0.00040	0.00025
	2		0.00027	0.00078	0.00051
	5		0.00069	0.00192	0.00127
	10		0.00143	0.00376	0.00255
	20		0.00299	0.00731	0.00514
	0.5	Channels only	0	0.00045	3.45E-05
	1		0	0.00094	7.26E-05
	2		0	0.00094	7.26E-05
	5		0	0.00393	0.00038
	10		4.60E-07	0.00771	0.00080
	20		0	0.01497	0.00162
	0.5			0	0.00036

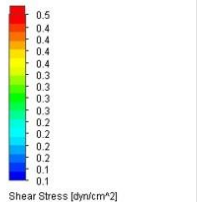
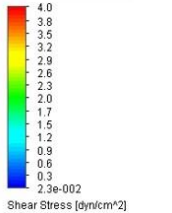
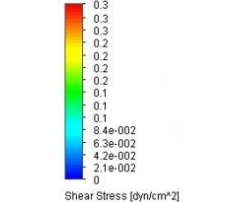
1	Channels + Pits	0	0.00073	5.09E-05
2		0	0.00143	0.00011
5		6.75E-08	0.00351	0.00027
10		2.36E-08	0.00693	0.00058
20		0	0.01351	0.00122

Table 3: Surface shear stress results from group 3 diameter experimental groups in bioreactor study.

The surface shear stress results in Tables 1-3 were used to determine which flow rate to use in the TPS bioreactor study since we wanted to use as close to a physiologically relevant shear stress as possible, while also not using such a high flow rate that the flow could potentially shear off the fibronectin coating. In all Tables 1-3, as the flow rate increased in every experimental group from 0.5 mL/minute to 20 mL/min, the average shear stress increased as well. Using the conclusions we made from these surface shear stress results, we decided to use 20 mL/minute flow rate because it had the widest range between the minimum and maximum shear stress in each group, which would allow us to see the largest variation of shear stress in a single bioreactor study. Additionally, out of all the flow rates simulated, 20 mL/min produced shear stresses closest to the physiologically relevant range, and thus was chosen as the flow rate to use in our TPS bioreactor study.

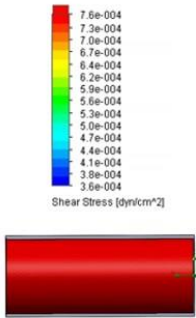
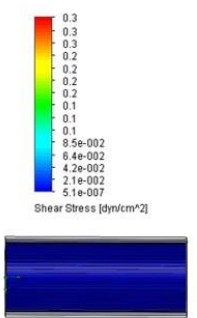
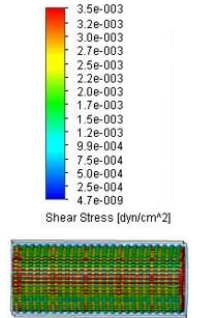
Focusing in on the 20 mL/minute flow rate shear stress results we saw that in the group with the smallest diameter (Figure 15), the no pattern group had the highest shear

stress average of 2.23 dynes/cm², which decreased in the channels topography group to 0.37 dyne/cm² and even further in the channels and pits topography group to 0.29 dyne/cm². Thus, the general trend seen here is that with increasing surface topographical complexity there is a decrease in the average shear stress values. This same trend was seen in the medium sized (Figure 16) and largest sized (Figure 17) diameter groups as well.

	No Pattern	Channels	Channels & Pits
Group 1 Diameter (4.5 mm)			
	Shear Stress (dyn/cm ²): Range: 1.25094-6.13288 Average: 2.23082	Shear Stress (dyn/cm ²): Range: 0.02259-4.04388 Average: 0.37994	Shear Stress (dyn/cm ²): Range: 0-0.29339 Average: 0.02950

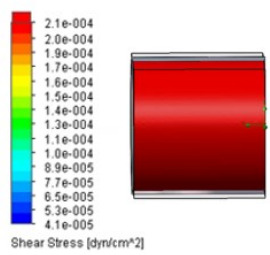
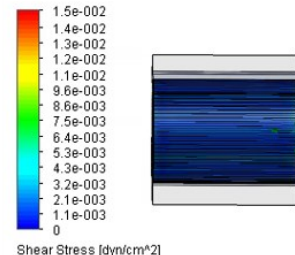
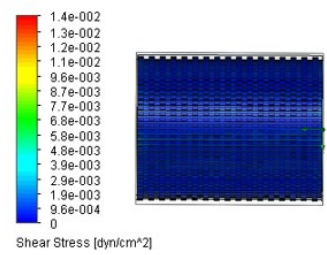
Average shear stress

Figure 15. Group 1 diameter shear stress results for each experimental group at 20 mL/minute flow rate.

	No Pattern	Channels	Channels & Pits
Group 2 Diameter (10 mm)			
	Shear Stress (dyn/cm ²): Range: 0.01722-0.02705 Average: 0.02222	Shear Stress (dyn/cm ²): Range: 5.06E-07-0.29634 Average: 0.00457	Shear Stress (dyn/cm ²): Range: 0-0.09879 Average: 0.00378

Average shear stress

Figure 16. Group 2 diameter shear stress results for each experimental group at 20 mL/minute flow rate.

	No Pattern	Channels	Channels & Pits
Group 3 Diameter (16 mm)			
	Shear Stress (dyn/cm ²): Range: 0.00299-0.00731 Average: 0.00514	Shear Stress (dyn/cm ²): Range: 0-0.01497 Average: 0.00162	Shear Stress (dyn/cm ²): Range: 0-0.01351 Average: 0.00122

Average shear stress

Figure 17. Group 3 diameter shear stress results for each experimental group at 20 mL/minute flow rate.

Static Conditions Endothelial Cell Analysis

The purpose of the static 2D studies was to assess endothelial cell behavior in static conditions in order to serve as comparative baseline values for the dynamic studies. Live/dead images were taken on Day 1, 3, and 7 of the no pattern flat surface 2D prints in the static conditions study. Cells at the day 1 time point were consistently more rounded (Figure 18), with an aspect ratio closer to 1 (1.75 ± 0.5), while cells on day 3 (Figure 19) were much more elongated with an aspect ratio much greater than 1 (8.3 ± 3.7). Using the aspect ratio calculation method previously described, we calculated average aspect ratios on Day 1 and Day 3 for static conditions samples, as shown in Figure 20. The aspect ratio is notably larger in the day 3 samples, and when using a 95% confidence interval on a 2 sample T-test, the difference was statistically significant ($p < 0.05$). Thus, as time increased the aspect ratio of the HUVECs increased significantly, thus indicating elongation of the cell morphology over time.

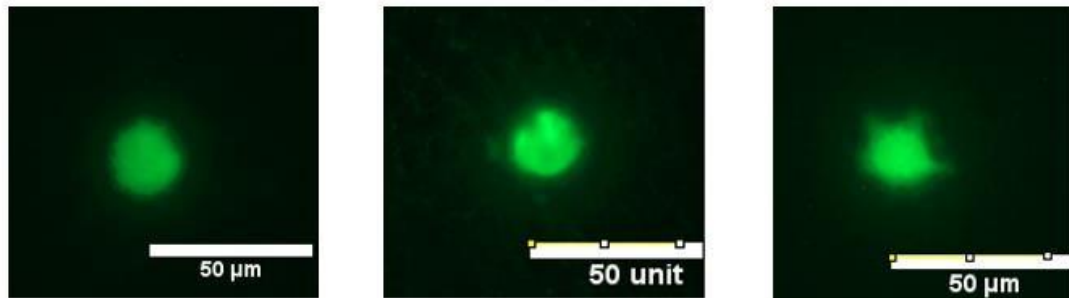


Figure 18: Selected images of HUVEC on day 1 at 20x. Live dead stain, green: calcein stain for live cells.

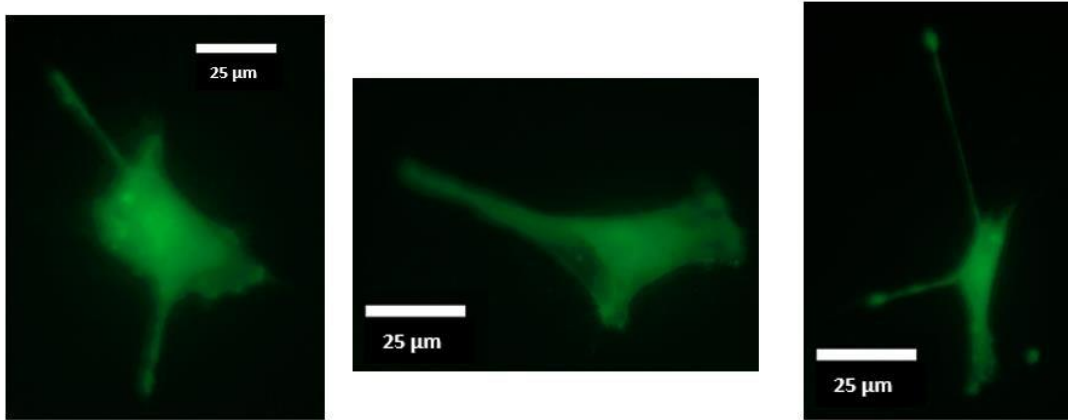


Figure 19: Selected images of HUVEC on day 3 at 20x. Live dead stain, green: calcein stain for live cells.

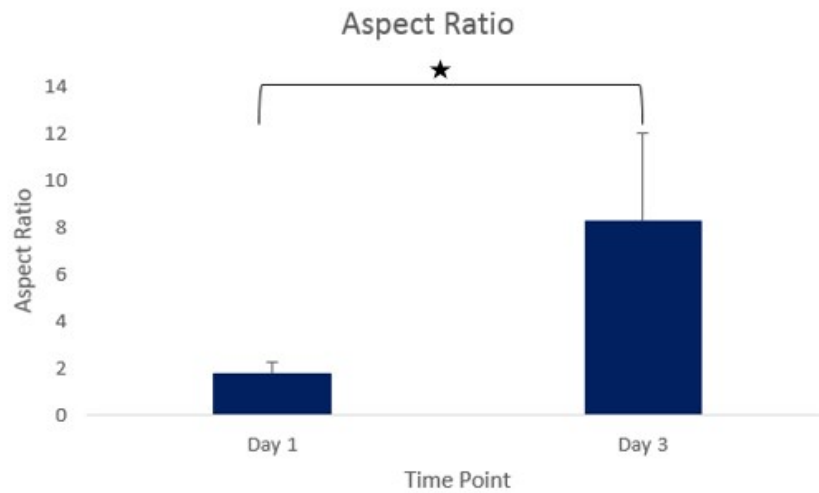


Figure 20: Aspect ratio of HUVEC on day 1 versus day 3. * indicates $p < 0.05$.

HUVEC attachment efficiency was also calculated on day 1 using live/dead imaging. With a cell seeding density of 5000 cells per cm^2 , the average attachment

efficiency was calculated to be 23% +/- 6 (n=5 samples). Additionally, although endothelial cell binding to fibronectin as a substrate is well established, coating of EShell polymer with fibronectin in order to provide proper endothelial cell attachment has not previously been demonstrated. The data presented here illustrates that fibronectin can successfully be used to enhance adhesion of HUVECs on the EShell polymer.

Proliferation of HUVECs was assessed on day 7. Compared to day 1 average cell count per cm² of 226 +/- 55 (n=5), day 7 average cell counts increased to 48493 +/- 1442 cells per cm² (n=3). This difference is statistically significant with a confidence level of 95%, using a 2 sample T-test (p = 0.042), thus indicating proliferation of the HUVECs has occurred over the 7 day study (Figure 21).

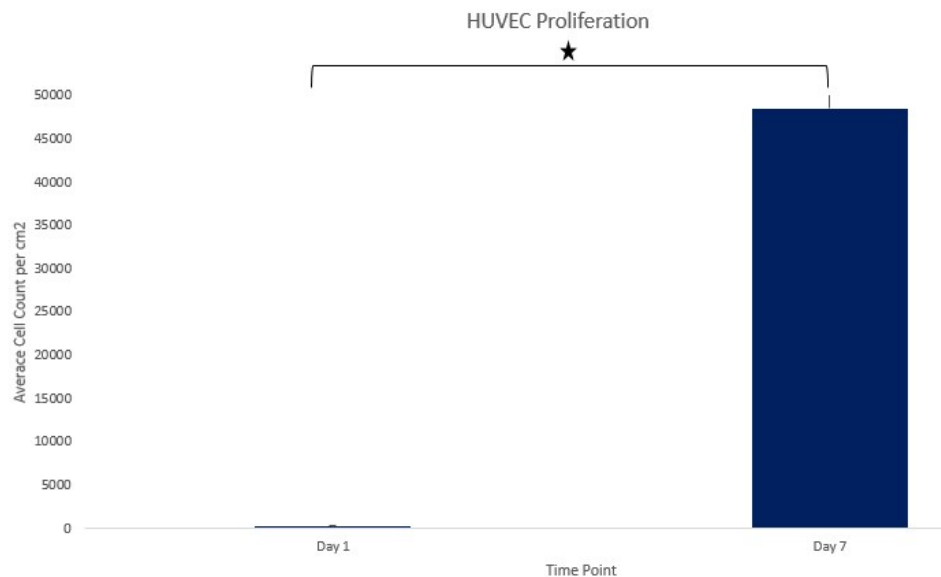


Figure 21: Proliferation of HUVECs from day 1 to day 7. * indicates p < 0.05.

Dynamic Growth Chamber Endothelial Cell Analysis

The purpose of the dynamic growth chamber experiments was to provide a proof of concept study to assess the effects of shear stress on HUVECs prior to

beginning the more complex TPS bioreactor setup. For the dynamic growth chamber study, attachment efficiency was calculated after a 24 hour cell seeding period in static conditions. The average attachment efficiency was 16 % +/- 7, which is similar to that of the static condition study average attachment efficiency, which is expected since both were calculated after static conditions. The 24 hour seeding period in this study was considered to be day 0 of the study. Day 1 time point in the dynamic growth chamber study was after 24 hours under flow. When comparing Day 1 (24h) time point data of average cell count per cm² between the static study (n=5 samples) and the dynamic study (n=4 samples) after 24 hours of flow, the dynamic study had a statistically significantly large average cell count per area than the static group (p = 0.046) (Figure 22).

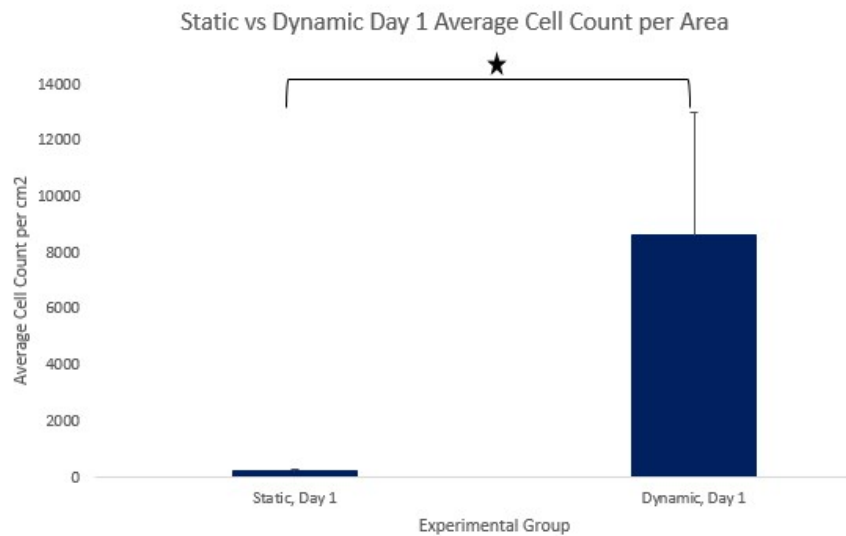


Figure 22: Static versus dynamic, no pattern group HUVEC cell density on day 1. * indicates p < 0.05.

This data suggests that the dynamic flow conditions may enhance or promote cell proliferation. However, when comparing the aspect ratio of these same two groups, there was no statistical difference between them ($p=0.927$), with both groups having an average aspect ratio near 1, meaning the majority of the cells were rounded. On the no pattern flat surface 2D scaffolds under dynamic flow, no orientation to the direction of flow was seen (Figure 23).

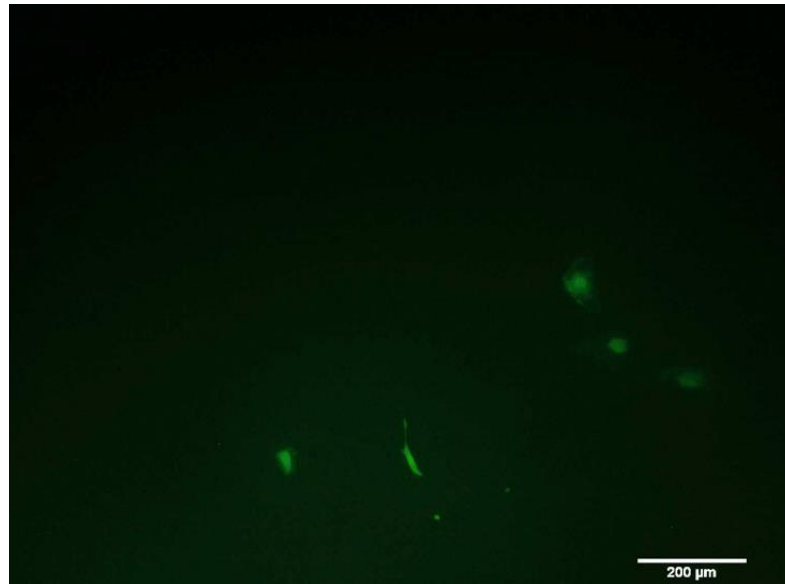


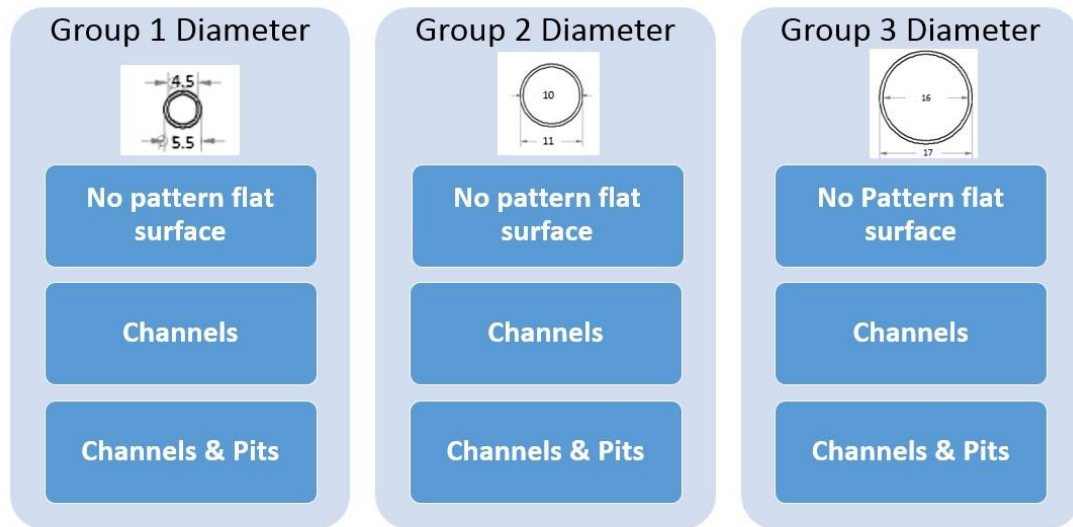
Figure 23: Random orientation under flow, no pattern flat surface group. 10x.

The original design dimensions of our topographical pattern, specifically the channels, was on the 100 to 150 micron scale, where this height would have fit the growth chamber apparatus. However, due to resolution limitations of the printer, the final design ended up being on the 400 micron scale. Although initial runs were tried,

due to the gasket and larger channel size, there was a leak, likely due to the height of the channel pattern that prevented the vacuum from creating a complete seal around the print and gasket. So, alternatively, we moved forward to perform dynamic flow effect analysis in the TPS bioreactor model.

***In Vitro* Bioreactor Endothelial Cell Analysis**

The purpose of the bioreactor study was to assess the effect of architecture and shear stress on endothelial cell monolayer formation. The experimental groups assessed in the bioreactor study are shown below in Figure 24. The experimental groups consisted on an overarching dynamic group with corresponding static controls. There was a static control for each specific dynamic experimental group. Within the dynamic group, three different diameters were tested: 4.5 mm, 10 mm, 16 mm inner diameters. At a constant flow rate, the shear stress decreases with increasing scaffold diameter (Figure 24). Within each diameter group, additionally 3 different surface topographies were tested – no pattern flat surface, channels, and our novel channels and pits combination.



*Exact same experimental groups were also studied in static conditions as controls for each group

Figure 24. Experimental groups assessed in the TPS bioreactor study.

Although we were optimistic, due to the radius of the curvature we were unable to image through the scaffold and the surface of the scaffold for day 7 live/dead analysis. Out of all the experimental groups we attempted to image, we were able to pick up several images from the group 1 diameter scaffolds, the group with the smallest radius of curvature, shown in Figures 25 and 26. While the images obtained were too out of focus to perform morphology and orientation analysis, the majority of the cells visualized in the channels only group seemed to be aggregated to the area of the channels (Figure 25). Additionally in the channels and pits scaffolds (Figure 26), the cells appeared to be aggregated. The dotted white line overlays in Figures 25 and 26 indicate where the surface topography on the scaffold would be.



Figure 25: Group 1 diameter, channels pattern at day 7 time point. 2.5x

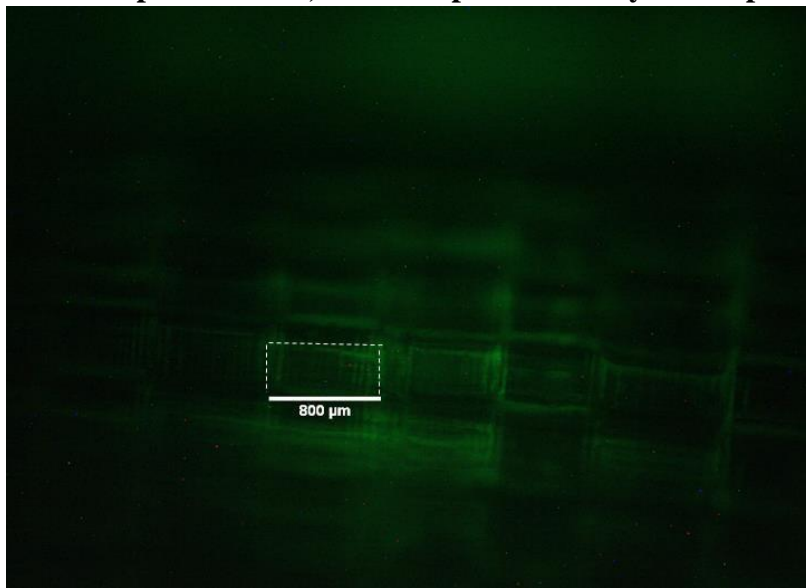


Figure 26: Group 1 diameter, channels and pits pattern at day 7 time point. 2.5x.

DNA analysis was performed via a PICO green assay. Samples included all TPS bioreactor samples as well as corresponding static scaffolds for each experimental

group. The analysis of DNA in the samples are shown in Figure 27. Statistical significance was determined using one way ANOVA with a 95% confidence interval.

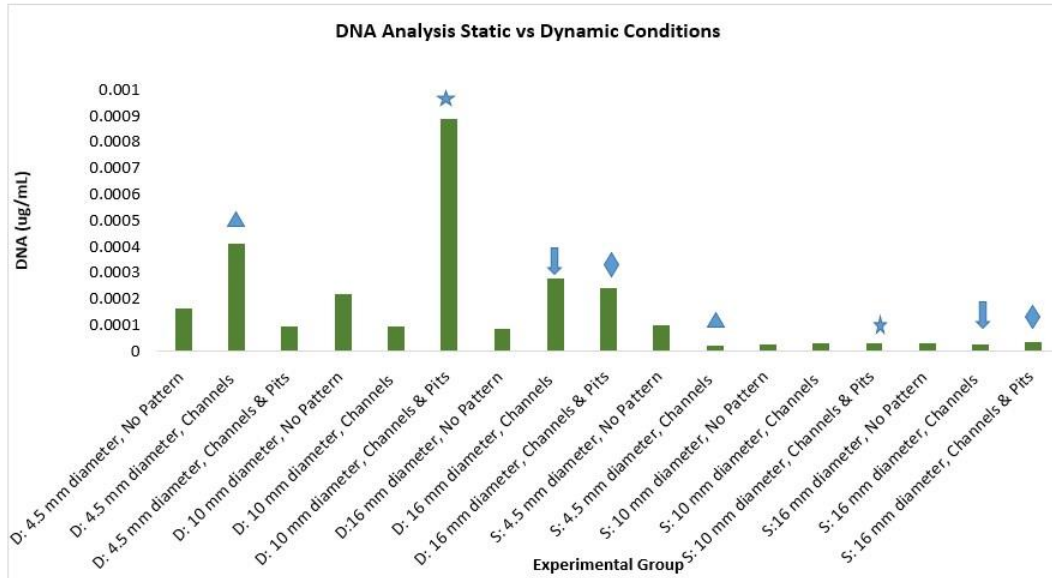


Figure 27: DNA PICO green assay results showing all groups. The blue symbols indicate the dynamic groups and static groups with statistically significant differences in DNA levels. D = dynamic study experimental group. S = static study experimental group.

Overall, all dynamic TPS bioreactor samples had higher levels of quantified DNA than the static controls. Additionally, when a scaffold in a specific experimental group from the TPS bioreactor was compared to its corresponding scaffold in the static control, there were statistically significant differences ($p < 0.05$) in the following experimental groups: Group 1 channels, Group 2 channels and pits, Group 3 channels, and Group 3 channels and pits. In all of these groups, the dynamic TPS bioreactor sample had a statistically significant larger amount of DNA than its static counterpart.

We can first focus on the effect of diameter on the DNA levels by keeping surface topography constant within the dynamic group. Although there were no statistical

significance among the no patterned dynamic scaffolds with varying diameters, when comparing channel topography in a dynamics groups we found that there was statistically higher DNA levels in the smallest diameter scaffolds than the 10 mm inner diameter scaffolds (Figure 28). Additionally, when comparing channels and pits combination surface topography among the different diameter scaffolds, the 10 mm scaffold had a statistically higher level of DNA than the smallest diameter scaffold, by a factor of almost 9 fold (Figure 29). This difference is indicated by the star in Figure 29. Additionally when comparing the 10 mm diameter group to the largest diameter group, the 10 mm group also had a statistically higher DNA level by a factor of 3 fold (Figure 29).

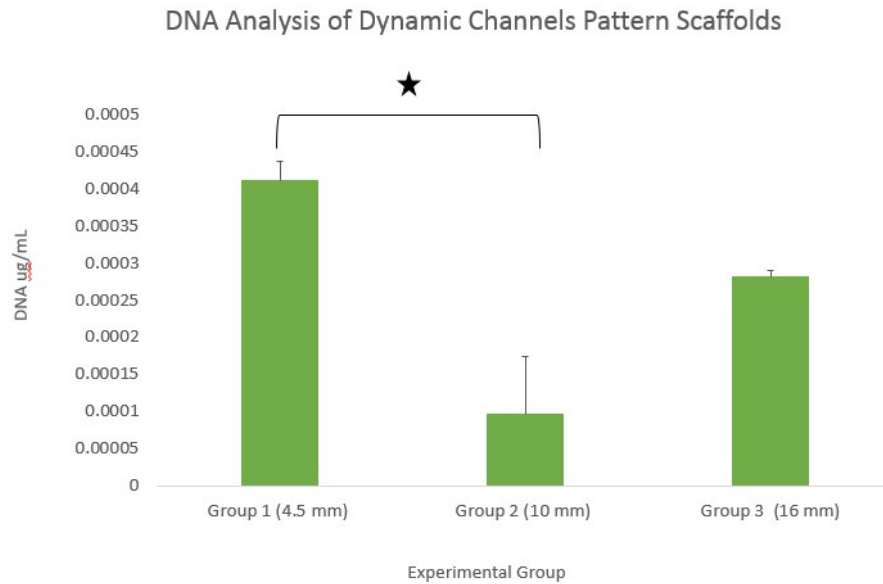


Figure 28. DNA analysis of dynamic channels pattern scaffold among varying diameter groups. Star represents statistically significant differences ($P < 0.05$).

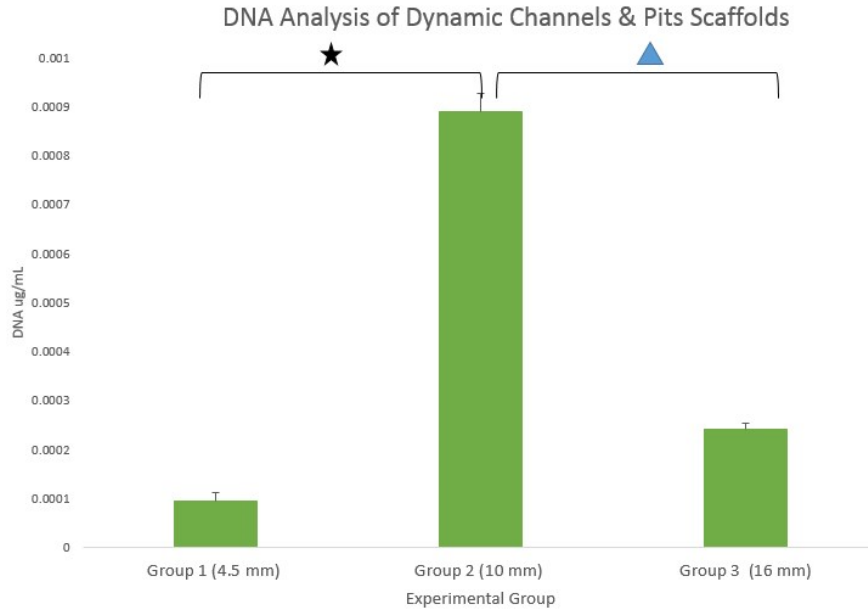


Figure 29. DNA analysis of dynamic channels pattern scaffold among varying diameter groups. Star and triangle represent statistically significant differences ($P < 0.05$).

Now keeping diameter constant we look at the effect of surface topography on DNA levels. In figure 30, we see that the channels topography had a statistically higher level of DNA than either the no pattern (as indicated by the star) and channels and pits combination pattern (indicated by the triangle) when looking at the results of the smallest diameter group of 4.5 mm (Figure 30). In the group with the 10 mm diameter, we see that the channels and pits topography had a statistically higher level of DNA than either the no pattern and channels combination group, as indicated by the star on the graph in Figure 31. In the group with the largest diameter, we see that both the channels topography as well as the channels and pits combination

topography had a statistically higher level of DNA than the no pattern group (Figure 32), as indicated by the star and triangle symbols respectively.

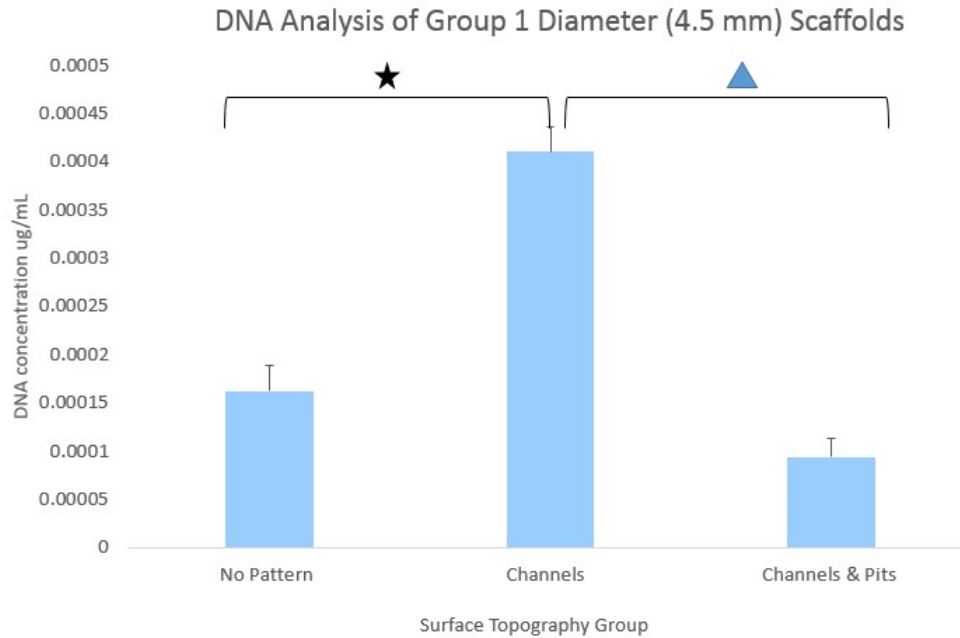


Figure 30. DNA analysis of group 1 diameter. Star and triangle indicate statistically different levels of DNA ($P < 0.05$).

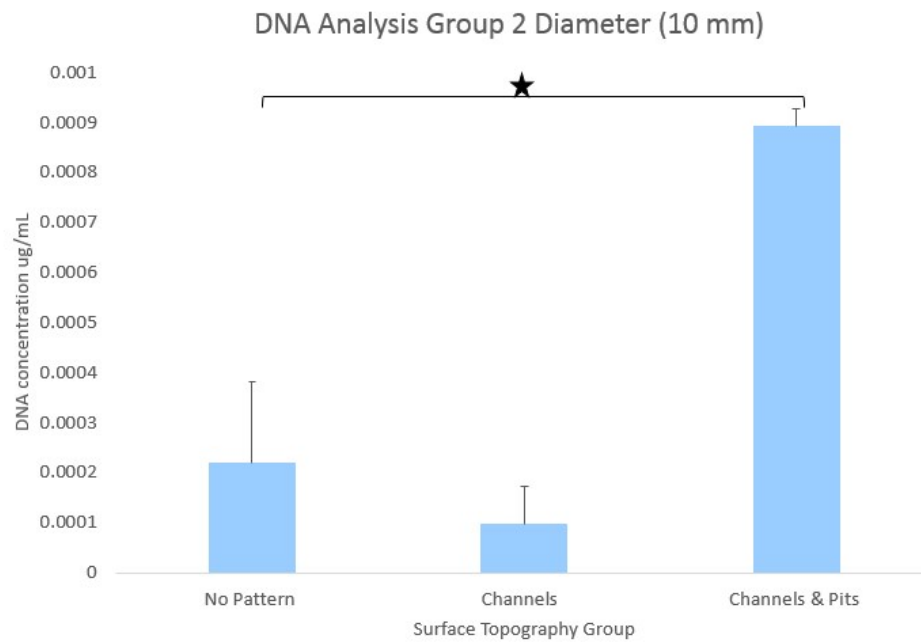


Figure 31. DNA analysis of group 2 diameter. Star indicate statistically different levels of DNA ($P < 0.05$).

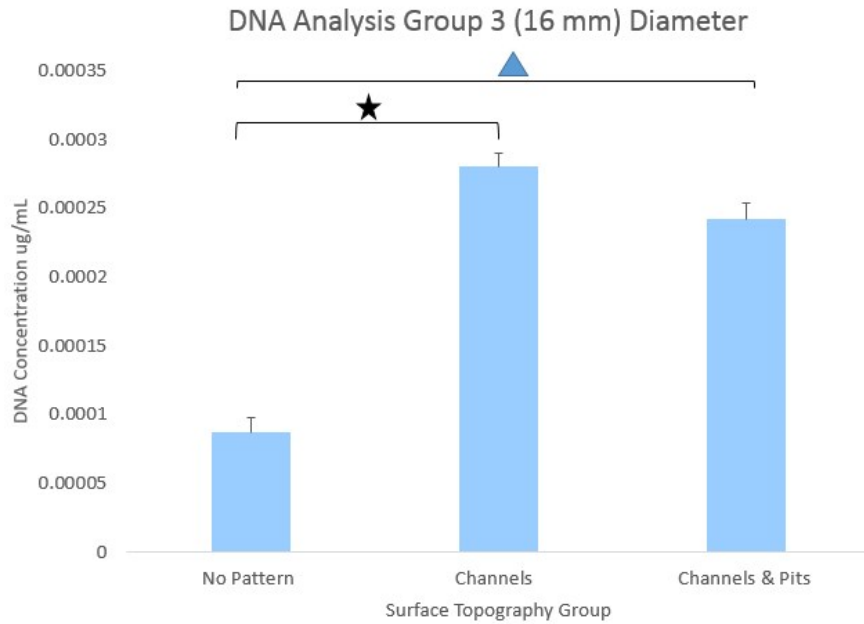


Figure 32. DNA analysis of group 3 diameter. Star and triangle indicate statistically different levels of DNA ($P < 0.05$).

Discussion

SolidWorks CFD Analysis

CFD analysis of the SolidWorks designs demonstrated varying flow profiles and velocities between different experimental groups. These velocities were on par with those shown to increase differentiation due to application of shear stress in previous TPS experiments. It was hypothesized that the variation in surface topography and diameter size would alter flow profiles and thus shear stress. The CFD analysis illustrates these variations, although the magnitude of differences between

groups is not very large. Future endeavors include doing additional simulations in a broader range of flow simulations higher than 20 mL/minute, which was the highest flow rate that was assessed in this study.

Static Conditions Endothelial Cell Analysis

HUVEC average attachment efficiency was also calculated on day 1 using live/dead imaging, which was found to be 23% +/- 6 (n=5). This is consistent with prior studies that have found fibronectin coating prior to seeding to enhance endothelial cell adhesion up to 20-30%. Proliferation of HUVECs was assessed on day 7. Compared to day 1 average cell count per cm² of 226 +/- 55 (n=5), day 7 average cell counts increased to 48493 +/- 1442 cells per cm² (n=3).

In the static conditions study, cells at the day 1 time point were consistently more rounded with an aspect ratio closer to 1 compared to cells at day 3 or day 7 under the same conditions, and had an aspect ratio much greater than 1. The greater aspect ratio with increased time progression, indicates that the HUVECs are becoming more elongated, which is consistent with prior studies.³⁵

Dynamic Growth Chamber Analysis

When comparing dynamic growth chamber samples at the Day 1 (24h) time point to static condition samples at the same time point, the dynamic study had a statistically significantly large average cell count per area than the static group (p = 0.046) (Figure 22). These results suggest that dynamic flow conditions may enhance proliferation, which would be consistent with other studies that have shown that shear

stress enhances proliferation.³⁶ There are several potential factors that may be playing a role in this increased proliferation- flow conditions allow for enhanced nutrient transport, waste removal, and the shear stress on the surface of the endothelial cells may activate mechanosensors that could induce downstream signaling and ultimately gene expression within the endothelial cells.³⁹ On the no pattern flat surface 2D scaffolds under dynamic flow, no orientation to the direction of flow was seen, which is consistent with prior research studies as well.^{35,37}

Future endeavors include producing a 2D patterned surface with a pattern small enough (on the order of a hundred microns or less) to fit the growth chamber model without leaks. This would allow us to analyze the effects of varying topography on the orientation of endothelial cells more clearly. Potential strategies at achieving this is by inverting the channel pattern so that the channels are printed into the surface, rather than as raised channels. Additionally, a longer term dynamic flow study beyond 24h would be beneficial in understanding the long term effects of flow and thus shear stress in combination with topographical patterns on endothelial monolayer formation.

TPS Bioreactor Analysis

Over early time points, the bioreactor culture was shown to support the proliferation of the cells. Bioreactor culture was shown that it may enhance proliferation, which is consistent with the increased DNA levels that were found in all dynamic culture samples compared to the corresponding static culture sample. There were minimal differences seen among different topographical pattern scaffolds compared to the no pattern flat surface scaffolds in the static control group. This is

consistent with prior studies that have shown that nanotopography has little effect on cell morphology and proliferation in static conditions.^{35,36} Of the images we were able to capture on day 7 during live/dead analysis, the majority of the cells visualized in the channels only group seemed to be aggregated to the area of the channels (Figure 25), which is consistent with previous studies. Additionally in the channels and pits scaffolds (Figure 26), the cells appeared to be aggregated in the pits, which has been previously been shown to reduce migration and enhance proliferation.^{34, 35}

In our initial study, we chose 20 ml/min as our flow rate to achieve a physiologically relevant surface shear stresses on the 3D printed scaffolds in the TPS bioreactor. Unfortunately we observed that the majority of cells that remained attached were in the pits (meant to provide cells a place to adhere and proliferate). We believe this may be due to the delamination of the fibronectin coating in other areas of the scaffold. Therefore, with these results, an additional studies are needed to investigate a bioreactor study using an order of magnitude lower flow rate (2 mL/min) to avoid this potential problem.

Overall, all dynamic TPS bioreactor samples had higher levels of quantified DNA than the static controls. Additionally, when a scaffold in a specific experimental group from the TPS bioreactor was compared to its corresponding scaffold in the static control, the TPS bioreactor scaffold had a higher quantity of DNA present, which indicates more cells present, and thus suggests enhanced proliferation. Our novel combination of channels and pits combination pattern showed the highest DNA quantity out of all the samples when combined with the group 2 diameter size (Figure

27). In all diameter groups in the dynamic study, the topographical pattern scaffolds, either the channels, channels and pits combination, or both, had higher DNA levels than the dynamic scaffold with no pattern in the same diameter group; In the group 1 diameter group, D2 was statistically greater than D1, in group 2 D6 was statistically greater than D4, and in group 3 both D8 and D9 were statistically greater than D7 (Figure 27). These statistically higher DNA readings suggest that specific architectural combinations, such as diameter and surface topography in this study may have the ability to significantly enhance cell proliferation, and potentially monolayer formation as well. Specifically, novel pattern combinations, rather than testing single surface topographies alone may potentially provide more impactful contact guidance cues and signals to cells to dramatically increase cell proliferation and monolayer formation.

Conclusion

With over 185,000 limb amputations in the United States alone,² and approximately 15 million bone fractures worldwide every year,¹ there is a large clinical need for bone tissue engineering alternatives. At present, approximately 1 million grafting procedures are performed each year. While current grafting procedures and surgical techniques help to heal bone defects, they also result in many undesirable effects including infection, graft rejection, donor site morbidity, and extended healing times. Recently, great strides have been made in the field of bone tissue engineering research, however, a major limitation of such 3D constructs is the

lack of inherent vasculature, which thus limits nutrient transfer. In order to increase the feasibility of cell based tissue engineering strategies, this limitation must be overcome.

The most common component of engineered vascular constructs is the presence of endothelial cells. Many techniques are currently being investigated for the development of vascularized networks with the ultimate goal of developing inherent vasculature within engineered bone tissue grafts. Some of these methods include *in vivo* and *in vitro* prevascularization of grafts. Due to several disadvantages of the former methods mentioned, more recent research has focused on 3D printing of vascular scaffolds. Additionally, a common method for overcoming this nutrient transfer limitation is the use of bioreactor systems. An important benefit of bioreactor systems is their ability to create an *in vitro* environment that mimics the *in vivo* environment of the human body more closely.

This research provides a promising and novel approach to the vascularization of bone tissue engineered constructs. Here, DLP stereolithographic printing is combined with *in silico* modeling and *in vitro* testing to design and validate biomimetic vascular architecture for use in TPS bioreactors. Under this system, cells can experience dynamic flow and accompanying shear stress to preferentially enhance endothelial cell layer formation.

The first goal of this study was to determine what flow rate was to be used for producing a physiologically relevant shear stress in our TPS bioreactor study. This was accomplished by running computational fluid dynamic simulations at six different flow rates on SolidWorks using the Flow Simulation Package. From the results of

these simulations we determined that a flow rate of 20 mL/min would provide the shear stress that was closest to physiologically relevant levels than any of the other flow rates.

Finally, *in silico* modeling results from SolidWorks were examined *in vitro* by running a 7 day bioreactor experiment with human umbilical vein endothelial cells in 9 different experimental groups, as well as corresponding static controls for each group. In short, Day 7 DNA quantification results were statistically significant when comparing four of the bioreactor experimental groups to their corresponding static groups. Overall the DNA levels were higher in all dynamic groups compared to their static counterpart. Additionally in every diameter group in the dynamic portion of the study, one or both of the topographical scaffolds always had a statistically higher level of DNA than the no pattern scaffold in the same diameter group. Of note, the Group 2 diameter with channels and pore topographical pattern had a statistically significantly higher level of DNA, and thus cell proliferation than any other experimental group, suggesting the potential ability of novel topographical pattern and diameter combinations to significantly enhance cell proliferation and eventually endothelial cell monolayer formation.

The vascular network designed and printed here shows promise not only for use in TPS bioreactors, but also many other dynamic culture strategies. By combining this architecture with a biodegradable network material and a lining of endothelial cells, it may be possible to create a vascular network that provides for the extended growth and viability of bone grafts, especially larger scale, clinically relevant sized

grafts. Further, the incorporation of large-diameter inlet and outlet channels allows for the potential direct anastomosis of these constructs to existing host vasculature.

Ideally, this inherent graft vasculature would sustain cell life until the network can be fully integrated with the body via spontaneous host vascular ingrowth.

Through the studies we presented here we have presented a proof of concept of fibronectin as a successful substrate for HUVECs on EShell polymer surfaces.

Additionally, we have shown proof of concept of successfully printed a novel combination of channels and pits topography and illustrated that these topographical combinations do alter shear stress, as visualized on the SolidWorks flow simulations.

Furthermore, we demonstrated that changes in shear stress due to this varying architecture has the potential to influence cell behavior and proliferation. From the studies presented here, we were able to investigate the short term effects of shear stress and architecture on endothelial cell behavior; with this information, it would now be useful to look at longer term effects of these factors on endothelial cell behavior.

In summary, a thorough combination of computer-aided design, *in silico* modeling, and *in vitro* experiments resulted in the development of a 3D printed with novel architecture has been utilized to illustrate the potential of surface topography and shear stress to enhance endothelial cell monolayer formation. While no complete monolayer formation was visualized, these initial results are encouraging, but additional computer aided design simulations and *in vitro* bioreactor studies need to be

performed to determine and solidify which architectural combination results in an endothelial cell monolayer formation.

Chapter 4: Appendix A: Raw Data & Calculations

Static Condition Studies

In all of the cell count data below, cell counts from images were converted to cell counts on the prints using the following conversions and calculations:

Image sizes on Image J:

2.5x mag: 319 pixels = 1000 microns

10x mag: 1069 pixels = 1000 microns

20x mag: 1499 pixels = 700 microns

40x mag = 1486 pixels = 350 microns

Multiply cell count from images by ratio of: area of print / area of image

Day 1 (24h)

10x images	Image 1	Image 2	Image 3	Image 4	Image 5	Average Cell Count/ cm ²
Sample 1	371	480	393	401	436	249
Sample 2	551	338	313	319	332	221
Sample 3	319	316	700	298	444	248

Sample 5	37	1	47	9	23	124
Sample 6	6	8	7	1	2	286
Average						226 +/- 55

Table 4: No pattern/flat surface cell counts and calculations at day 1 time point.

Sample	Seeding Density Cells/ cm ²	Number of cells seeded	Total Cells counted print	Attachment Efficiency (%)
1	5000	234000	59953	25
2	5000	234000	53384	23
3	5000	234000	59838	26
4	5000	25000	3001	12
5	5000	25000	6914	28
Average				23 +/- 6

Table 5: No pattern/flat surface attachment efficiency data at Day 1 time point.

Side 1	Side 2	Aspect Ratio
138	57	2.421053
133	85	1.564706
143	35	4.085714
133	25	5.32
47	25	1.88
60	60	1
361	94	3.840426
96	48	2
150	82	1.829268
177	68	2.602941
244	76	3.210526

Side 1	Side 2	Aspect Ratio
196	47	4.170213
111	54	2.055556
106	44	2.409091
88	17	5.176471
190	72	2.638889
95	20	4.75
160	58	2.758621
215	86	2.5
109	34	3.205882

Table 6: Aspect ratio data and calculations at day 1 time point.

Day 3: Morphology and Proliferation

10x images	Image 1	Image 2	Image 3	Image 4	Image 5	Total Cells Counted in print
Sample 1	17	36	27	17	28	36013
Sample 2	18	14	10	17	14	1873
Sample 3	17	10	8	18	13	1693
Sample 4	3	7	20	4	22	1436
Average						10254

Table 7: No pattern flat surface cell count data at day 3 time point.

Side 1	Side 2	Aspect Ratio
213	73	2.917808
278	24	11.58333
152	46	3.304348
271	20	13.55
270	48	5.625
460	48	9.583333
328	45	7.288889
353	29	12.17241
429	27	15.88889
85	42	2.02381
443	40	11.075
160	77	2.077922
239	39	6.128205

Side 1	Side 2	Aspect Ratio
280	49	5.714286
212	43	4.930233
203	21	9.666667
350	27	12.96296
159	44	3.613636
308	66	4.666667
247	42	5.880952
169	17	9.941176
181	14	12.92857
267	54	4.944444
140	46	3.043478
288	36	8
338	56	6.035714
354	26	13.61538
409	49	8.346939

Table 8: Aspect ratio data at day 3 time point.

Day 7: Proliferation

10x images	Image 1 Cell Count	Image 2 Cell Count	Image 3 Cell Count	Image 4 Cell Count	Image 5 Cell Count	Average # cells per image	Total Cells on print	Average Cell Count/cm ²
Sample 5	298	0	0	486	368	231	2417829	68572
Sample 7	0	0	308	170	220	140	1464969	41548
Sample 8	650	450	350	250	500	440	1255210	35358
Average								48493 +/- 1442

Table 9: No pattern/flat surface cell counts and calculations at day 7 time point.

Dynamic Growth Chamber Studies

Day 1 (10x)	Image 1 Cell Count	Image 2 Cell Count	Image 3 Cell Count	Image 4 Cell Count	Image 5 Cell Count	Average # cells per image	Total Cells Counted in images	Average Cell print/ cm²
Sample 1	14	12	12	13	13	13	64	12765
Sample 2	1	2	1	1	1	1	6	1197
Sample 3	38	35	35	35	31	35	174	10287
Sample 4	37	35	36	35	30	35	173	10228
Average								8620 +/- 4406

Table 10: No pattern/flat surface total cells on 2D prints at day 1 time point.

Sample	Seeding Density Cells/ cm ²	Number of cells seeded	Total Cells counted print	Attachment Efficiency (%)
1	5000	177000	16134	9
2	5000	177000	36013	15
3	5000	25000	3001	12
4	5000	25000	6914	28
Average				16 +/- 7

Table 11: No pattern flat surface, attachment efficiency at day 1 time point.

Side 1	Side 2	AR
143	72	1.986111
38	33	1.151515
32	31	1.032258
10	10	1

Table 12: No pattern/flat surface, aspect ratio at day 1 time point.

Bioreactor Study

Pre-TPS bioreactor study setup calculations

Group	Outer D (mm)	Inner D (mm)	Thickness (mm)
1	11.1252	6.35	2.3876
2	19.05	12.7	3.175
3	25.4	19.05	3.175

Table 13: Tubing sizes available for TPS bioreactor study.

Group	Outer D (mm)	Inner D (mm)	Thickness (mm)	Length (mm)
1	5.5	4.5	1	62
2	11	10	1	25.5
3	17	16	1	16.5

Table 14: Diameters of 3D scaffolds based on tubing sizes.

Tubing type	# of tubing segments needed	# of lines	Total # of segments needed	Length of each segment (2 scaffolds + connectors at each end) (mm)	Length of each segment (in)
1/4"	2	2	4	151	6
1/2"	2	2	4	102	4.1
3/4"	2	2	4	90	3.5
Connector type	# needed per line	# of lines	Total # needed		
1/8→1/4	2	2	4		
1/4→1/2	2	2	4		
1/2→3/4	2	2	4		
3/4→3/4	1	2	2		

Table 15: Tubing length quantities needed for setup of TPS bioreactor.

Tubing type	Length each segment (in)	Inner SA (in ²)	# of segments	Total SA of each (in ²)
1/4"	6	4.7	4	18.8
1/2"	4.1	6.5	4	25.8
3/4"	3.5	8.3	4	32.3
Total SA				77 in²
				497 cm²

Table 16: Total inner surface area of scaffolds in bioreactor setup.

Based on SA to media ratio of T-75 (75 cm²: 12 mL media):

Total amount of media needed for tubing: 80 mL

Amount of media needed for each separate line: 40 mL

Amount of media to be added to each media reservoir flask: 100 mL

Tubing type	Length each segment (in)	Inner volume (in ³)	# of segments	Total V of each (in ³)
1/4"	6	0.30	4	1.20
1/2"	4.1	0.81	4	3.22
3/4"	3.5	1.55	4	6.20
Total Volume				10.62 in³
				174 cm³ = 174 mL

Table 17: Total volume of tubing in TPS bioreactor.

Tubing type	Length each segment (in)	Inner SA (in ²)	Inner SA (cm ²)	# of segments	Total SA of each (in ²)
1/4"	6	4.7	30.4	4	121.4
1/2"	4.1	6.5	42.0	4	168.0
3/4"	3.5	8.3	53.6	4	214.4
Total SA					78 in²
					504 cm²

Table 18: Total HUVEC requirement needed based on total inner surface area of scaffolds in bioreactor setup.

Cell seeding density: 5,000 cells/ cm²

Total amount of cells required: 504* 5,000 = **million cells**

DNA Analysis: Data and Calculations

High	
0.000875	-0.00497
5.2E-06	0.002683
0.999894	0.005186
28377.19	3
0.763156	8.07E-05
#N/A	#N/A

Table 19: PICO green assay standard curves.

	1	2	3	4	5	6	7	8	9	10	11	
A	H1	L1	D1	D1	D1	D7	D7	D7	S6	S6	S6	
B	H2	L2	D2	D2	D2	D8	D8	D8	S6	S6	S6	
C	H3	L3	D3	D3	D3	D9	D9	D9	S7	S7	S7	
D	H4	L4	D4	D4	D4	S1	S1	S1	S8	S8	S8	
E	H5	L5	D4	D4	D4	S2	S2	S2	S9	S9	S9	
F			D5	D5	D5	S4	S4	S4				
G			D5	D5	D5	S5	S5	S5				
H			D6	D6	D6	S5	S5	S5				

	1	2	3	4	5	6	7	8	9	10	11	12
A	H1	L1	D1	D1	D1	D7	D7	D7	S6	S6	S6	
B	H2	L2	D2	D2	D2	D8	D8	D8	S6	S6	S6	
C	H3	L3	D3	D3	D3	D9	D9	D9	S7	S7	S7	
D	H4	L4	D4	D4	D4	S1	S1	S1	S8	S8	S8	
E	H5	L5	D4	D4	D4	S2	S2	S2	S9	S9	S9	
F			D5	D5	D5	S4	S4	S4				
G			D5	D5	D5	S5	S5	S5				
H			D6	D6	D6	S5	S5	S5				

Table 20: PICO green plate setup. H= high standard curve, L = low standard curve. D = dynamic conditions sample (TPS bioreactor). S = static conditions sample. Sample 1 = group 1, no pattern. Sample 2 = group 1, channels. Sample 3 = group 1, channels and pits. Sample 4 = group 2, no pattern. Sample 5 = group 2, channels. Sample 6 = group 2, channels and pits. Sample 7 = group 3, no pattern. Sample 8 = group 3, channels. Sample 9 = group 3, channels and pits.

Table 20: PICO green plate setup. H= high standard curve, L = low standard curve. D = dynamic conditions sample (TPS bioreactor). S = static conditions sample. Sample 1 = group 1, no pattern. Sample 2 = group 1, channels. Sample 3 = group 1, channels and pits. Sample 4 = group 2, no pattern. Sample 5 = group 2, channels. Sample 6 = group 2, channels and pits. Sample 7 = group 3, no pattern. Sample 8 = group 3, channels. Sample 9 = group 3, channels and pits.

	1	2	3	4	5	6	7	8	9	10	11
A	1	0.0025	0.000127	0.000174	0.000187	8.34E-05	7.55E-05	0.000101	3.41E-05	3.39E-05	4.65E-05
B	0.1	0.00025	0.000393	0.000392	0.000447	0.000267	0.000288	0.000287	1.86E-05	5.66E-05	3.78E-06
C	0.01	0.000025	0.000117	9.51E-05	7.11E-05	0.000237	0.000231	0.000259	3.53E-05	3.5E-05	2.34E-05
D	0.001	2.5E-06	7.2E-05	4.71E-05	5.16E-05	0.000104	9.91E-05	9.97E-05	2.89E-05	2.53E-05	1.82E-05
E	0	0	0.000401	0.000356	0.000387	2.13E-05	2.86E-05	1.62E-05	3.05E-05	3.85E-05	3.54E-05
F			1.84E-05	8.25E-06	3.05E-05	2.98E-05	2.54E-05	2.02E-05			
G			0.000176	0.000152	0.000189	3.24E-05	2.02E-05	4.23E-05			
H			0.000852	0.00088	0.000941	2.45E-05	2.18E-05	2.16E-05			

Table 21: PICO green plate results raw data corresponding to plate setup above.

	1	2	3	4	5	6	7	8	9	10	11
A	1	0.0025	0.000127	0.000174	0.000187	8.34E-05	7.55E-05	0.000101	3.41E-05	3.39E-05	4.65E-05
B	0.1	0.00025	0.000393	0.000392	0.000447	0.000267	0.000288	0.000287	1.86E-05	5.66E-05	3.78E-06
C	0.01	0.000025	0.000117	9.51E-05	7.11E-05	0.000237	0.000231	0.000259	3.53E-05	3.5E-05	2.34E-05
D	0.001	2.5E-06	7.2E-05	4.71E-05	5.16E-05	0.000104	9.91E-05	9.97E-05	2.89E-05	2.53E-05	1.82E-05
E	0	0	0.000401	0.000356	0.000387	2.13E-05	2.86E-05	1.62E-05	3.05E-05	3.85E-05	3.54E-05
F			1.84E-05	8.25E-06	3.05E-05	2.98E-05	2.54E-05	2.02E-05			
G			0.000176	0.000152	0.000189	3.24E-05	2.02E-05	4.23E-05			
H			0.000852	0.00088	0.000941	2.45E-05	2.18E-05	2.16E-05			

Table 22: PICO green plate results in micrograms/mL and corresponding to plate setup above.

Label	Ones Different Than ($p < 0.05$)
D1	D6, D4, D2
D2	D6, D9, D1, S1, D5, D3, D7, S9, S6, S7, S5, S4, S8, S2
D3	D6, D2, D8, D9
D4	D6
D5	D6, D2
D6	All
D7	D6, D2, D8, D9.
D8	D6, S1, D3, D7, S9, S6, S7, S5, S4, S8, S2
D9	D6, D2, S1, D3, D7, S9, S6, S7, S5, S4, S8, S2
S1	D6, D2, D8, D9, S9, S6, S7, S5, S4, S8, S2
S2	D6, D2, D8, D9, S1
S4	D6, D2, D8, D9, S1
S5	D6, D2, D8, D9, S1

Label	Ones Different Than ($p < 0.05$)
S6	D6,D2,D8,D9,S1
S7	D6,D2,D8,D9,S1
S8	D6,D2,D8,D9,S1
S9	D6,D2,D8,D9,S1

Table 23: PICO green results. a. Average and standard deviation values for each sample. b. Significant differences between samples.

Chapter 5: Appendix B: SolidWorks CFD Results

Shear Stress Surface Plot Contours

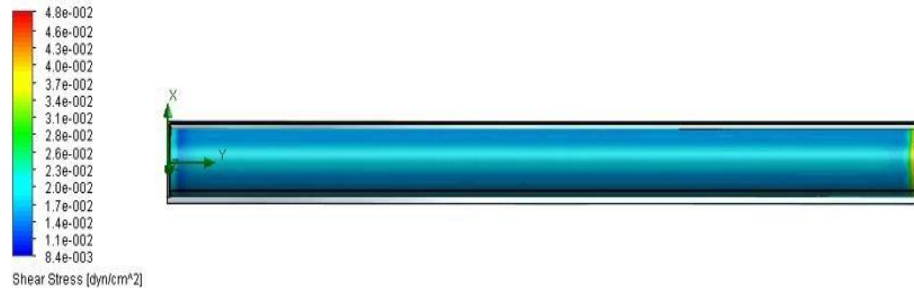


Figure 33: Group 1 no pattern at 0.5 mL/minute flow rate.

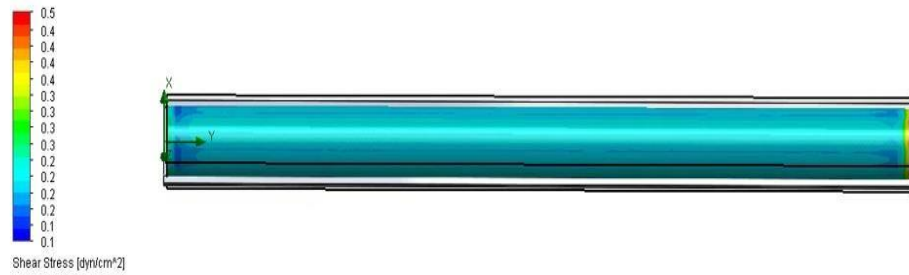


Figure 34: Group 1 no pattern at 1 mL/minute flow rate.

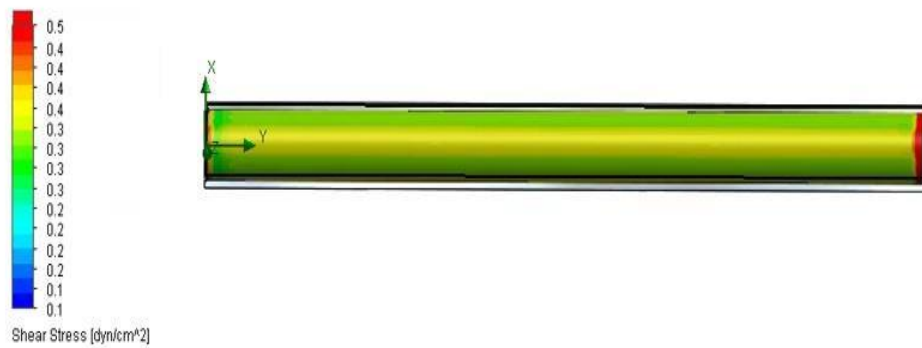


Figure 35: Group 1 no pattern at 2 mL/minute flow rate.

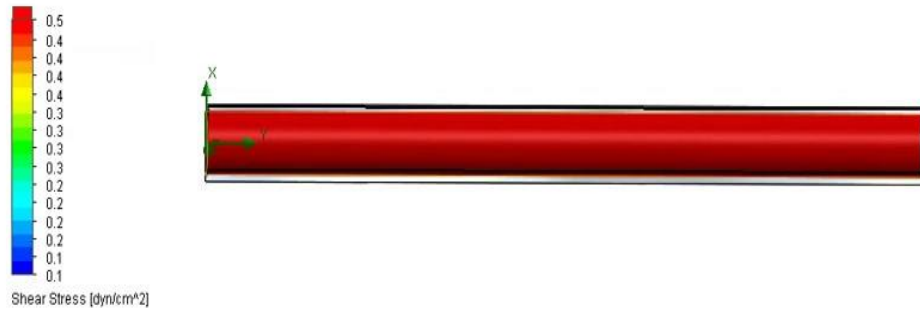


Figure 36: Group 1 no pattern at 5 mL/minute flow rate.



Figure 37: Group 1 no pattern at 10 mL/minute flow rate.

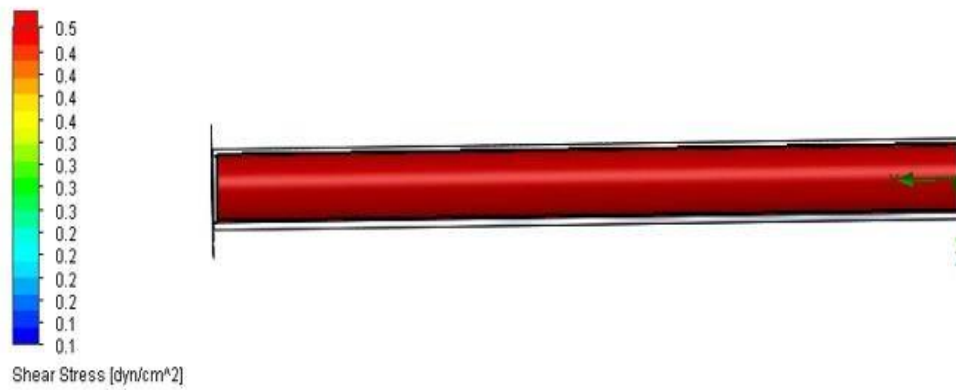


Figure 38: Group 1 no pattern at 20 mL/minute flow rate.

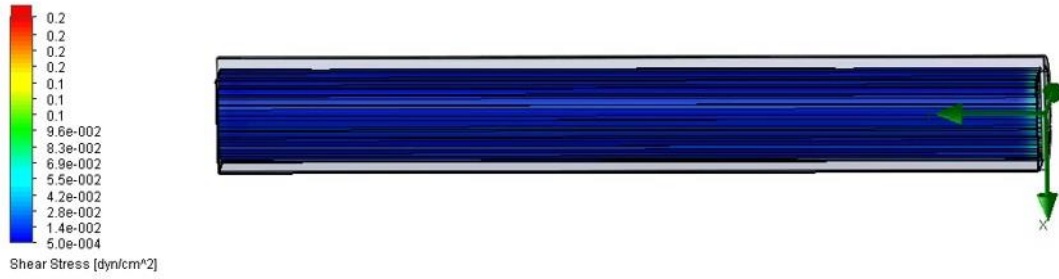


Figure 39: Group 1 with channels at 0.5 mL/minute flow rate.



Figure 40: Group 1 with channels at 1 mL/minute flow rate.



Figure 41: Group 1 with channels at 2 mL/minute flow rate.



Figure 42: Group 1 with channels at 5 mL/minute flow rate.



Figure 43: Group 1 with channels at 10 mL/minute flow rate.



Figure 44: Group 1 with channels at 20 mL/minute flow rate.

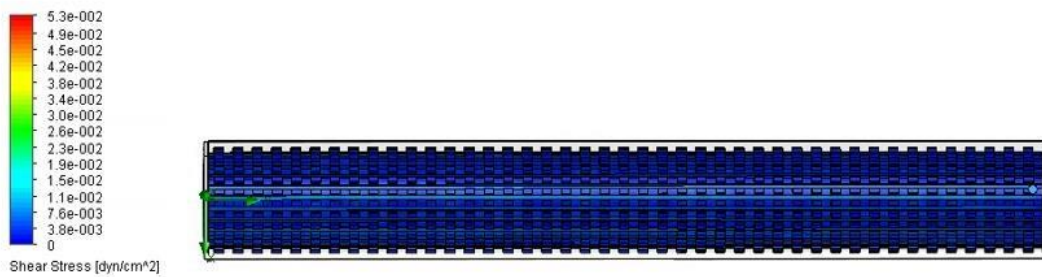


Figure 45: Group 1 with channels and pits at 0.5 mL/minute flow rate.

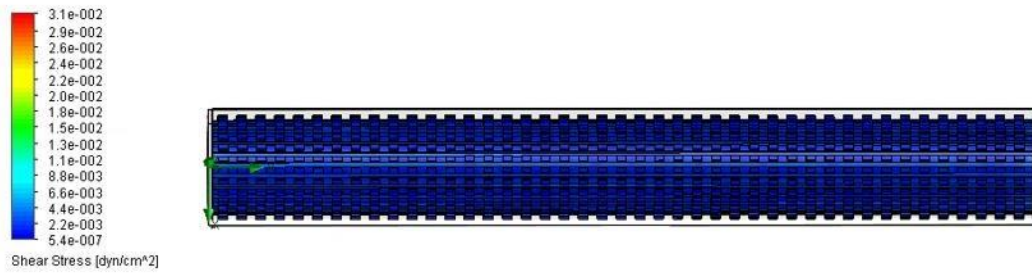


Figure 46: Group 1 with channels and pits at 1 mL/minute flow rate.

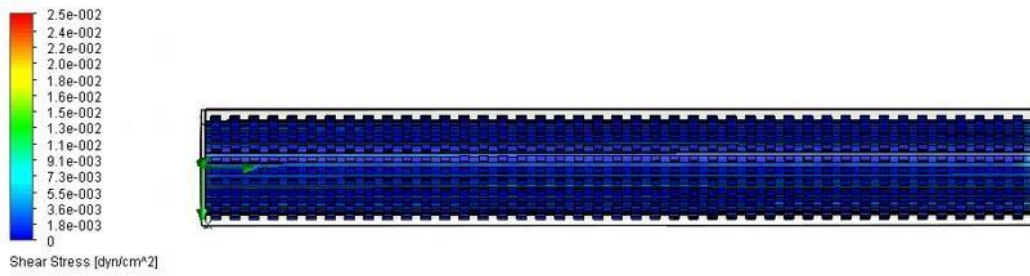


Figure 47: Group 1 with channels and pits at 2 mL/minute flow rate.

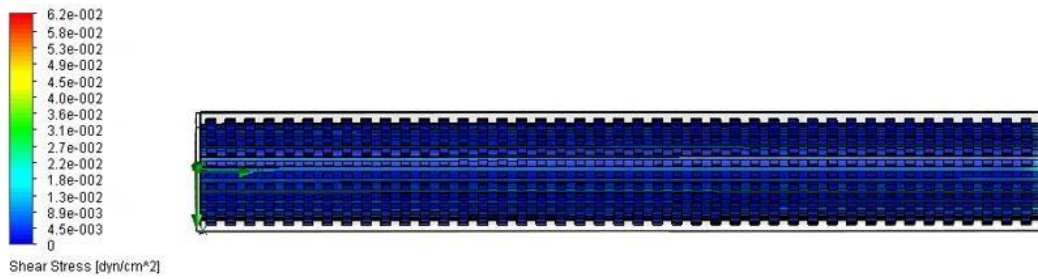


Figure 48: Group 1 with channels and pits at 5 mL/minute flow rate.

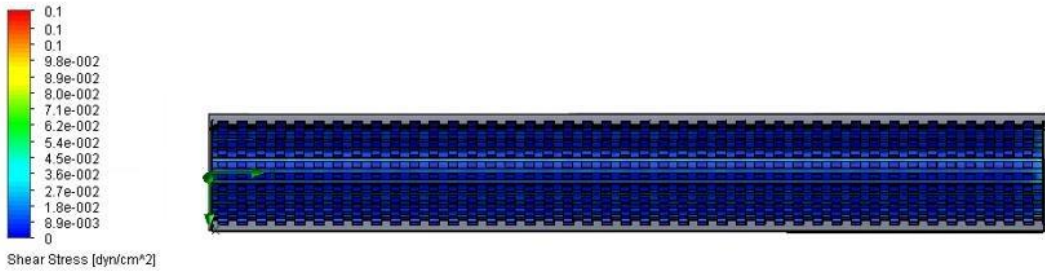


Figure 49: Group 1 with channels and pits at 10 mL/minute flow rate.

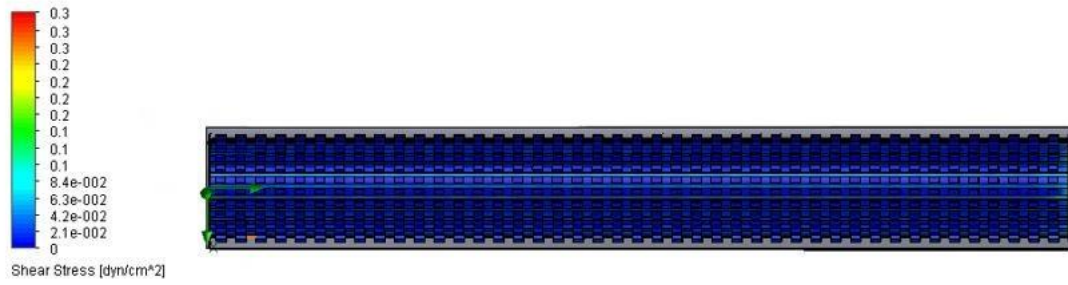


Figure 50: Group 1 with channels and pits at 20 mL/minute flow rate.



Figure 51: Group 2 no pattern at 0.5 mL/minute flow rate.

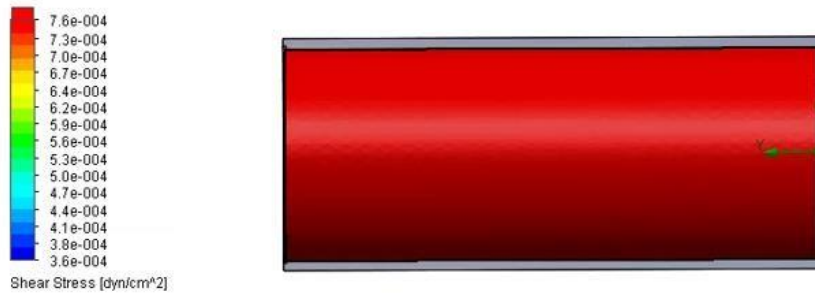


Figure 52: Group 2 no pattern at 1 mL/minute flow rate.

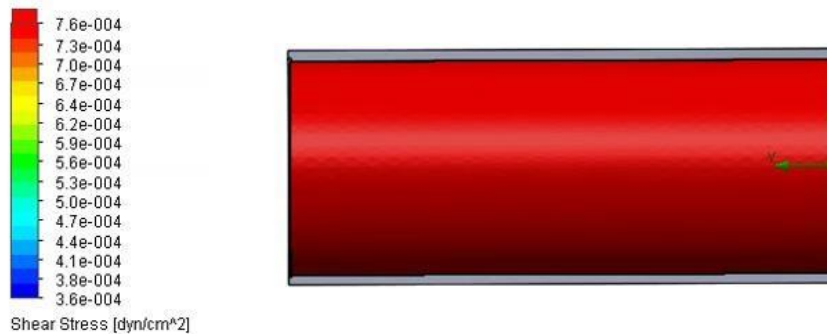


Figure 53: Group 2 no pattern at 2 mL/minute flow rate.

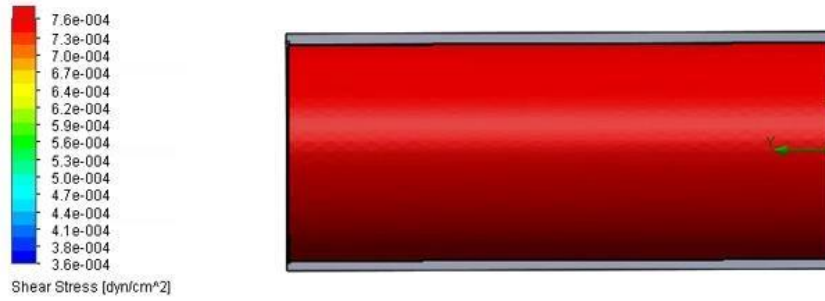


Figure 54: Group 2 no pattern at 5 mL/minute flow rate.

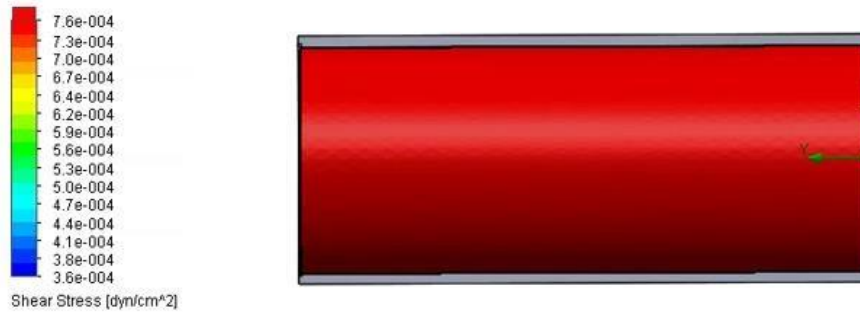


Figure 55: Group 2 no pattern at 10 mL/minute flow rate.

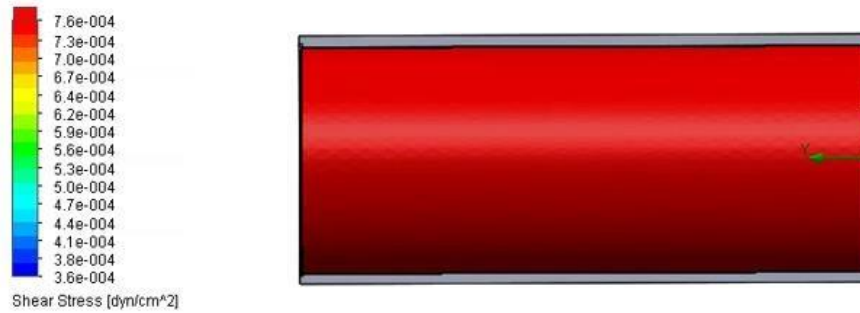


Figure 56: Group 2 no pattern at 20 mL/minute flow rate.



Figure 57: Group 2 with channels at 0.5 mL/minute flow rate.



Figure 58: Group 2 with channels at 1 mL/minute flow rate.



Figure 59: Group 2 with channels at 2 mL/minute flow rate.



Figure 60: Group 2 with channels at 5 mL/minute flow rate.



Figure 61: Group 2 with channels at 10 mL/minute flow rate.

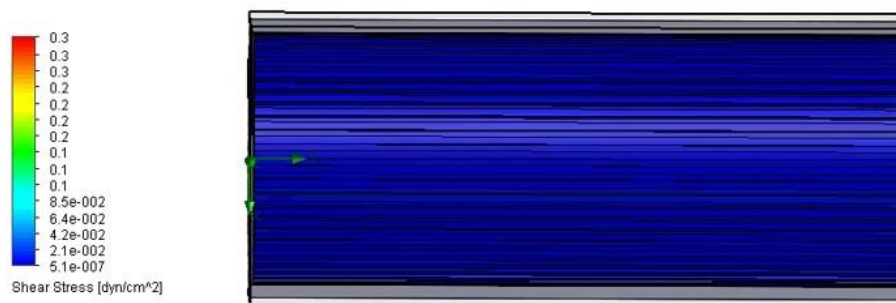


Figure 62: Group 2 with channels at 20 mL/minute flow rate.

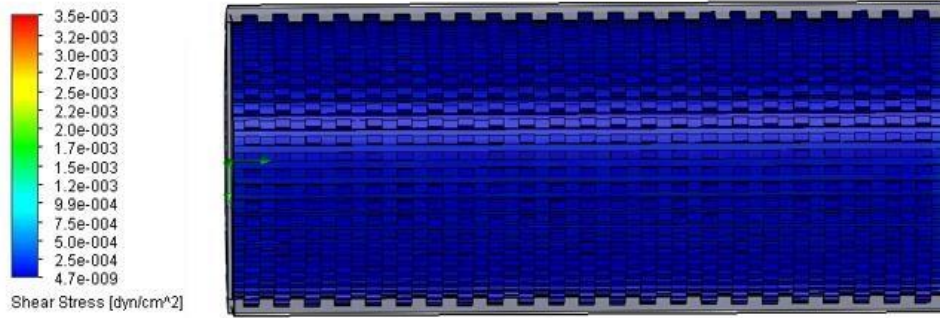


Figure 63: Group 2 with channels and pits at 0.5 mL/minute flow rate.

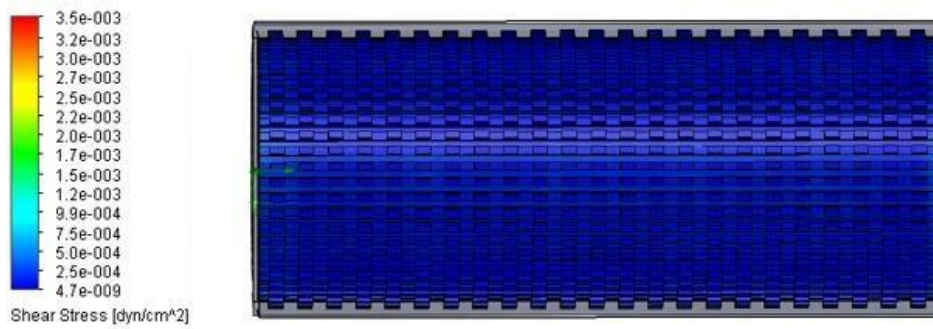


Figure 64: Group 2 with channels and pits at 1 mL/minute flow rate.

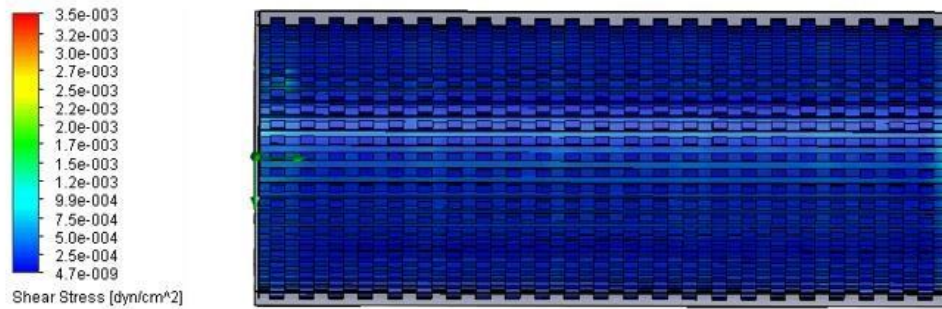


Figure 65: Group 2 with channels and pits at 2 mL/minute flow rate.

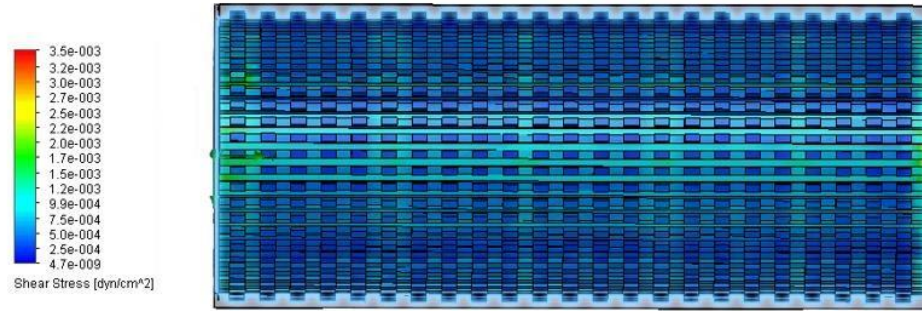


Figure 66: Group 2 with channels and pits at 5 mL/minute flow rate.

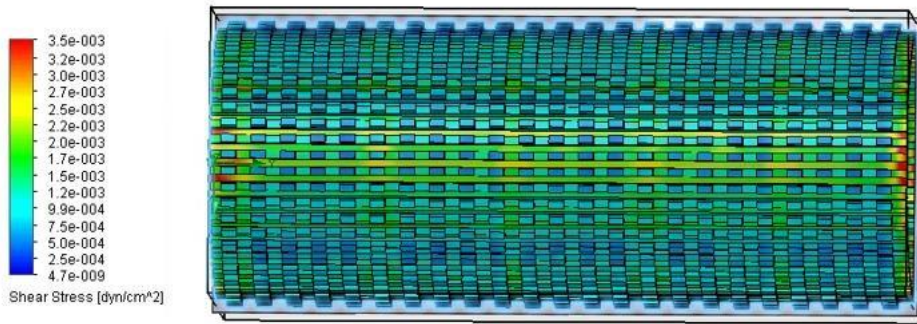


Figure 67: Group 2 with channels and pits at 10 mL/minute flow rate.

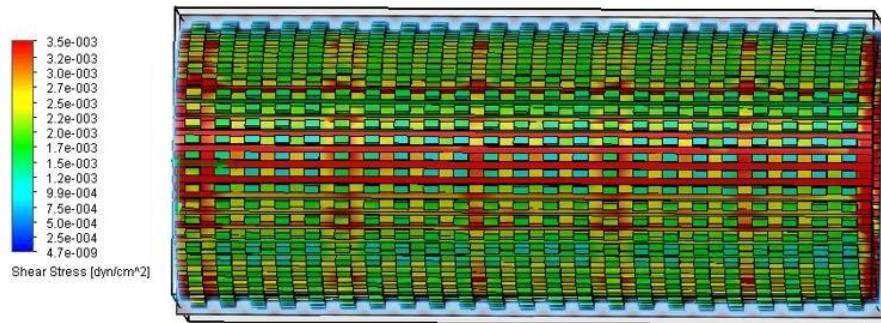


Figure 68: Group 2 with channels and pits at 20 mL/minute flow rate.

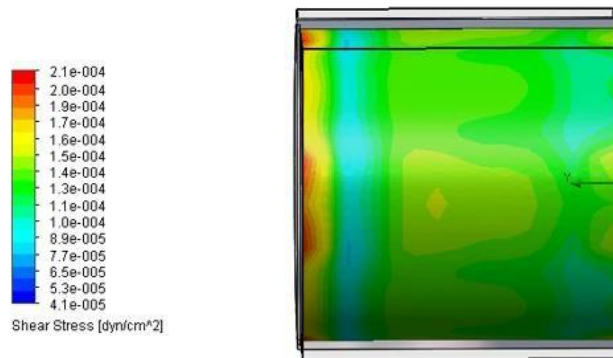


Figure 69: Group 3 no pattern at 0.5 mL/minute flow rate.

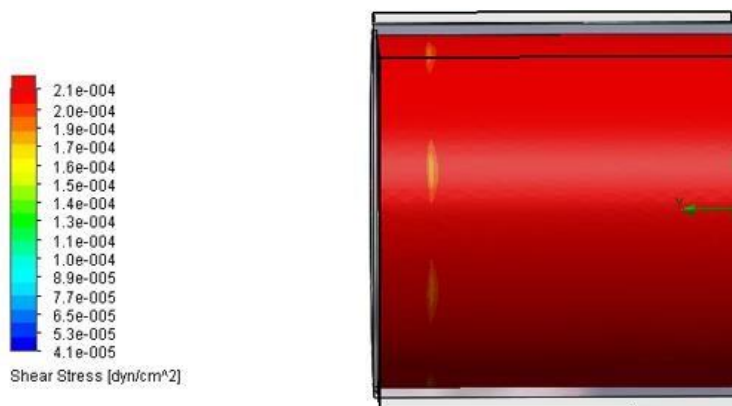


Figure 70: Group 3 no pattern at 1 mL/minute flow rate.

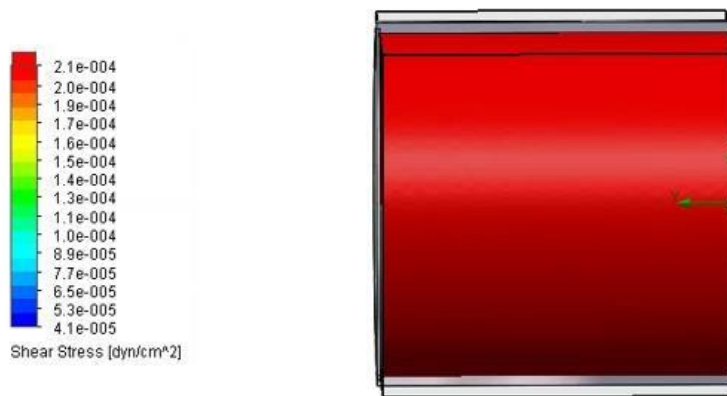


Figure 71: Group 3 no pattern at 2 mL/minute flow rate.

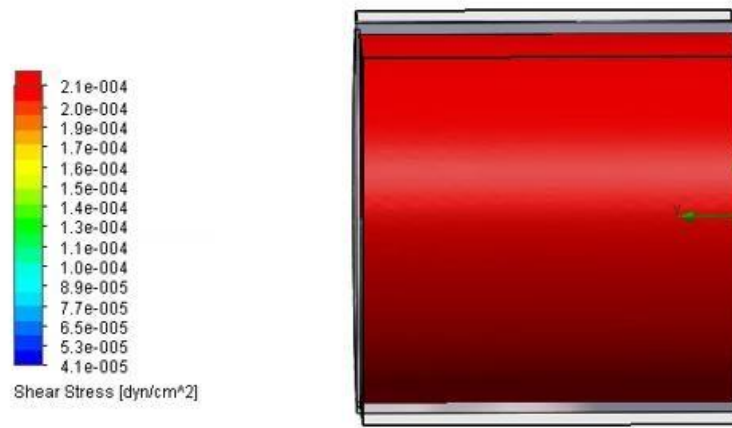


Figure 72: Group 3 no pattern at 5 mL/minute flow rate.

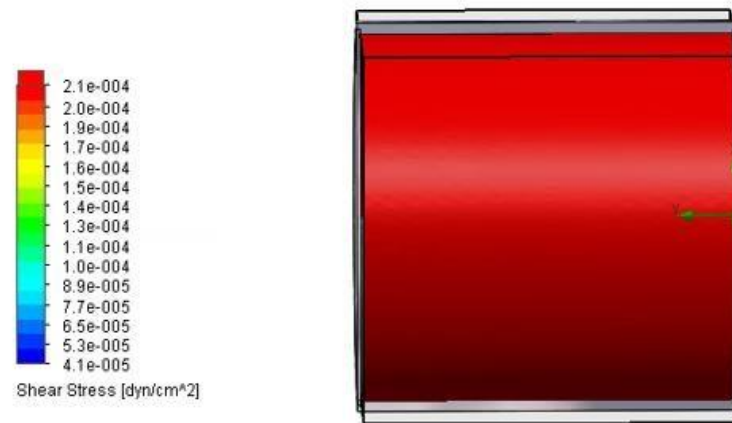


Figure 73: Group 3 no pattern at 10 mL/minute flow rate.

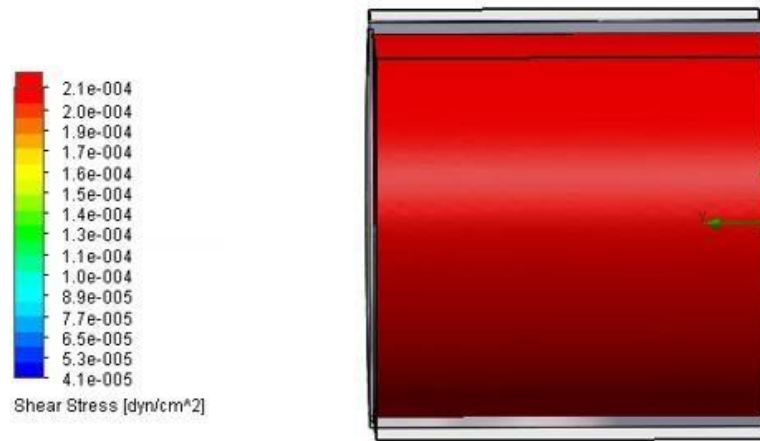


Figure 74: Group 3 no pattern at 20 mL/minute flow rate.

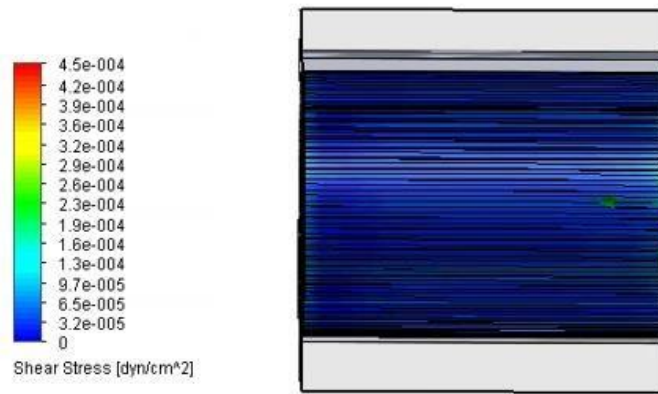


Figure 75: Group 3 with channels at 0.5 mL/minute flow rate.

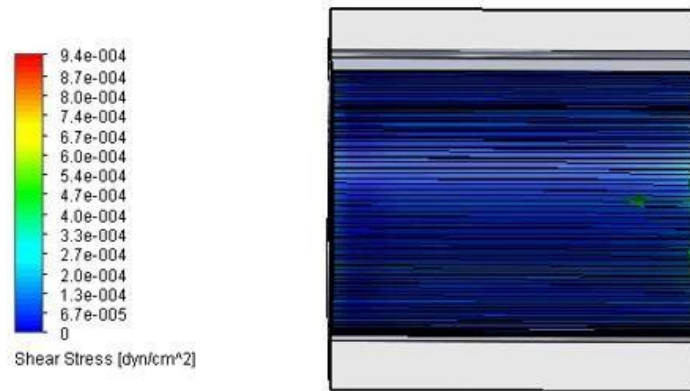


Figure 76: Group 3 with channels at 1 mL/minute flow rate.

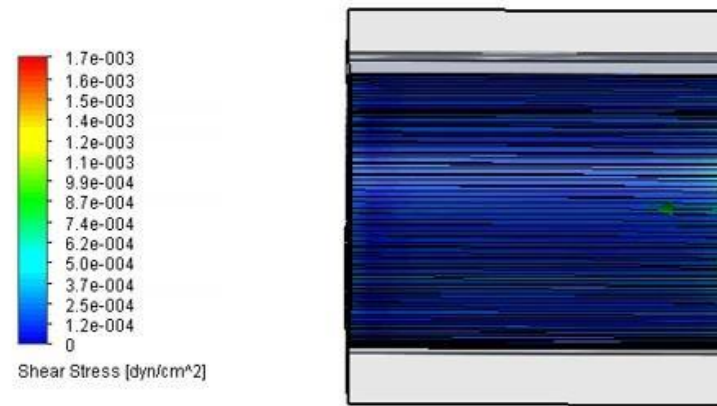


Figure 77: Group 3 with channels at 2 mL/minute flow rate.

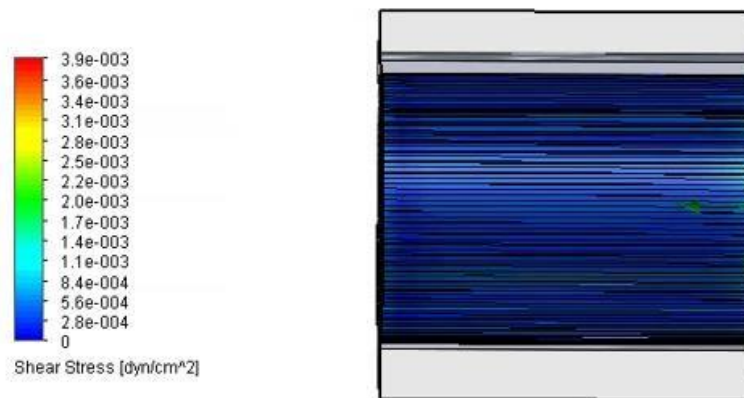


Figure 78: Group 3 with channels at 5 mL/minute flow rate.

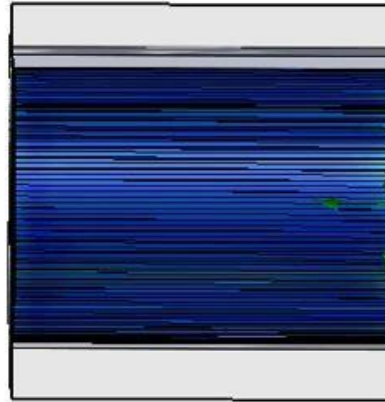
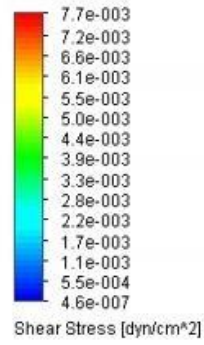


Figure 79: Group 3 with channels at 10 mL/minute flow rate.

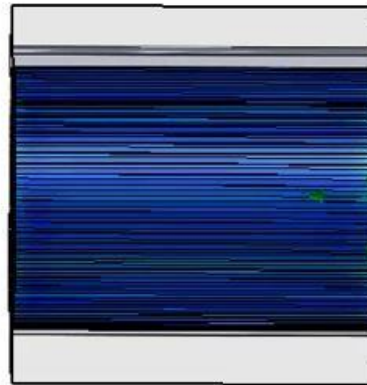
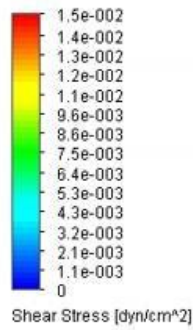


Figure 80: Group 3 with channels at 20 mL/minute flow rate.

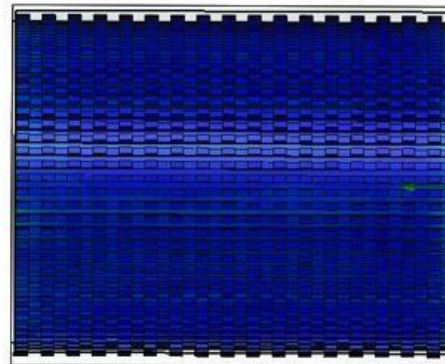
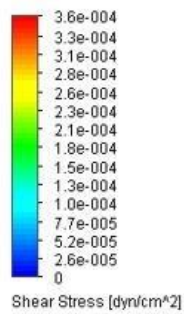


Figure 81: Group 3 with channels and pits at 0.5 mL/minute flow rate.

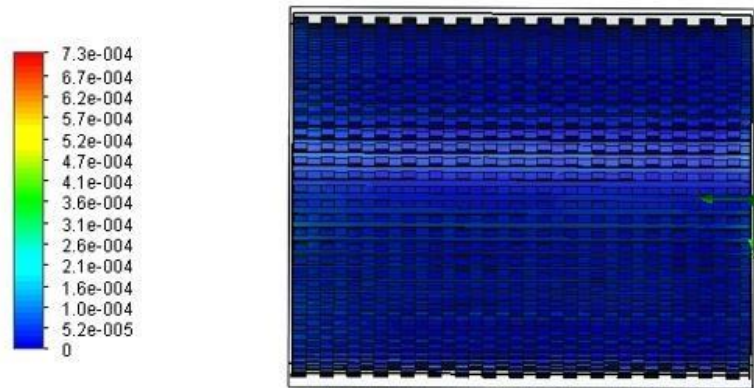


Figure 82: Group 3 with channels and pits at 1 mL/minute flow rate.

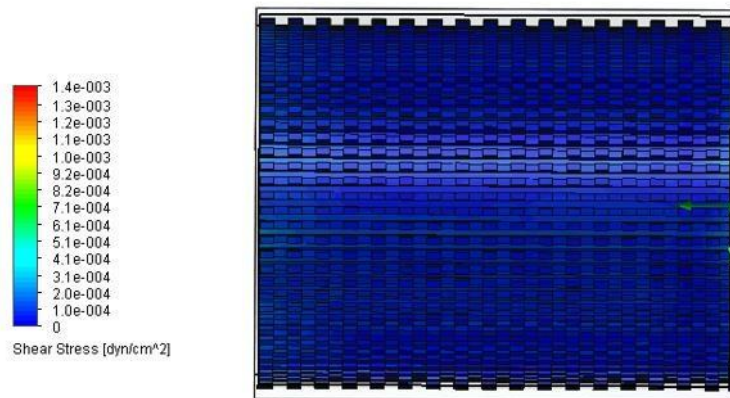


Figure 83: Group 3 with channels and pits at 2 mL/minute flow rate.

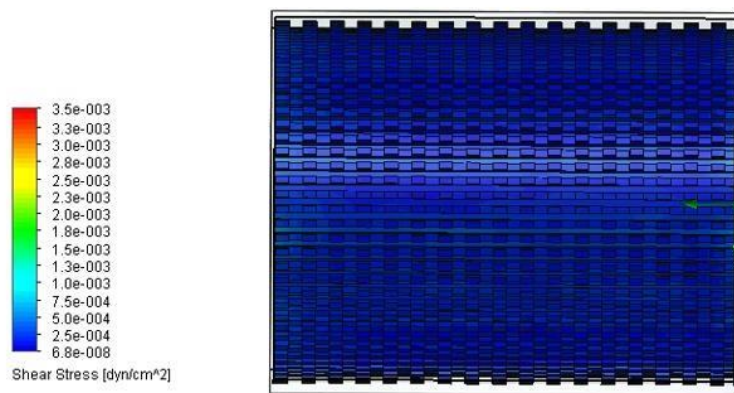


Figure 84: Group 3 with channels and pits at 5 mL/minute flow rate.

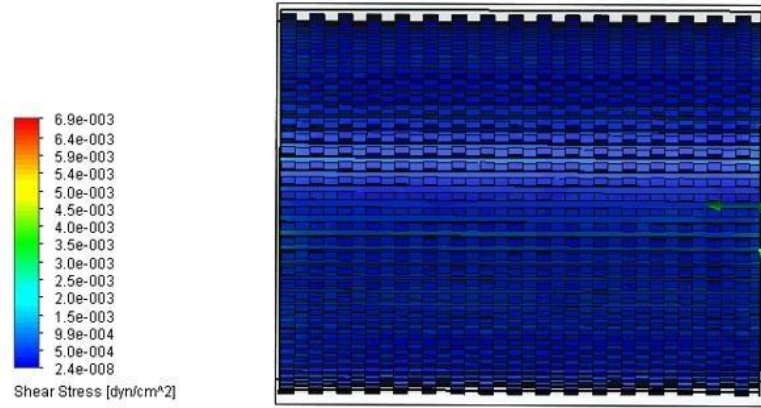


Figure 85: Group 3 with channels and pits at 10 mL/minute flow rate.

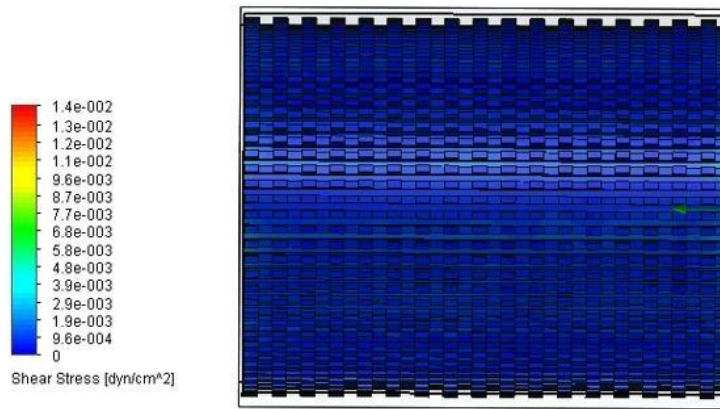


Figure 86: Group 3 with channels and pits at 20 mL/minute flow rate.

Flow Trajectories

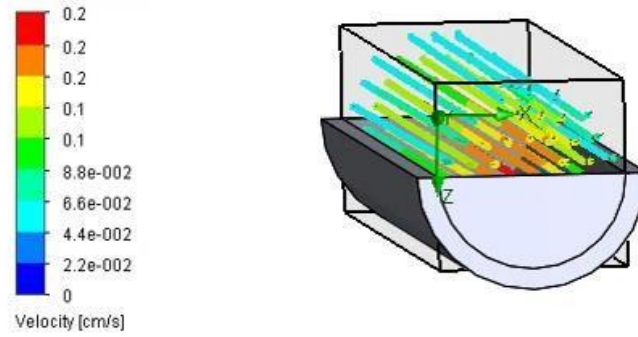


Figure 87: Group 1 no pattern at 0.5 mL/minute flow rate.

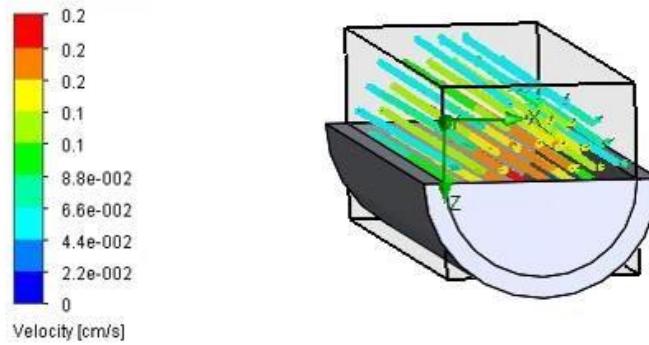


Figure 88: Group 1 no pattern at 1 mL/minute flow rate.

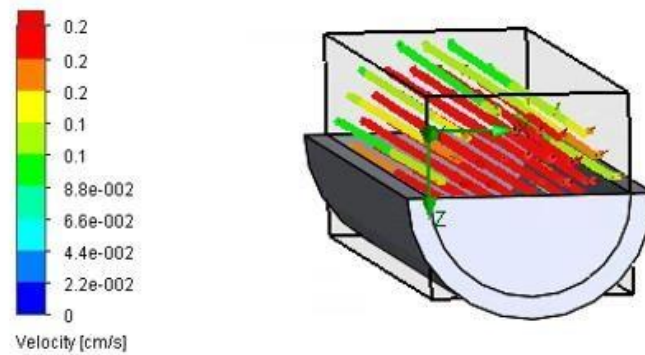


Figure 89: Group 1 no pattern at 2 mL/minute flow rate.

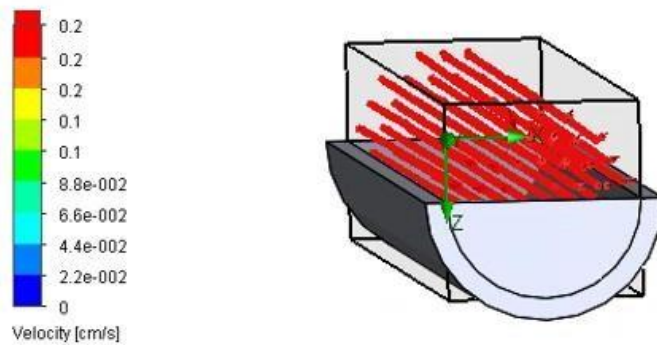


Figure 90: Group 1 no pattern at 5 mL/minute flow rate.

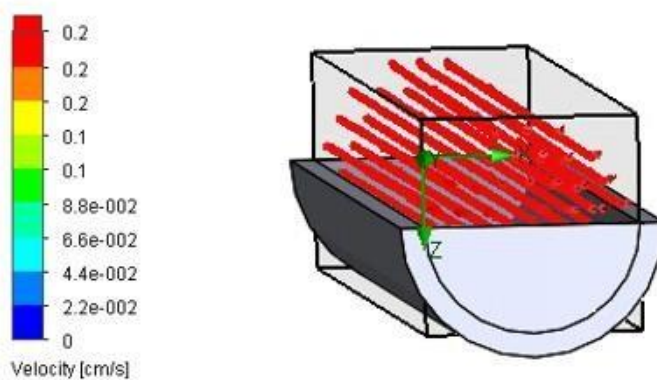


Figure 91: Group 1 no pattern at 10 mL/minute flow rate.

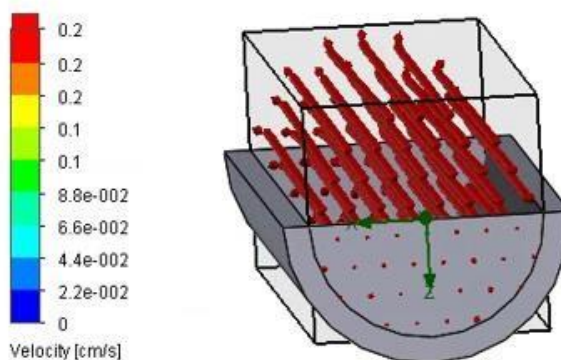


Figure 92: Group 1 no pattern at 20 mL/minute flow rate.

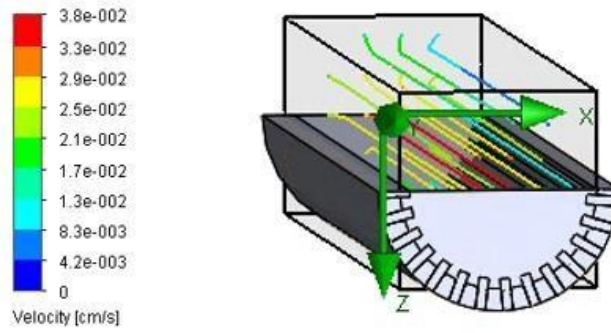


Figure 93: Group 1 with channels at 0.5 mL/minute flow rate.

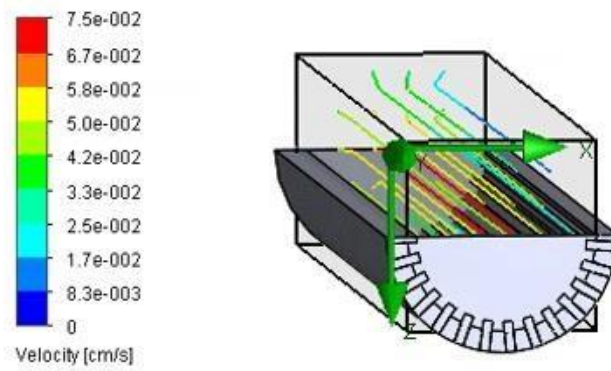


Figure 94: Group 1 with channels at 1 mL/minute flow rate.

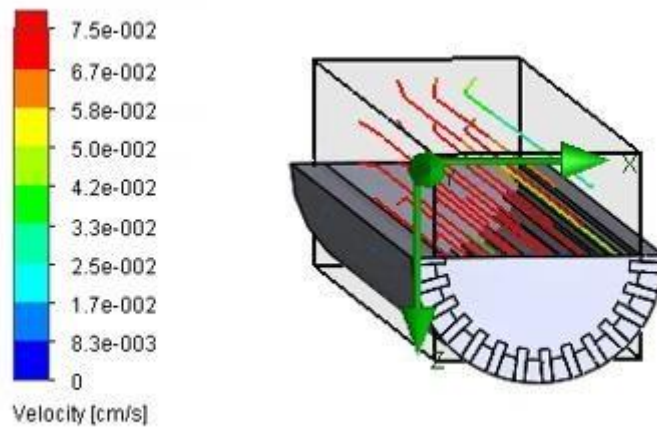


Figure 95: Group 1 with channels at 2 mL/minute flow rate.

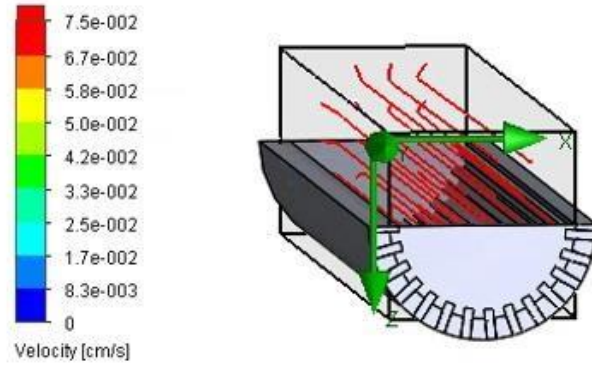


Figure 96: Group 1 with channels at 5 mL/minute flow rate.

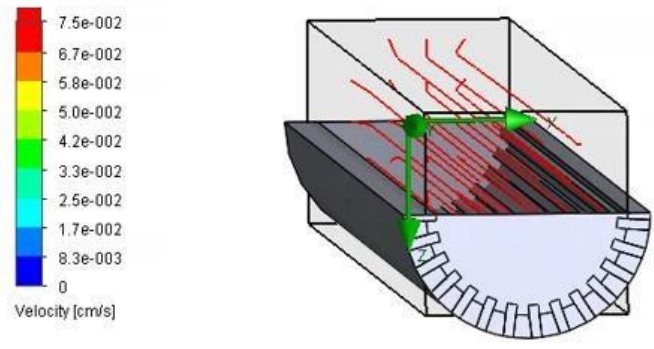


Figure 97: Group 1 with channels at 10 mL/minute flow rate.

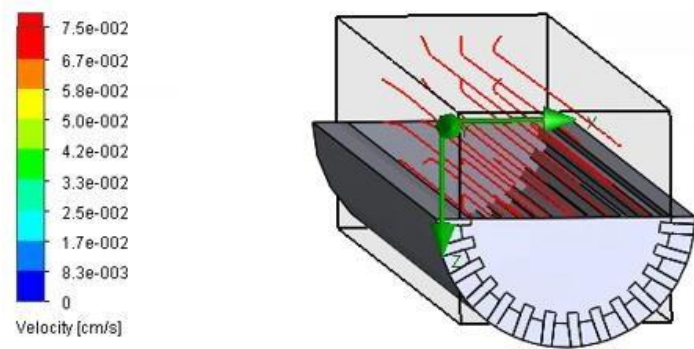


Figure 98: Group 1 with channels at 20 mL/minute flow rate.

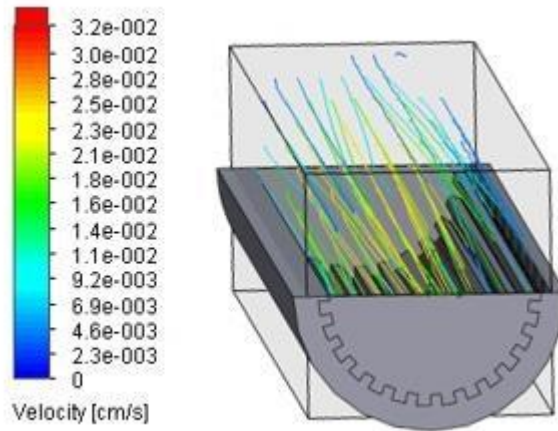


Figure 99: Group 1 with channels and pits at 0.5 mL/minute flow rate.

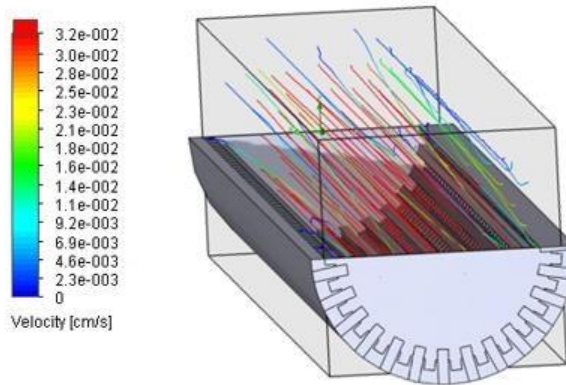


Figure 100: Group 1 with channels and pits at 1 mL/minute flow rate.

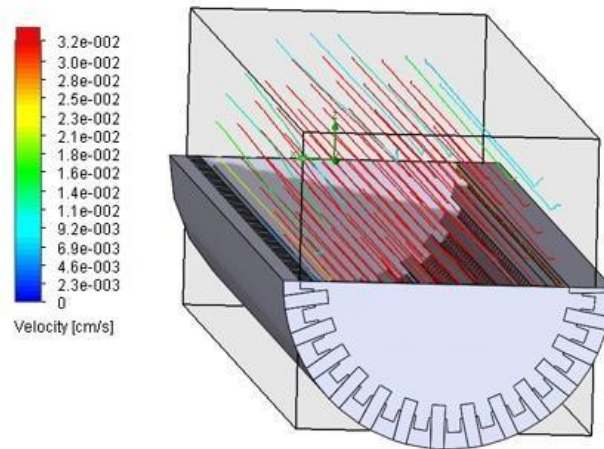


Figure 101: Group 1 with channels and pits at 2 mL/minute flow rate.

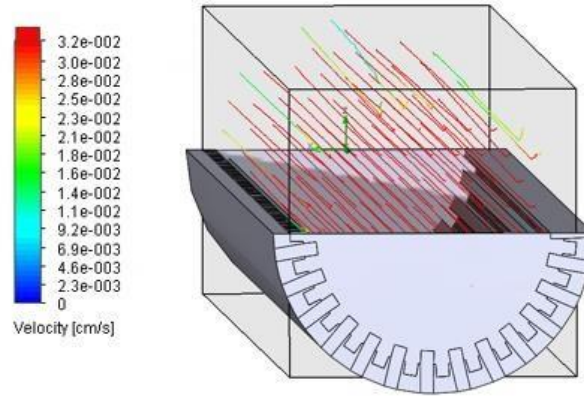


Figure 102: Group 1 with channels and pits at 5 mL/minute flow rate.

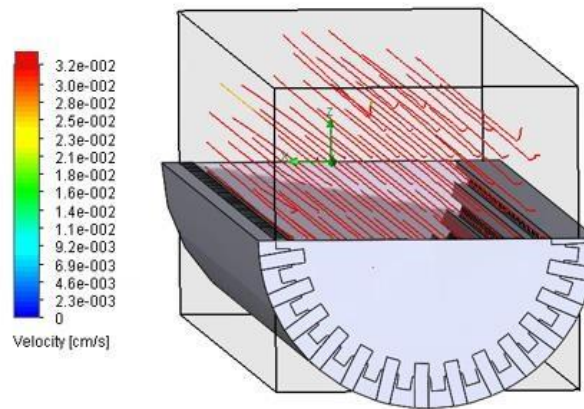


Figure 103: Group 1 with channels and pits at 10 mL/minute flow rate.

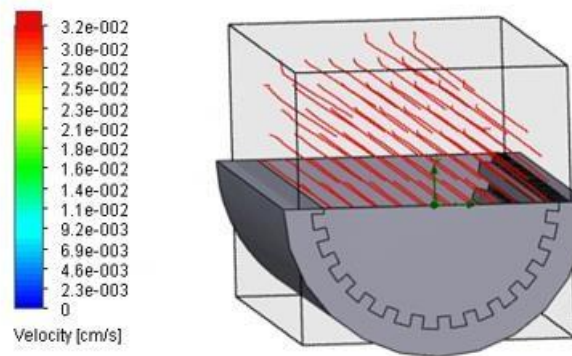


Figure 104: Group 1 with channels and pits at 20 mL/minute flow rate.

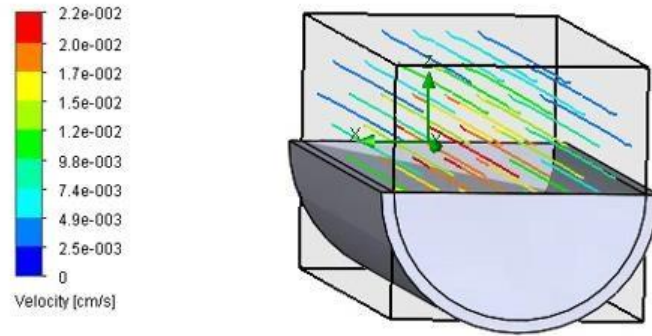


Figure 105: Group 2 no pattern at 0.5 mL/minute flow rate.

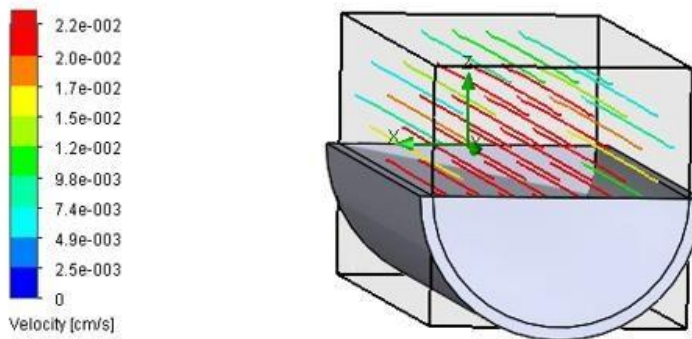


Figure 106: Group 2 no pattern at 1 mL/minute flow rate.

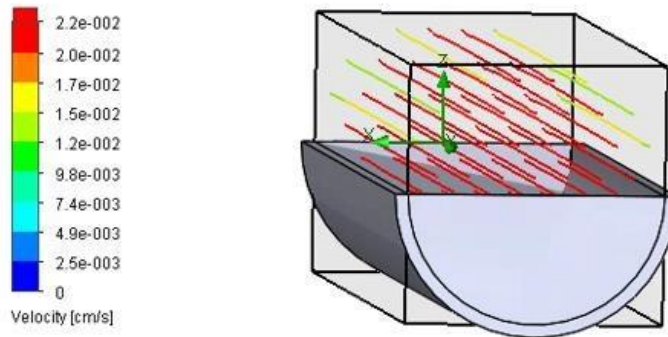


Figure 107: Group 2 no pattern at 2 mL/minute flow rate.

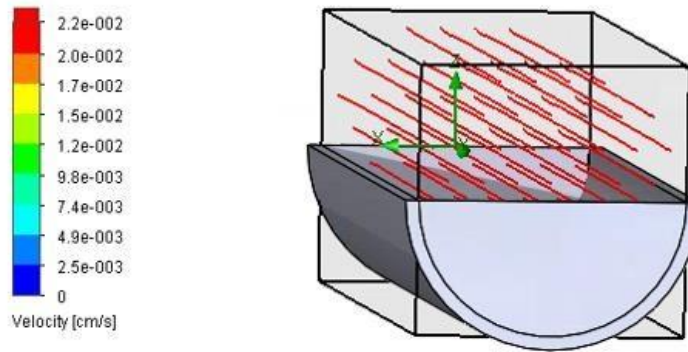


Figure 108: Group 2 no pattern at 5 mL/minute flow rate.

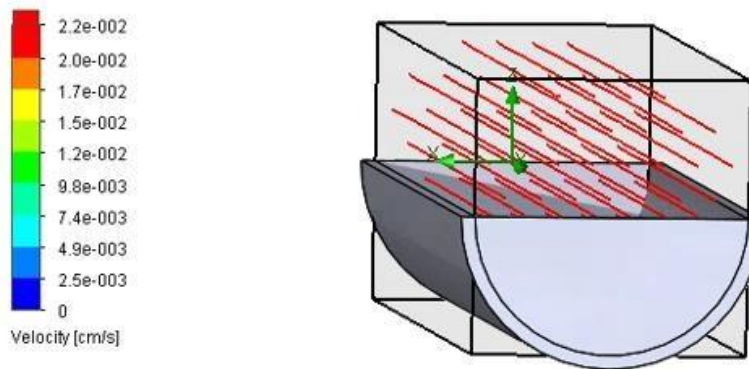


Figure 109: Group 2 no pattern at 10 mL/minute flow rate.

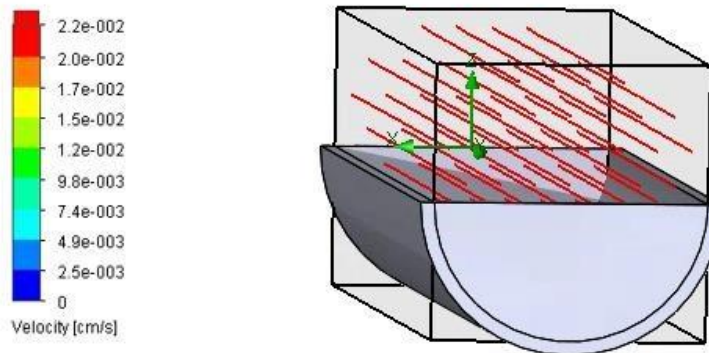


Figure 110: Group 2 no pattern at 20 mL/minute flow rate.

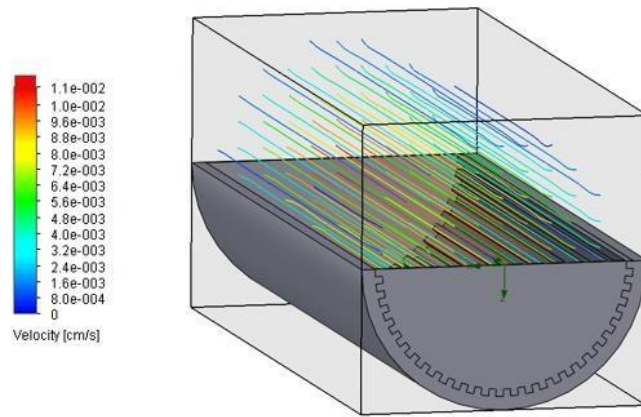


Figure 111: Group 2 with channels at 0.5 mL/minute flow rate.

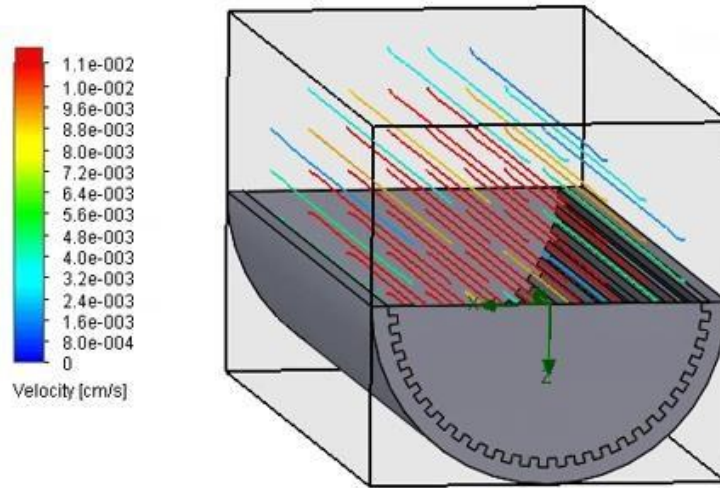


Figure 112: Group 2 with channels at 1 mL/minute flow rate.

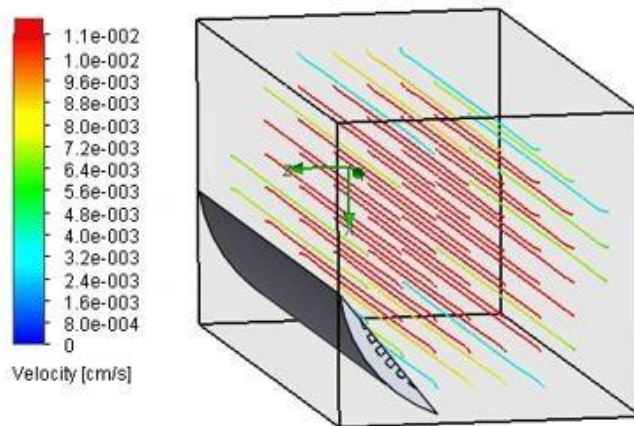


Figure 113: Group 2 with channels at 2 mL/minute flow rate.

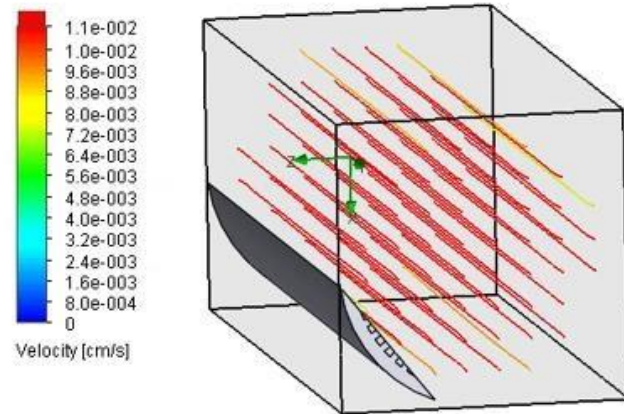


Figure 114: Group 2 with channels at 5 mL/minute flow rate.

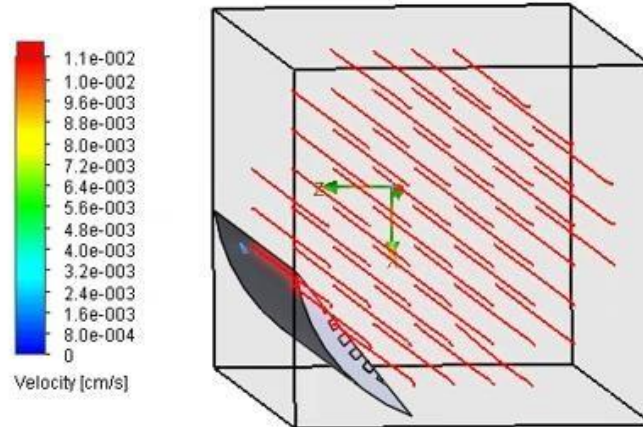


Figure 115: Group 2 with channels at 10 mL/minute flow rate.

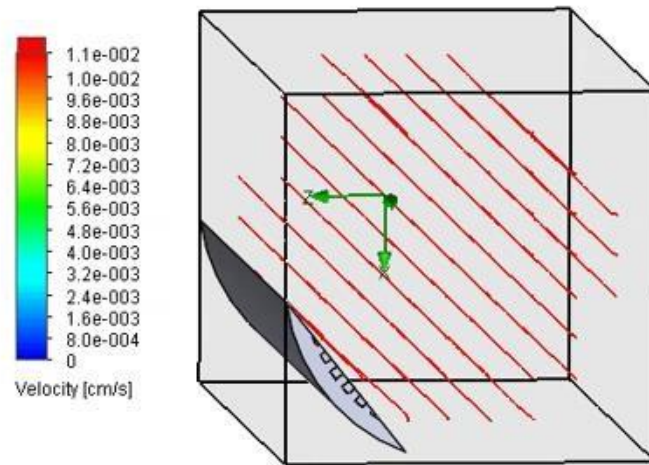


Figure 116: Group 2 with channels at 20 mL/minute flow rate.

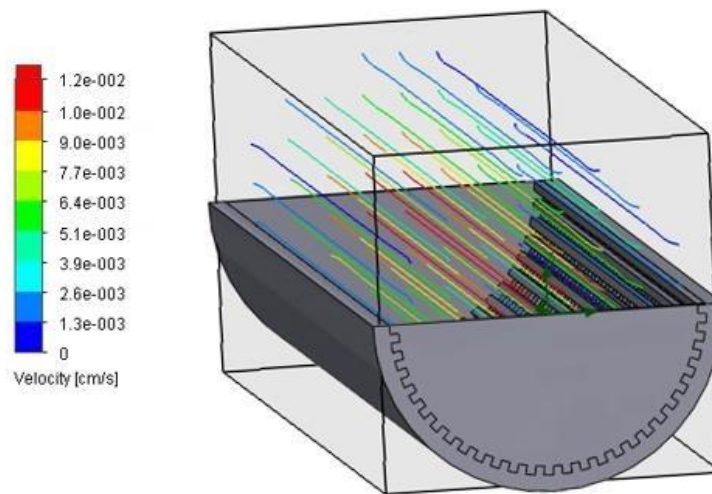


Figure 117: Group 2 with channels and pits at 0.5 mL/minute flow rate.

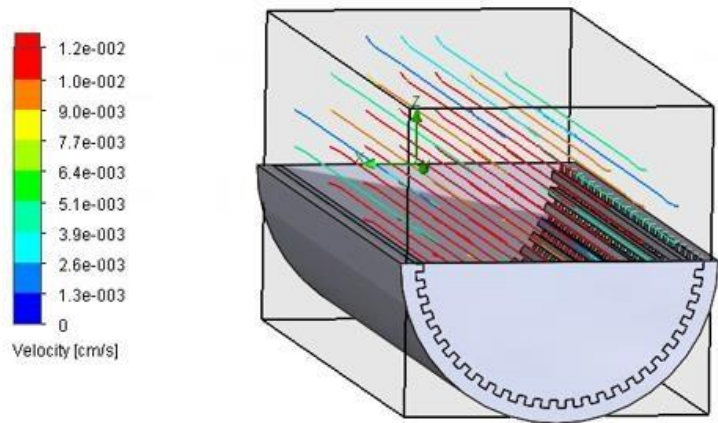


Figure 118: Group 2 with channels and pits at 1 mL/minute flow rate.

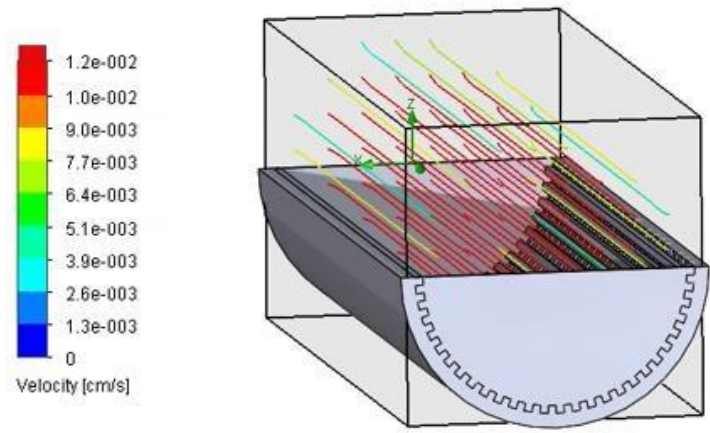


Figure 119: Group 2 with channels and pits at 2 mL/minute flow rate.

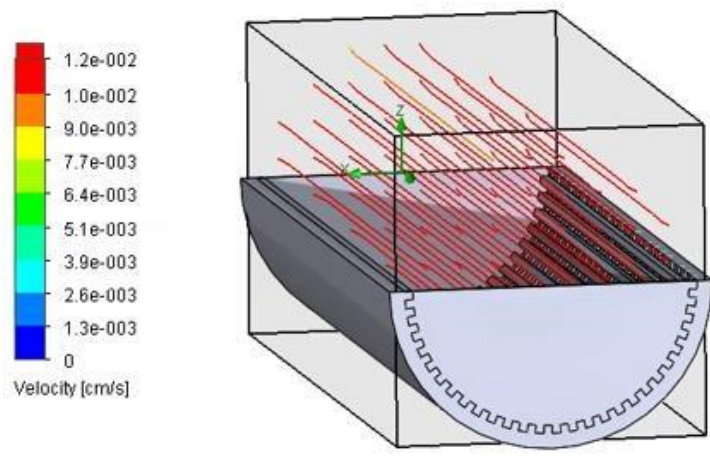


Figure 120: Group 2 with channels and pits at 5 mL/minute flow rate.

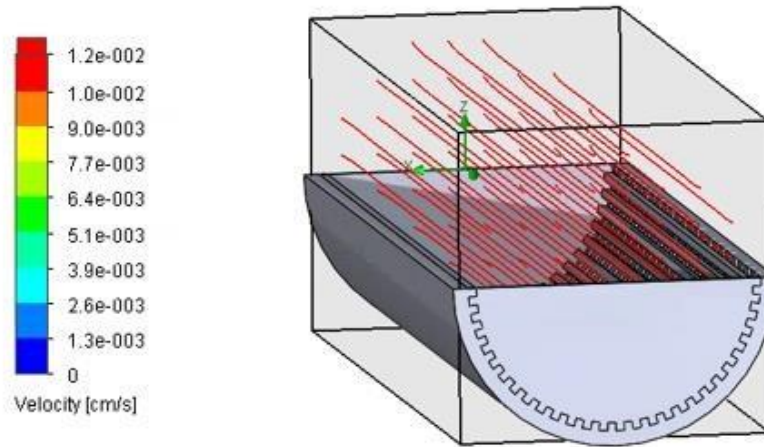


Figure 121: Group 2 with channels and pits at 10 mL/minute flow rate.

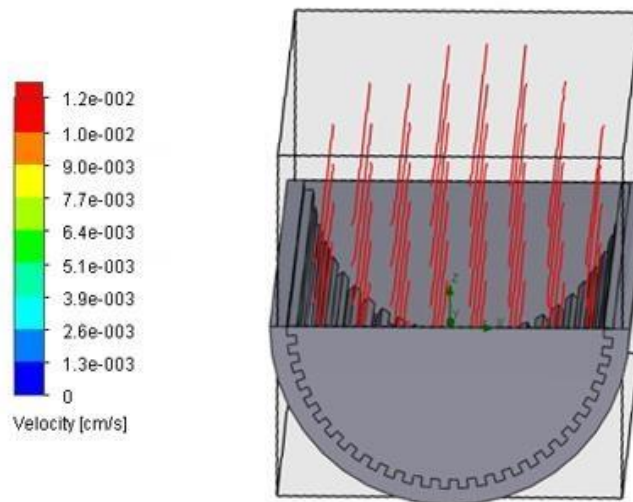


Figure 122: Group 2 with channels and pits at 20 mL/minute flow rate.

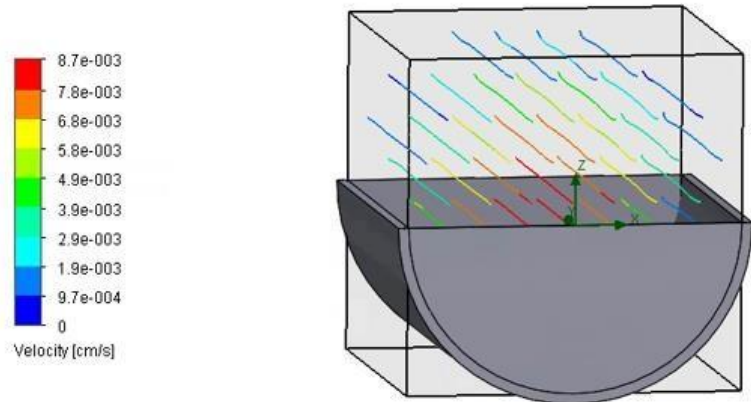


Figure 123: Group 3 no pattern at 0.5 mL/minute flow rate.

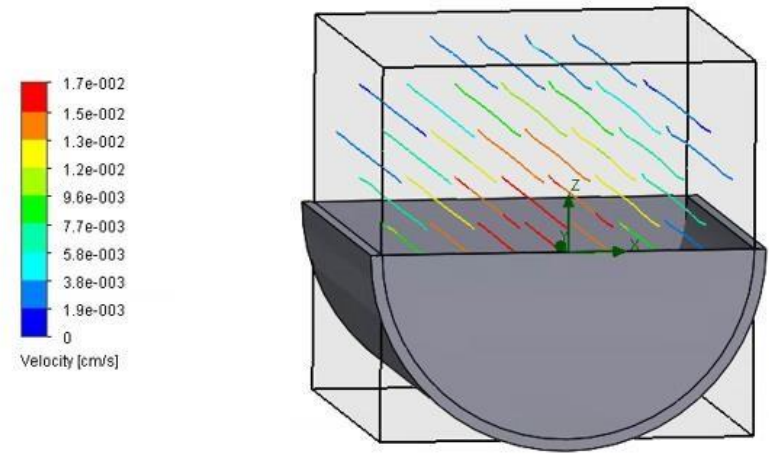


Figure 124: Group 3 no pattern at 1 mL/minute flow rate.

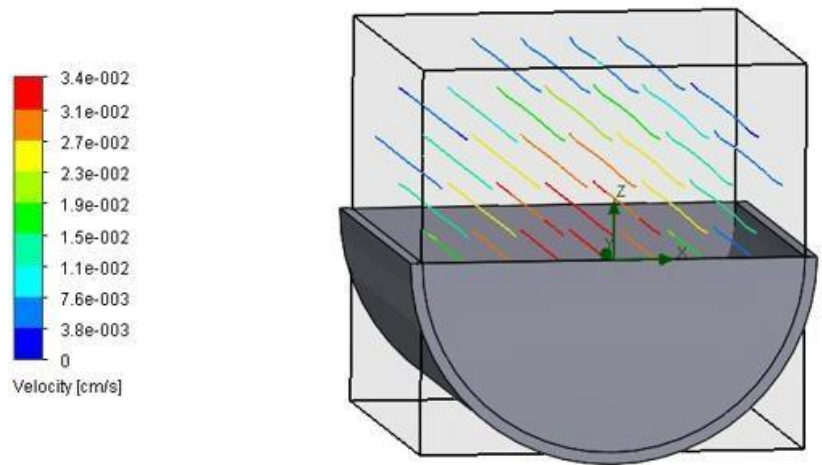


Figure 125: Group 3 no pattern at 2 mL/minute flow rate.

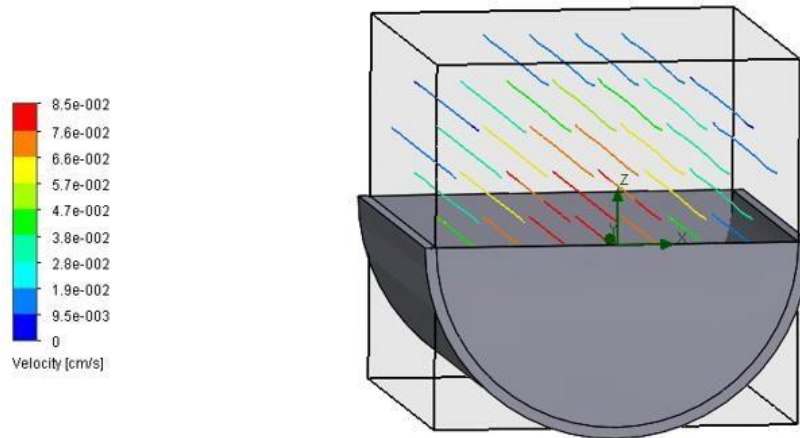


Figure 126: Group 3 no pattern at 5 mL/minute flow rate.

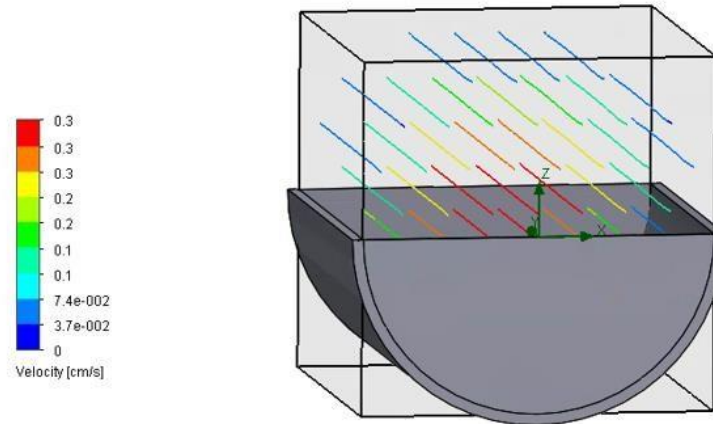


Figure 127: Group 3 no pattern at 10 mL/minute flow rate.

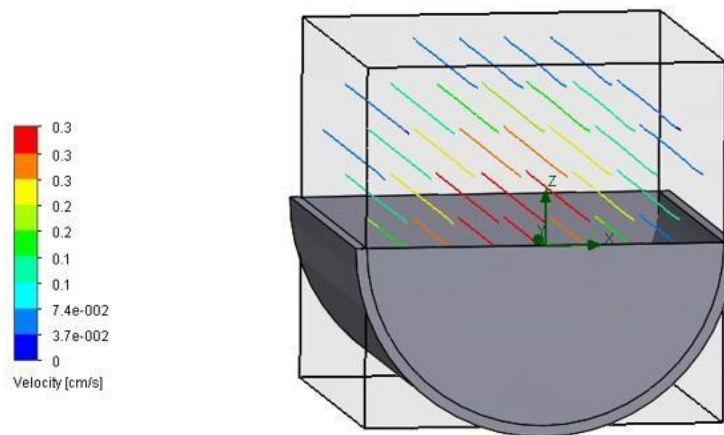


Figure 128: Group 3 no pattern at 20 mL/minute flow rate.

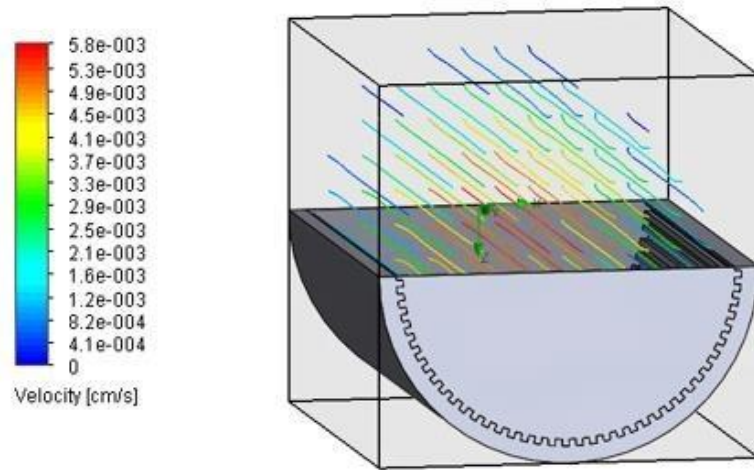


Figure 129: Group 3 with channels at 0.5 mL/minute flow rate.

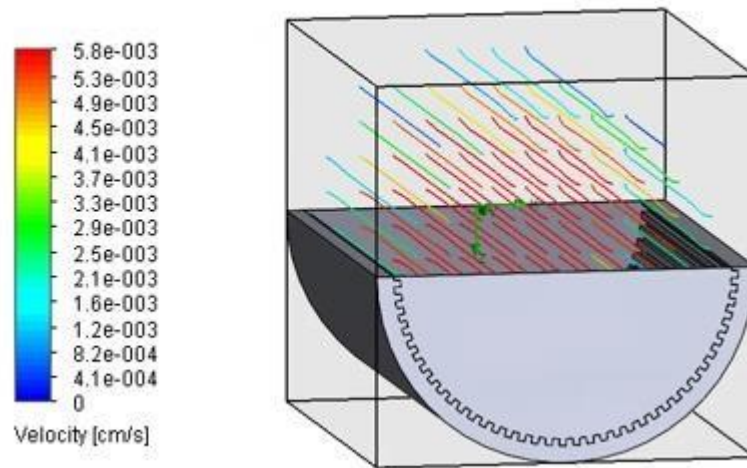


Figure 130: Group 3 with channels at 1 mL/minute flow rate.

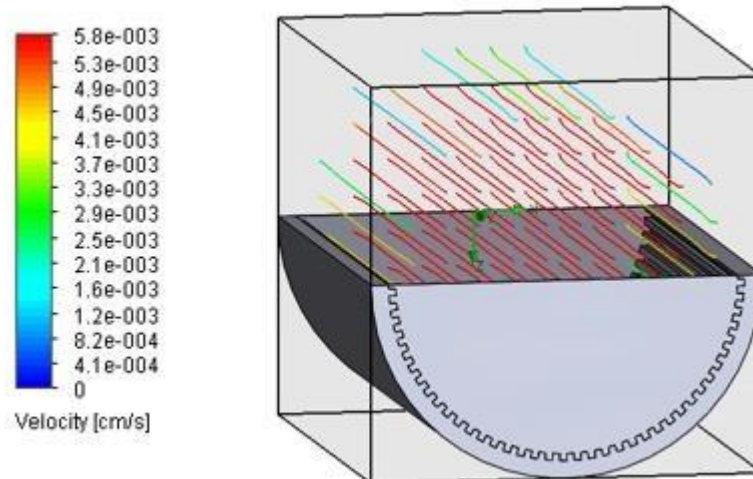


Figure 131: Group 3 with channels at 2 mL/minute flow rate.

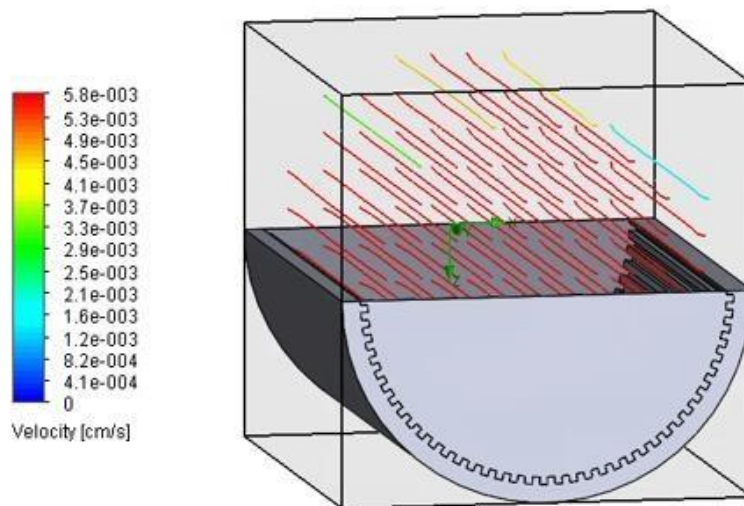


Figure 132: Group 3 with channels at 5 mL/minute flow rate.

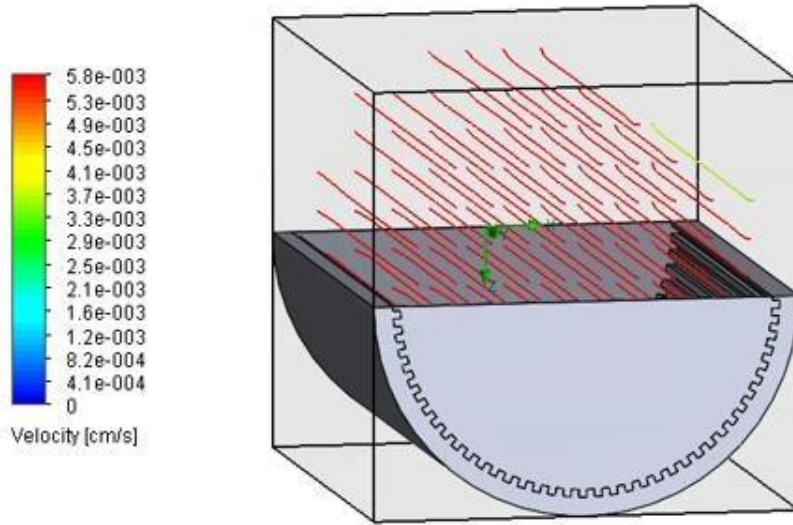


Figure 133: Group 3 with channels at 10 mL/minute flow rate.

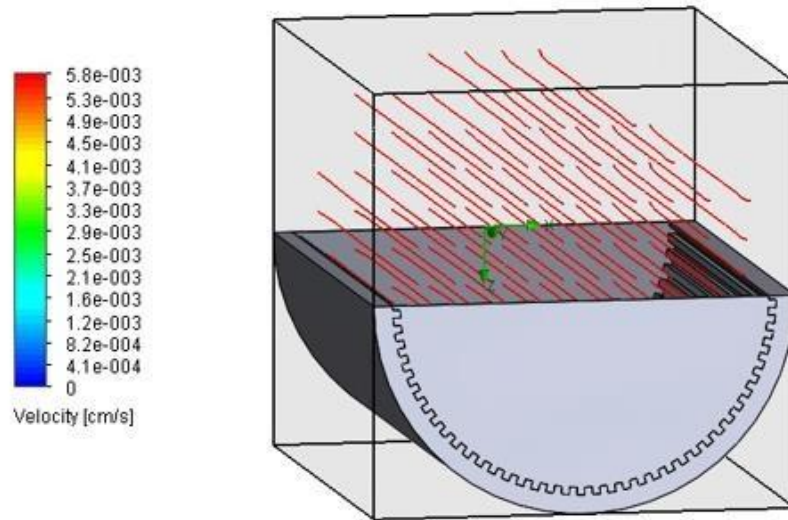


Figure 134: Group 3 with channels at 20 mL/minute flow rate.

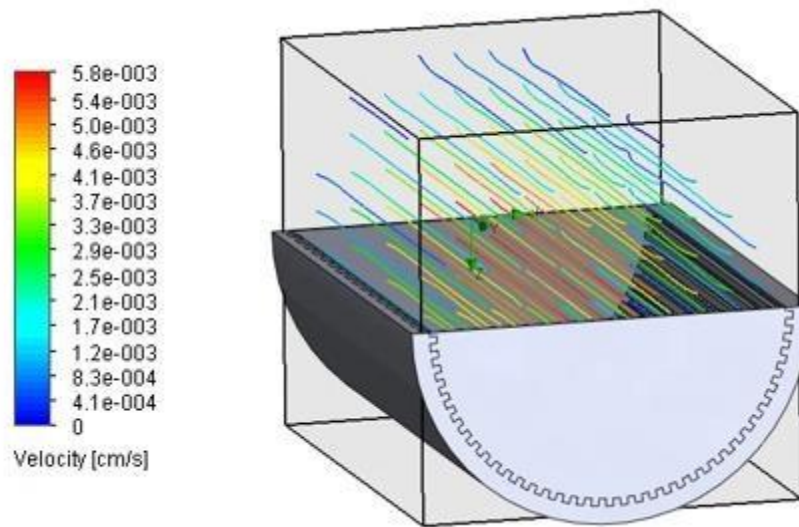


Figure 135: Group 3 with channels and pits at 0.5 mL/minute flow rate.

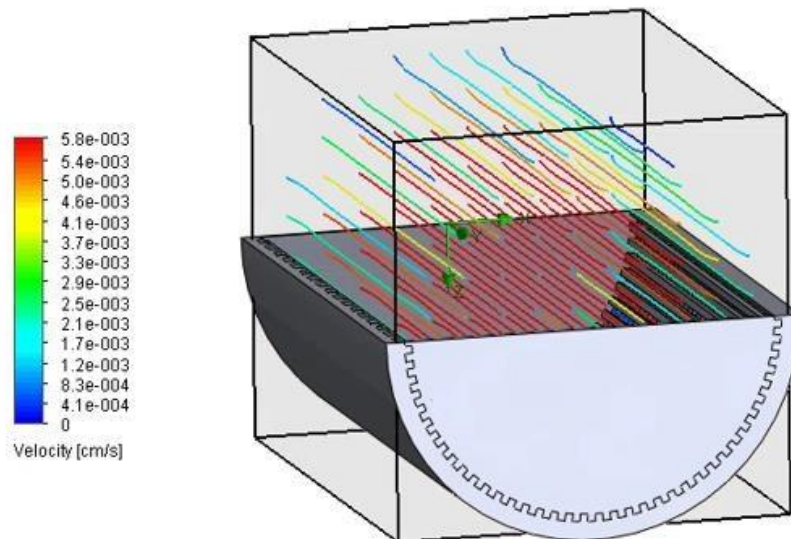


Figure 136: Group 3 with channels and pits at 1 mL/minute flow rate.

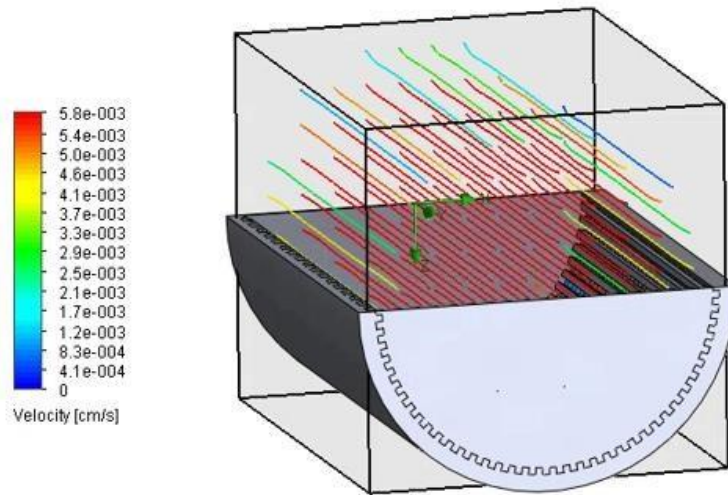


Figure 137: Group 3 with channels and pits at 2 mL/minute flow rate.

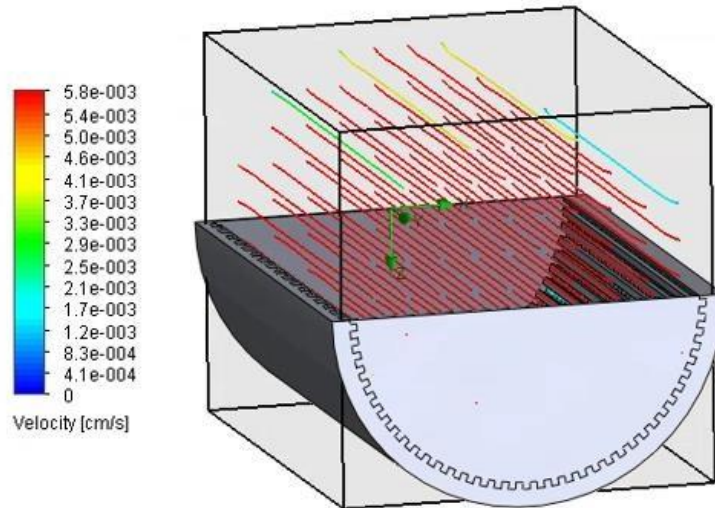


Figure 138: Group 3 with channels and pits at 5 mL/minute flow rate.

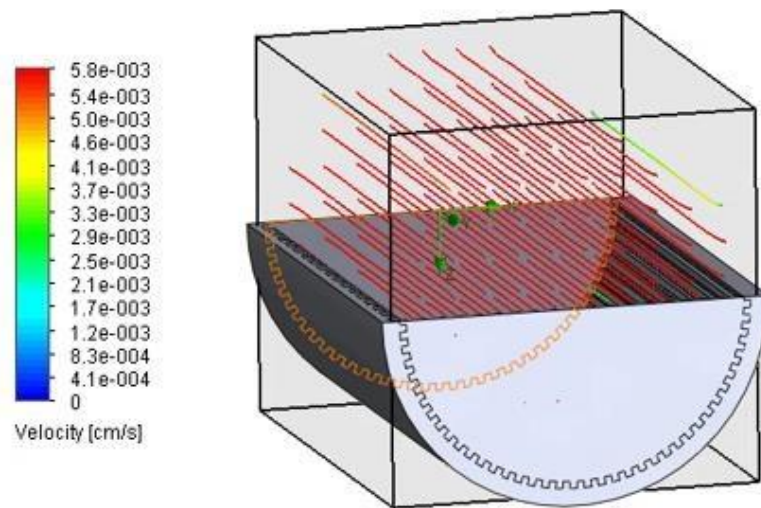


Figure 139: Group 3 with channels and pits at 10 mL/minute flow rate.

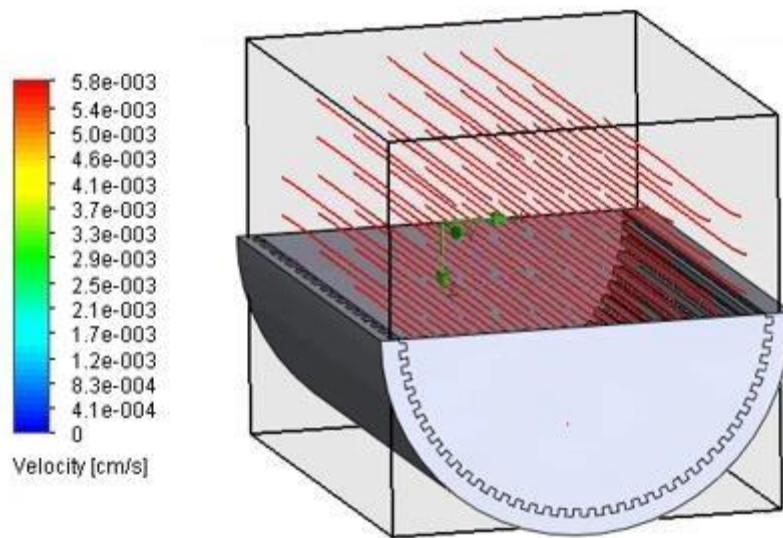


Figure 140: Group 3 with channels and pits at 20 mL/minute flow rate.

Bibliography

1. Liu, Y., Lim, J. & Teoh, S. H. Review: Development of clinically relevant scaffolds for vascularised bone tissue engineering. *Biotechnol. Adv.* **31**, 688– 705 (2013).
2. Sen, M. K. & Miclau, T. Autologous iliac crest bone graft: should it still be the gold standard for treating nonunions? . *Injury* **38 Suppl 1**, S75–80 (2007).
3. Matthews, D., Samdany, A. & Ahmed, S. U. An alternative management option for infected non-union of long bone fractures. *J. Clin. Orthop. Trauma* **4**, 43–45 (2013).
4. Nonfatal Hospitalized Injuries, Both Sexes, All Ages , United States, 2010. *CDC WISQARS 2014*, (2014).
5. Calori, G. M. *et al.* Incidence of donor site morbidity following harvesting from iliac crest or RIA graft. *Injury* **45**, S116–S120 (2014).
6. Laurencin, C. T., Ambrosio, A. M. A., Borden, M. D. & Cooper, J. A. Tissue Engineering: Orthopedic Applications. *Annu. Rev. Biomed. Eng.* **1**, 19–46 (1999).
7. Giannoudis, P. V, Dinopoulos, H. & Tsiridis, E. Bone substitutes: an update. *Injury* **36 Suppl 3**, S20–S27 (2005).
8. Yeatts, A. B. & Fisher, J. P. Bone tissue engineering bioreactors: Dynamic culture and the influence of shear stress. *Bone* **48**, 171–181 (2011).

9. Yeatts, A. B. & Fisher, J. P. Tubular Perfusion System for the Long-Term Dynamic Culture of Human Mesenchymal Stem Cells. *Tissue Eng. Part C Methods* **17**, 337–348 (2011).
10. Bertassoni, L. E. *et al.* Hydrogel bioprinted microchannel networks for vascularization of tissue engineering constructs. *Lab Chip* **14**, 2202–2211 (2014).
11. Bettahalli, N. M. S., Steg, H., Wessling, M. & Stamatialis, D. Development of poly(l-lactic acid) hollow fiber membranes for artificial vasculature in tissue engineering scaffolds. *J. Memb. Sci.* **371**, 117–126 (2011).
12. Kolesky, D. B. *et al.* 3D bioprinting of vascularized, heterogeneous cell-laden tissue constructs. *Adv. Mater.* **26**, 3124–30 (2014).
13. Rouwkema, J., Rivron, N. C. & van Blitterswijk, C. a. Vascularization in tissue engineering. *Trends Biotechnol.* **26**, 434–441 (2008).
14. Tocchio, A. *et al.* Versatile fabrication of vascularizable scaffolds for large tissue engineering in bioreactor. *Biomaterials* **45**, 124–31 (2015).
15. Liu, J., Zheng, H., Poh, P., Machens, H.-G. & Schilling, A. Hydrogels for Engineering of Perfusable Vascular Networks. *Int. J. Mol. Sci.* **16**, 15997– 16016 (2015).
16. Selvaganapathy, P. R., & Attalla, R. Microfluidic vascular channels in gells using commercial 3D printers. *Microfluidics, BioMEMS, and Medical Microsystems.* (2016).

17. Yeatts, A. B., Choquette, D. T. & Fisher, J. P. Bioreactors to influence stem cell fate: Augmentation of mesenchymal stem cell signaling pathways via dynamic culture systems. *Biochim. Biophys. Acta - Gen. Subj.* **1830**, 2470–2480 (2013).
18. Rotenberg, M. Y., Ruvinov, E., Armoza, A., & Cohen, S. A multi-shear perfusion bioreactor for investigating shear stress effects in endothelial cell constructs. *Lab on a Chip*, *12*, 2696. (2012).
19. Yeatts, A. B., Geibel, E. M., Fears, F. F. & Fisher, J. P. Human mesenchymal stem cell position within scaffolds influences cell fate during dynamic culture. *Biotechnol. Bioeng.* **109**, 2381–2391 (2012).
20. Gui, L. & Niklason, L. E. Vascular tissue engineering: Building perfusable vasculature for implantation. *Curr. Opin. Chem. Eng.* **3**, 68–74 (2014).
21. Zhao, L., Lee, V. K., Yoo, S.-S., Dai, G. & Intes, X. The integration of 3-D cell printing and mesoscopic fluorescence molecular tomography of vascular constructs within thick hydrogel scaffolds. *Biomaterials* **33**, 5325–5332 (2012).
22. Mironov, V., Boland, T., Trusk, T., Forgacs, G. & Markwald, R. R. Organ printing: computer-aided jet-based 3D tissue engineering. *Trends Biotechnol.* **21**, 157–161 (2003).
23. Skardal, A., Zhang, J. & Prestwich, G. D. Bioprinting vessel-like constructs using hyaluronan hydrogels crosslinked with tetrahedral polyethylene glycol tetracrylates. *Biomaterials* **31**, 6173–6181 (2010)

24. Cooke, M. N., Fisher, J. P., Dean, D., Rimnac, C. & Mikos, A. G. Use of stereolithography to manufacture critical-sized 3D biodegradable scaffolds for bone ingrowth. *J. Biomed. Mater. Res. B. Appl. Biomater.* **64**, 65–69 (2003).
25. Bellan, L. M., Strychalski, E. A. & Craighead, H. G. Nanochannels fabricated in polydimethylsiloxane using sacrificial electrospun polyethylene oxide nanofibers. *J. Vac. Sci. Technol. B Microelectron. Nanom. Struct.* **26**, 1728 (2008).
26. Gualandi, C., Zucchelli, A., Fernández Osorio, M., Belcari, J. & Focarete, M. L. Nanovascularization of polymer matrix: generation of nanochannels and nanotubes by sacrificial electrospun fibers. *Nano Lett.* **13**, 5385–90 (2013).
27. Sandgren, T., Sonesson, B., Ahlgren, Å. R. & Länne, T. The diameter of the common femoral artery in healthy human: Influence of sex, age, and body size. *J. Vasc. Surg.* **29**, 503–510 (1999).
28. Mohyeldin, A., Garzón-Muvdi, T. & Quiñones-Hinojosa, A. Oxygen in Stem Cell Biology: A Critical Component of the Stem Cell Niche. *Cell Stem Cell* **7**, 150–161 (2010).
29. Utting, J. C. *et al.* Hypoxia inhibits the growth, differentiation and boneforming capacity of rat osteoblasts. *Exp. Cell Res.* **312**, 1693–1702 (2006).
30. Lennon, D. P., Edmison, J. M. & Caplan, a I. Cultivation of rat marrowderived mesenchymal stem cells in reduced oxygen tension: effects on in vitro and in vivo osteochondrogenesis. *J. Cell. Physiol.* **187**, 345–355 (2001).

31. Harrison, J. S., Rameshwar, P., Chang, V. & Bandari, P. Oxygen Saturation in the Bone Marrow of Healthy Volunteers. *Blood* **99**, 394 (2002).
32. Volkmer, E. *et al.* Hypoxia in static and dynamic 3D culture systems for tissue engineering of bone. *Tissue Eng. Part A* **14**, 1331–1340 (2008).
33. Potier, E. *et al.* Hypoxia affects mesenchymal stromal cell osteogenic differentiation and angiogenic factor expression. *Bone* **40**, 1078–1087 (2007).
34. Bettinger, C. J., Langer, R., & Borenstein, J.
Engineering substrate topography at the micro- and nanoscale to control cell function. *Angew Chem Int Ed Engl.* 5406. (2009).
35. Kim, J., Kim, H. N., Lim, K., Kim, Y., Pandey, S., Garg, P., et al. Synergistic effects of nanotopography and co-culture with endothelial cells on osteogenesis of mesenchymal stem cells. *Biomaterials*, *34*, 7257. (2013).
36. Bettinger, C. J., Zhang, Z., Gerecht, S., Borenstein, J., & Langer, R.
Enhancement of in vitro capillary tube formation by substrate nanotopography. *Adv Mater.* 99. (2008).
37. Kim, H. N., Jiao, A., Hwang, N., Kim, M. S., & Kang, D. H. Nanotopography-guided tissue engineering and regenerative medicine. *Advanced Drug Delivery Reviews*, *65*, 536. (2013).
38. Sladkova, M. & de Peppo, G. Bioreactor Systems for Human Bone Tissue Engineering. *Processes* **2**, 494–525 (2014).
39. Li, Y. S., Haga, J. H., & Chien, S. (2005). Molecular basis of the effects of shear stress on vascular endothelial cells. *Journal of Biomechanics*. 1949.